Structures Research
Report 2016/113605-
113606

University of Florida
Civil and Coastal Engineering

University of Florida
Civil and Coastal Engineering

UF

GATOR Engineering

University of Florida
Civil and Coastal Engineering

Final Report September 2016

Pendulum Impact Testing of Metallic, Non-metallic, and Hybrid Sign Posts

Principal investigators:
Gary R. Consolazio, Ph.D.
H. R. (Trey) Hamilton, III, Ph.D., P.E.

Graduate research assistants:
Matías Groetaers
Douglas Innocent

Department of Civil and Coastal Engineering
University of Florida
P.O. Box 116580
Gainesville, Florida 32611

Sponsor:
Florida Department of Transportation (FDOT)

Contract:
UF Project Nos. 113605, 113606, 92335 & 92728
FDOT Contract No. BDV31-977-16 & BDK75-977-42

DISCLAIMER

The opinions, findings, and conclusions expressed in this publication are those of the authors and not necessarily those of the State of Florida Department of Transportation.

SI (MODERN METRIC) CONVERSION FACTORS

*APPROXIMATE CONVERSIONS **TO** SI UNITS*

SYMBOL	WHEN YOU KNOW	MULTIPLY BY	TO FIND	SYMBOL
LENGTH				
in	inches	25.4	millimeters	mm
ft	feet	0.305	meters	m
yd	yards	0.914	meters	m
mi	miles	1.61	kilometers	km
AREA				
in^2	square inches	645.2	square millimeters	mm^2
ft^2	square feet	0.093	square meters	m^2
yd^2	square yard	0.836	square meters	m^2
ac	acres	0.405	hectares	ha
mi^2	square miles	2.59	square kilometers	km^2
VOLUME				
fl oz	fluid ounces	29.57	milliliters	mL
gal	gallons	3.785	liters	L
ft^3	cubic feet	0.028	cubic meters	m^3
yd^3	cubic yards	0.765	cubic meters	m^3
NOTE: volumes greater than 1000 L shall be shown in m^3				
MASS				
oz	ounces	28.35	grams	g
lb	pounds	0.454	kilograms	kg
T	short tons (2,000 lb)	0.907	Megagrams	Mg (or "t")
TEMPERATURE (exact degrees)				
^oF	Fahrenheit	5(F-32)/9 or (F-32)/1.8	Celsius	^oC
FORCE and PRESSURE or STRESS				
kip	1,000 pound force	4.45	kilonewtons	kN
lbf	pound force	4.45	newtons	N
lbf/in^2	pound force per square inch	6.89	kilopascals	kPa
ksi	kips force per square inch	6.89	Megapascals	MPa

TECHNICAL REPORT DOCUMENTATION PAGE

1. Report No.	2. Government Accession No.	3. Recipient's Catalog No.

4. Title and Subtitle	5. Report Date
Pendulum Impact Testing of Metallic, Non-metallic, and Hybrid Sign Posts, Phase II	September 2016
	6. Performing Organization Code
	8. Performing Organization Report No.
7. Author(s)	
Gary Consolazio, H.R. Hamilton, Matías Groetaers, Douglas Innocent	2016/113605-113606
9. Performing Organization Name and Address	10. Work Unit No. (TRAIS)
University of Florida Department of Civil and Coastal Engineering 365 Weil Hall, P.O. Box 116580 Gainesville, FL 32611-6580	11. Contract or Grant No. BDV31-977-16 & BDK75-977-42
12. Sponsoring Agency Name and Address	13. Type of Report and Period Covered
Florida Department of Transportation Research Management Center 605 Suwannee Street, MS 30 Tallahassee, FL 32399-0450	Final Report
	14. Sponsoring Agency Code

15. Supplementary Notes

16. Abstract

Current FDOT design standards for large roadside sign structures employ steel posts and steel connection components that are intended to survive hurricane wind loading, but break away under direct vehicular impact loading—the latter behavior to limit risk to vehicle occupants who could be injured by abrupt vehicle deceleration. Alternative structural materials, such as fiber-reinforced polymer (FRP), have the potential to offer advantages over steel when used in breakaway roadside sign structures. Because FRP is significantly lighter than steel, use of breakaway FRP sign posts could reduce occupant impact risk measures, such as occupant impact velocity (OIV), thereby improving roadside safety.

In this study, hybrid breakaway structural systems that combined FRP posts with steel connection components were conceptually developed, structurally designed, fabricated, and subjected to impact testing and static flexural testing. Two fundamentally different design approaches were investigated. In the first, steel cutting components were used to form a 'shear collar' that sliced through the FRP post during direct vehicular impact loading. In the second, the FRP post was joined to a steel 'moment-resisting, shear-frangible' breakaway connection. Impact testing of both systems was carried out using the FDOT pendulum impact test facility. To facilitate impact testing in a manner that was compliant with the requirements of AASHTO MASH, a new 1100C surrogate test vehicle—which mimics the behavior of an 1,100-kg production passenger car—was designed, fabricated, and experimentally tested/validated as part of this study. Results from pendulum impact testing and static flexural testing of hybrid FRP/steel sign structure systems revealed several, as-yet unsolved obstacles to successful integration of FRP and steel.

17. Key Words	18. Distribution Statement
	No restrictions.

19. Security Classif. (of this report)	20. Security Classif. (of this page)	21. No. of Pages	22. Price
Unclassified	Unclassified	124	

Form DOT F 1700.7 (8-72). Reproduction of completed page authorized

ACKNOWLEDGEMENTS

The authors thank the Florida Department of Transportation (FDOT) for providing the funding that made this research possible. Additionally, the authors acknowledge contributions made by FDOT Structures Research Center personnel who contributed significantly to this project by providing technical insights, suggestions, and assistance with fabrication and pendulum impact testing.

EXECUTIVE SUMMARY

Current FDOT design standards for large roadside sign structures employ steel posts and steel connection components that are intended to survive hurricane wind loading, but break away under direct vehicular impact loading—the latter behavior to limit risk to vehicle occupants who could be injured by abrupt vehicle deceleration. Alternative structural materials, such as fiber-reinforced polymer (FRP), have the potential to offer advantages over steel when used in breakaway roadside sign structures. Because FRP is significantly lighter than steel, use of breakaway FRP sign posts could reduce occupant impact risk measures, such as occupant impact velocity (OIV), thereby improving roadside safety.

In this study, hybrid breakaway structural systems that combined FRP posts with steel connection components were conceptually developed, structurally designed, fabricated, and subjected to impact testing and static flexural testing. Two fundamentally different design approaches were investigated. In the first, steel cutting components were used to form a 'shear collar' that sliced through the FRP post during direct vehicular impact loading. In the second, the FRP post was joined to a steel 'moment-resisting, shear-frangible' breakaway connection. Impact testing of both systems was carried out using the FDOT pendulum impact test facility. To facilitate impact testing in a manner that was compliant with the requirements of AASHTO MASH, a new 1100C surrogate test vehicle—which mimics the behavior of an 1,100-kg production passenger car—was designed, fabricated, and experimentally tested/validated as part of this study. Results from pendulum impact testing and static flexural testing of hybrid FRP/steel sign structure systems revealed several, as-yet unsolved obstacles to successful integration of FRP and steel.

TABLE OF CONTENTS

LIST OF FIGURES

Figure Page

LIST OF TABLES

Table Page

CHAPTER 1
INTRODUCTION

1.1 Background

Multi-post ground signs installed adjacent to roadways in Florida must be designed for hurricane wind loading as well as vehicle impact loading. With respect to hurricane wind loads, all structural components in a sign structure—support posts, base connections, etc.—must be designed to resist (i.e., survive without failing) the applicable code-specified wind loads. For design purposes, wind loading is treated as an equivalent-static pressure applied to the sign panel (Figure 1.1a). Due to the significant vertical offset that typically exists between the center of wind pressure, and the base of the support posts, wind loads generally produce large flexural moments that must be resisted both by the sign posts as well as by the base connections.

In contrast, under vehicle impact conditions, where an errant passenger vehicle leaves the roadway and strikes a roadside sign structure, the intended design goal is not structural survivability, but rather vehicle occupant survivability—or more specifically, prevention of serious occupant injury. Contact between the front bumper of a vehicle and a sign post typically occurs at a relatively low vertical elevation (~18 in. from the ground plane), thus application of vehicle impact loading (Figure 1.1b) causes large shear forces in the support posts and base connection components, but not significant flexural moments.

To limit the risk of injury to vehicle occupants, loads associated with vehicle collision can be employed to break (i.e., disengage) selected structural components in the base connections of a sign structure (Figure 1.2). Once the base connection components break away, flexural moment is transmitted along the height of the support post, in turn causing tension loading of a perforated steel 'fuse plate' located just below the sign panel. At a sufficiently high tension level, the fuse plate ruptures allowing the lower segment of the post to rotate out of the path of the vehicle. A hinge plate on the non-impact (downstream) side of the posts keeps the lower segment connected to the rest of the sign structure during rotation. (In Figure 1.3, an illustration of this overall process is shown, with rendering of the vehicle omitted).

Risk of injury to vehicle occupants during a collision is primarily associated with either vehicle decelerations or with parts of the sign structure deforming the vehicle compartment (e.g., causing roof intrusion). Regarding the former, abrupt vehicle deceleration can cause occupants to strike interior portions of the vehicle compartment at a velocity referred to as the 'occupant impact velocity' (OIV). Reducing the potential for occupant injury is achieved by limiting the OIV. In turn, limiting the OIV is achieved—from a structural design perspective—by designing a sign post system that breaks away during impact, thus reducing inertial post resistance and, accordingly, reducing vehicular deceleration. With respect to vehicle compartment intrusion, limiting the associated risk is achieved by ensuring that the lower segment of the post swings out of the path of the vehicle during collision.

Both of these risks (OIV and compartment intrusion) can be mitigated by reducing the weight (i.e., mass) of the components that make up a breakaway sign post. Reducing sign post and base connection mass: (1) reduces the inertial resistance, which in turn reduces vehicle deceleration and OIV and (2) increases the acceleration of the post away from the path of the impacting vehicle. Designing roadside sign structures using materials such as fiber-reinforced polymer (FRP) composites, which are less dense (i.e., less massive) than structural steel, therefore offers at least the potential for reducing occupant risks during errant vehicle impacts.

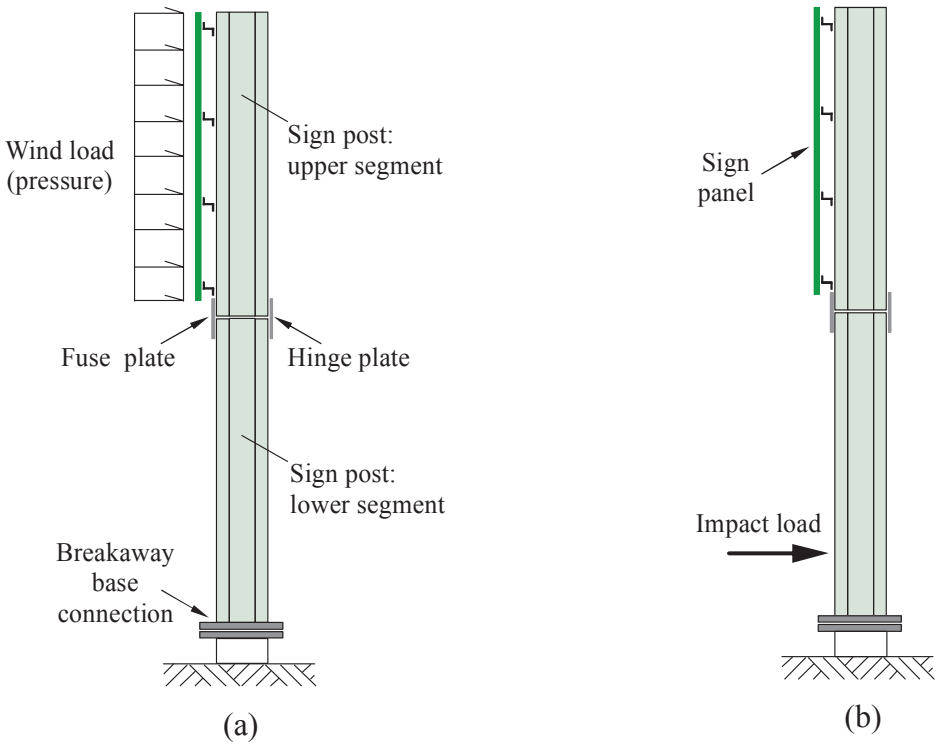

Figure 1.1 Design loading conditions on a roadside sign structure:
(a) Wind loading applied to sign panel; (b) Vehicle impact loading applied to post

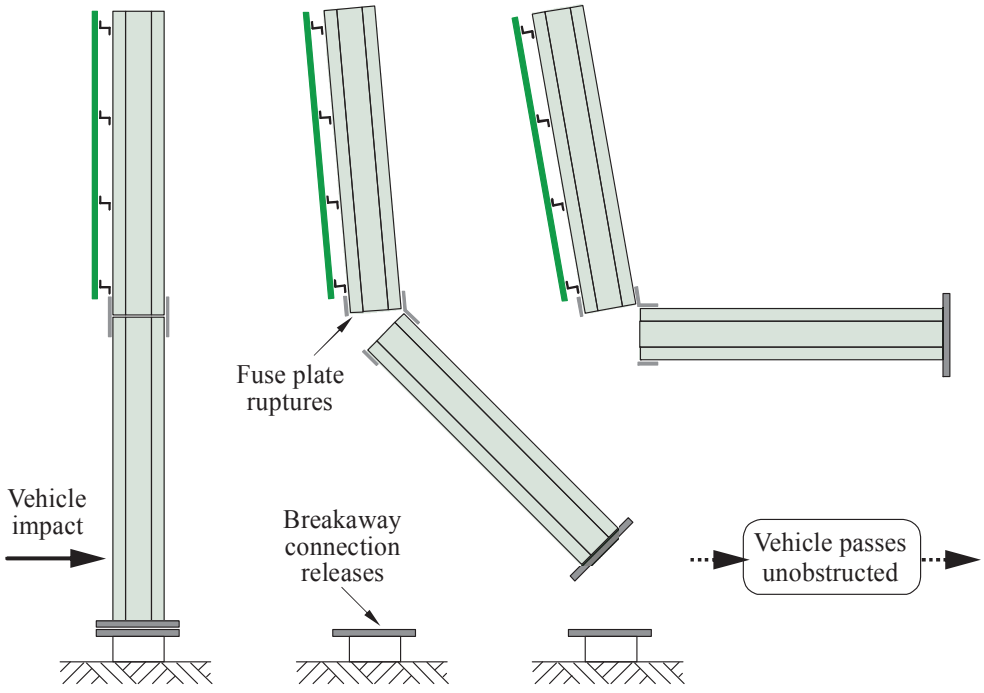

Figure 1.2 Intended breakaway behavior under vehicle impact loading conditions

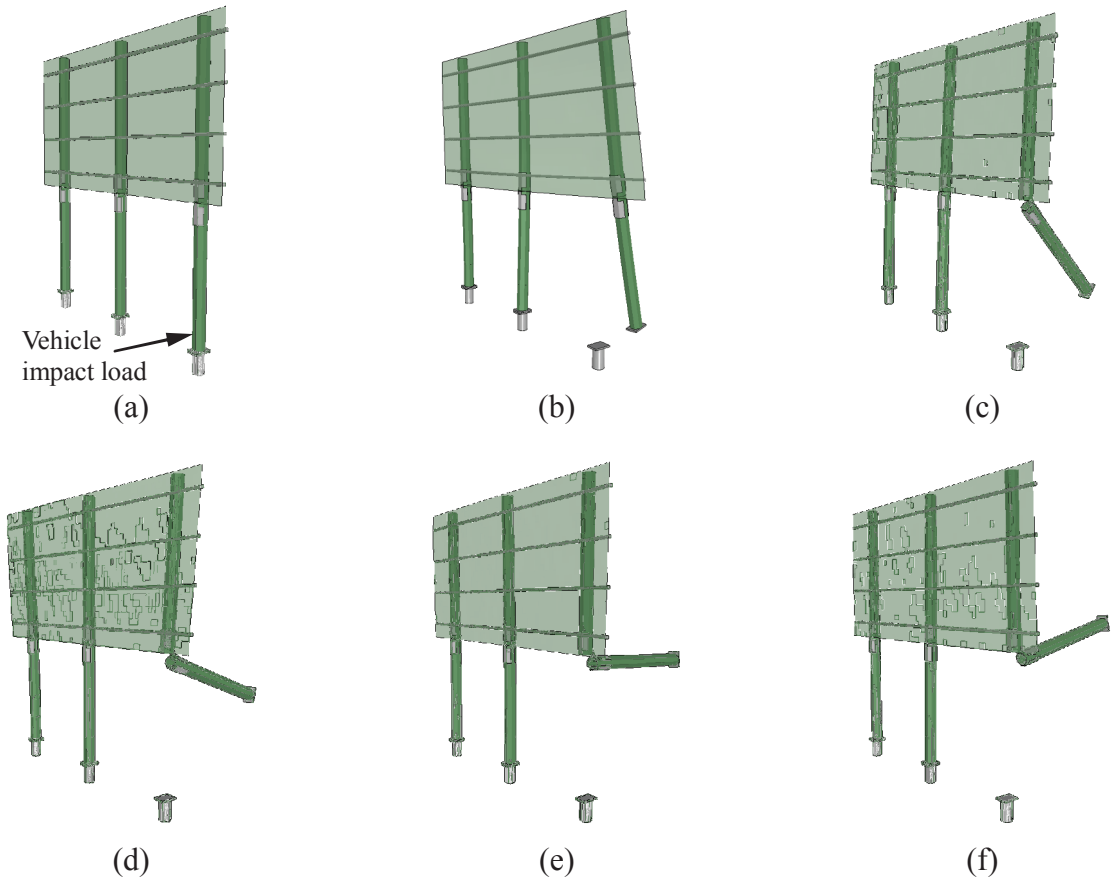

Figure 1.3 Intended system behavior of a three-post sign structure:
(a) Impact load from vehicle (not shown) is applied to right most column; (b) Breakaway base connection disengages; (c) Fuse plate at top of lower segment ruptures; (d)-(e) Lower post segment rotates out of path of vehicle, but remains attached to the rest of the structure

1.1.1 Related FDOT research

In a previous study conducted for the FDOT (BDK75-977-40, Consolazio et al. 2012), a new type of high capacity breakaway connection system (Figure 1.4) was developed for large roadside sign structures that utilize steel 'wide flange' sections as posts. Referred to as a 'shear-controlled moment-resisting collar' connection—or more simply a 'moment collar'—this system possessed a design wind moment capacity of ~100 kip-ft, and was experimentally demonstrated to possess an ultimate flexural capacity of ~150 kip-ft (i.e., producing a factor of safety FS>1.5).

In a subsequent and related FDOT study (BDV31-977-24, Consolazio and Innocent 2016), the target design life for breakaway connection development was reduced from 50 years to 10 years which, per AASHTO LTS-6 (2013), reduced the design wind loading and the required flexural capacity. A lighter and structurally simplified/optimized version of the high capacity moment collar connection was thus developed (Figure 1.5) to possess a design moment capacity of 80 kip-ft. Static flexural testing demonstrated that this connection possessed an ultimate flexural capacity in excess of (FS=1.5)(80 kip-ft) = 120 kip-ft. As part of this same study, medium capacity and low capacity versions of same connection were also developed. The

low capacity version of the connection (Figure 1.6) possessed a design wind moment capacity of 30 kip-ft, and an ultimate flexural capacity in excess of (FS=1.5)(30 kip-ft) = 45 kip-ft.

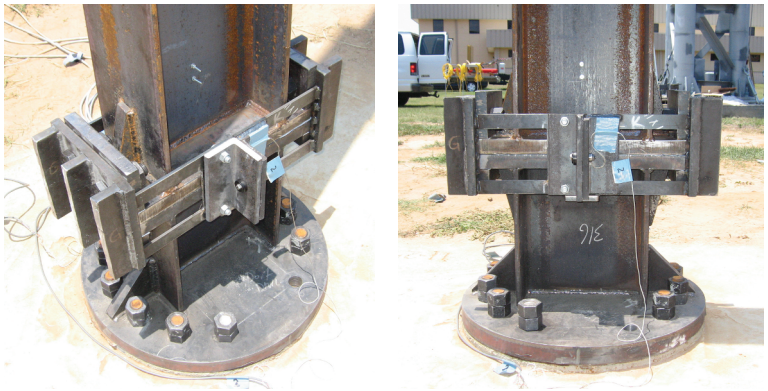

Figure 1.4 High capacity moment collar breakaway connection developed in FDOT project BDK75-977-40

Figure 1.5 High capacity moment collar breakaway connection developed in FDOT project BDV31-977-24

Figure 1.6 Low capacity moment collar breakaway connection developed in FDOT project BDV31-977-24

1.2 Objectives

All of the structural systems developed in BDK75-977-40 and BDV31-977-24 employed steel wide-flange sections as support posts, and steel breakaway connection components. In the present study, a primary objective was to investigate whether lighter-weight FRP composite materials could be incorporated into the design of breakaway sign structures so as to reduce occupant risk, improve safety, and possibly simplify field installation procedures. Primary focus was given to the development of 'hybrid' systems that utilize FRP composite structural shapes as support posts, but steel components in the breakaway base connections.

Complementing the hybrid connection development process were associated research objectives related to conducting physical pendulum impact testing of breakaway hardware. The AASHTO MASH (2009) standards require testing of roadside safety hardware with—among other vehicles—a 1,100 kg passenger car; denoted the '1100C vehicle'. However, while production vehicles such as the Kia Rio conform to the MASH 1100C vehicle specification, corresponding crushable-nose 'surrogate' vehicles, which are employed in pendulum impact testing, had not been developed when this study began. Consequently, developing an AASHTO MASH compliant 1100C surrogate vehicle for use in low speed (19 mph, per AASHTO MASH) pendulum impact testing of breakaway hardware was a key objective of this study. Also relating to pendulum impact testing, an associated objective of this study was to assess the scope of effort that would be required for the FDOT pendulum impact test facility to gain internationally recognized ISO 17025 laboratory accreditation.

1.3 Scope of work

- Development of a MASH-compliant surrogate 1100C test vehicle: Using impact force and vehicle deformation data obtained from full-scale crash testing of a 2006 Kia Rio production vehicle, a new crushable-nose surrogate vehicle was designed, fabricated, and experimentally validated. Intended for use in low speed (19 mph) pendulum impact testing of breakaway roadside hardware, the new UF/FDOT surrogate vehicle incorporates innovative design concepts to improve the accuracy of representation of the target production vehicle.
- Development of hybrid 'shear collar' breakaway connection: A hybrid breakaway sign post system in which a steel 'shear collar' is used to cut through an FRP sign post under direct vehicular impact was designed, fabricated, and experimentally tested. The FRP composite post used in this system ran continuous—without breaks/splices—from foundation to top of sign.
- Development of hybrid 'moment collar' breakaway connection: A breakaway sign post system consisting of a hybrid adaptation of the low capacity all-steel moment system shown previously in Figure 1.6 was designed, fabricated, and subjected to both pendulum impact testing and static flexural capacity testing.
- Determine accreditation requirements for FDOT impact pendulum: A thorough review of the process required to gain ISO 17025 laboratory accreditation for the FDOT pendulum impact facility was carried out, including acquisition and review of ISO 17025 accreditation documents, and examples of 'quality management system' (QMS) documentation produced by other state research labs.

CHAPTER 2
DESIGN BASIS AND APPROACH

2.1 Introduction

Documented and discussed in this chapter are the wind load resistance requirements (e.g., flexural strength) and vehicle impact performance requirements (e.g., limits on OIV) that were employed in this study to develop hybrid breakaway connection systems.

2.2 Review of design specifications

2.2.1 Review of specifications relating to wind load capacity

All AASHTO LTS-6 (2013, 2015) design requirements relating to wind load and load combinations were reviewed in detail for this study. In addition, the FDOT LTS-6 (2015) requirements, i.e., FDOT's modifications to AASHTO LTS-6, were also reviewed as were the FDOT SDG (2015) requirements, as they relate to wind load determination.

2.2.2 Specifications relating to vehicle impact load and breakaway connection performance

A comprehensive review of AASHTO MASH (2009) was conducted to establish design, testing, and performance requirements for the hybrid breakaway connections developed in this study. Additionally, a review of breakaway sign support requirements set forth in AASHTO LTS-6 (2013, 2015) was also conducted. On several important items, requirements set forth in AASHTO LTS-6 for breakaway supports (e.g., Chapter 12) complement those contained in AASHTO MASH. For example, the factor of safety required from breakaway connection ultimate strength testing; treatment of dead and wind load combinations; permissible residual breakaway stub height; etc. are all specified in AASHTO LTS-6.

It is also important to note that, in regard to 'breakaway connection dynamic performance' (i.e., vehicle impact loading), AASHTO LTS-6 references older vehicle impact test requirements from NCHRP 350 (Ross et al. 1993) rather than newer requirements contained in AASHTO MASH (2009). To ensure that the breakaway connections developed and tested in this study meet *modern* impact performance requirements, all connections were designed to meet the more stringent AASHTO MASH requirements rather than the older NCHRP 350 requirements.

2.3 Design basis

2.3.1 Wind load and steel component capacity

Structural selection and design of FRP composite sign posts, breakaway base connection components (plates, bolts, etc.), and related additional components, such as fuse plates and hinge plates, were based on the wind load and FRP capacity specifications contained in AASHTO LTS-6 (2013, 2015), FDOT LTS-6 (2015), and FDOT SDG (2015). In Table 2.1, a summary is provided of the design parameters from these specifications that were most pertinent to the present study. In a separate and parallel study (BDV31-977-24, Consolazio and Innocent 2016), the wind load specifications cited in Table 2.1 were used to establish and define 'design wind moment' capacities for high capacity, medium capacity, and low capacity breakaway connection systems. As was noted in Section 1.1.1, the design wind moment of the low capacity connection

in BDV31-977-24 (Consolazio and Innocent 2016) was defined as 30 kip-ft. In the present study, the hybrid connection systems developed were also defined as 'low capacity' and were thus assigned a 'design wind moment' capacity of 30 kip-ft. Accordingly, based on Table 2.1, the required ultimate flexural capacity of FRP posts used in the hybrid connections was (FS=2.0)(30 kip-ft) = 60 kip-ft, and the required ultimate flexural capacity of the steel breakaway connection components was (FS=1.5)(30 kip-ft) = 45 kip-ft.

Table 2.1 Specifications relating to wind load and FRP component capacity

Document	Section	Parameter	Design basis
FDOT LTS-6	3.8.3	Design life	Table 3-3, roadside sign structures: 10 year
FDOT LTS-6	3.8.2	Basic wind speed	FDOT LTS-6 cites FDOT SDG for wind speed
FDOT SDG	2.4.1	Basic wind speed	FL coastal county wind speed chosen: V = 150 mph
AASHTO LTS-6	3.4	Group II loads (DL+W)	Allowable stress increase for post = 33%
AASHTO LTS-6	8.7	Factor of safety: FRP post	FS $\geq$2.0 for ultimate strength from flexural testing
AASHTO LTS-6	12.4	Group II loads (DL+W)	Allowable load increase for connection = 0%
AASHTO LTS-6	12.4	Factor of safety: connection	FS $\geq$1.5 for ultimate strength from flexural testing
N/A	N/A	Number of sign posts	Sign structures with 2 or 3 posts will be considered
N/A	N/A	Steel yield strength	Fy = 50 ksi for breakaway connection components

2.3.2 Vehicle impact load and breakaway connection performance

Impact design requirements for hybrid breakaway sign structures developed in this study were based on vehicle impact conditions and breakaway performance criteria set forth in AASHTO MASH (2009) and AASHTO LTS-6 Chapter 12 (2013, 2015). Requirements from these specifications that were pertinent to the present study are summarized in Table 2.2. Structural adequacy under impact conditions requires that breakaway supports shall readily fail in a predictable manner by breaking, fracturing, or yielding when struck head-on (or at an angle of 25 degrees) by a standard MASH 1100C passenger car with a mass of 1,100 kg (2,420 lbf.) at a nominal speed of 19 mph (30 kph) for a low speed impact. The 1,100 kg mass is representative of small passenger cars such as the Kia Rio or Toyota Yaris.

With respect to occupant risk factors, AASHTO MASH limits the longitudinal occupant impact velocity (with respect to the interior surface of the passenger compartment) to no greater than 16 ft/sec, with values less than 10 ft/sec being preferred. Maximum allowable occupant deceleration is limited to 20.49 g, but preferably should not exceed 15 g. Detached elements (debris) from the breakaway support are not permitted to penetrate, or show potential for penetrating, the vehicle occupant compartment or present an undue hazard to other traffic, pedestrians or personnel in a nearby work zone. Potential for serious injury to vehicle occupants, due to deformation of the occupant compartment, is not acceptable.

Low speed (19 mph) passenger car (1100C) impact conditions typically yield the most severe occupant risk values when developing and testing breakaway roadside sign structures. With relatively small mass (m), and impacting at low speed (velocity, v), minimal kinetic energy ($\frac{1}{2}mv^2$) is available to activate the breakaway device, and to accelerate the lower post leg out of the path of the vehicle. OIV and vehicle compartment intrusion risks tend to be maximized during such conditions. Consequently, low speed 1100C impacts were the focus of the present study. However, it must be noted that MASH also references impact conditions involving a more massive 2270P vehicle (a 2,270 kg pickup truck). With greater mass (than the 1100C vehicle), and greater kinetic energy available to activate the breakaway device and accelerate the lower

post leg out of the vehicle path, the OIV and vehicle compartment intrusion risks associated with the 2270P vehicle were expected to be less severe than those associated with the 1100C vehicle.

Supplementing the AASHTO MASH criteria, AASHTO LTS-6 provides additional requirements to ensure predictable and safe performance. For example, to prevent a vehicle from snagging after breaking a support post away from the base, AASHTO LTS-6 limits the maximum residual stub height to 4 in.

Table 2.2 Vehicle impact load and breakaway connection performance requirements

AASHTO document	Section	Parameter	Requirement
MASH	2.1.1	Passenger car (1100C) mass	2420 ± 55 lbf (1100 ± 25 kg)
MASH	2.2.4.1	Test 3-60 impact speed	19 mph (30 kph)
MASH	2.2.4.1	Test 3-60 kinetic energy	$\leq$34 kip-ft ($\leq$20% in excess of target)
MASH	2.2.4.1	Evaluation criteria	B, D, F, H, I, N in MASH Section 5.3
MASH	2.2.4.1	Impact angles, min. and max.	$\theta = 0$ deg. and $\theta = 25$ deg.
MASH	2.2.4.1	Impact location	At transverse centerline of crushable nose
MASH	4.2.2	Surrogate vehicle type	Crushable nose impactor based on Kia-Rio
MASH	4.2.2	Roof/windshield impact	Assessed via impact test and FEA simulation
MASH	5.3	Table 5-1, Criteria B	Breakaway connection shall readily activate
MASH	5.3	Table 5-1, Criteria D	Detached fragments will not show potential for danger
MASH	5.3	Table 5-1, Criteria F	Vehicle shall remain upright after collision
MASH	5.3	Table 5-1, Criteria H	Occupant impact velocity $\leq$10 ft/sec (preferred)
MASH	5.3	Table 5-1, Criteria H	Occupant impact velocity $\leq$16 ft/sec (maximum)
MASH	5.3	Table 5-1, Criteria I	Occupant ride-down acceleration $\leq$15 g (preferred)
MASH	5.3	Table 5-1, Criteria I	Occupant ride-down acceleration $\leq$20.49 g (maximum)
MASH	5.3	Table 5-1, Criteria N	Acceptable vehicle trajectory behind test article
MASH	A5.3	Flail-space model	Longitudinal occupant flail distance = 2 ft
MASH	A5.3	Flail-space model	Use trapezoidal integration of accelerometer data
LTS-6	12.5.1	Impact test criteria	NCHRP 350 indicated but MASH will be used instead
LTS-6	12.5.3	Residual stub height	Stub height after connection 'breakaway' $\leq$4 in.
LTS-6	12.5.3	Sign post hinge elevation	Shall be $\geq$7 ft above ground
LTS-6	12.5.3	Sign post weight (per ft)	If post spacing $\geq$7 ft , max post weight = 45 lbf/ft
LTS-6	12.5.3	Sign post weight (total)	Total post weight, from slip plane to hinge, $\leq$600 lbf

2.4 Design approach

The overall approach used to design hybrid breakaway sign structures, for the wind load and impact performance criteria described above, involved combining the following:

- Use of applicable design aids: Standard structural design aids, such as AASHTO LTS-6, the AISC steel design specifications (AISC 2005), structural data from FRP materials providers, etc. were used to size/select/design various components of candidate breakaway system designs.
- Finite element modeling and simulations: Finite element modeling and *quasi-static* 'pushover' simulations were used to analytically quantify the ultimate flexural capacity of various steel components in the hybrid connection designs. Similarly, finite element modeling and *dynamic* impact simulations were used to quantify occupant risk factors, such as OIV, for candidate breakaway system designs.

- Static flexural testing: Static flexural tests of FRP posts were conducted at the FDOT Structures Research Center to experimentally quantify ultimate flexural capacity. Static flexural tests of hybrid 'breakaway connection and post' assemblies were conducted at the University of Florida to experimentally quantify ultimate flexural capacity.
- Pendulum impact testing: Pendulum impact tests of single-post breakaway systems were conducted at the FDOT Structures Research Center to experimentally evaluate system performance and to quantify occupant risk measures for candidate designs.

To facilitate pendulum impact testing of candidate breakaway systems, a new 1100C surrogate vehicle was developed and validated (as described in the following chapter).

CHAPTER 3
SURROGATE VEHICLE DEVELOPMENT

3.1 Introduction

Development of new roadside hardware (e.g., breakaway sign supports) requires that such systems meet the requirements set forth in applicable design standards. These standards specify both vehicle impact conditions that must be considered (e.g., vehicle mass, impact speed, impact angle) as well as system performance criteria that must be satisfied (e.g., measures of occupant risk). Moreover, such standards are not static in nature, but instead undergo periodic updates to reflect evolving changes in the vehicle fleet, advances in safety technology, and past lessons learned. Recent documents that have set forth impact performance requirements for breakaway hardware include National Cooperative Highway Research Program (NCHRP) Report 350 (Ross et al. 1993) and the American Association of State Highway and Transportation Officials (AASHTO) Manual for Assessing Safety Hardware (MASH 2009). For breakaway support structures, such as sign posts, NCHRP 350 required that adequate system performance be demonstrated by impact testing with a small car (an 820 kg [1,800 lbf] car, denoted the 820C test vehicle). With the publication of MASH, which replaced NCHRP 350, the 820C vehicle was replaced with a passenger car (1,100 kg [2,420 lbf] car, denoted the 1100C test vehicle) as well as modified impact conditions (speed and angle); testing using a light truck (a 2,270 kg 5,000 lbf] pickup, denoted the 2270P test vehicle) was also introduced as a requirement for breakaway supports.

In the design of breakaway systems that need to be applicable over a wide range of traffic speeds, the low speed, passenger car (1100C) impact conditions set forth in MASH can, in many cases, be the most challenging design conditions to satisfy. At low speed, and with substantially less mass than a 2270P light truck, the 1100C car possesses minimal impact energy with which to activate a breakaway device. As a consequence, substantial negative vehicle accelerations may occur, thereby increasing occupant risk measures (e.g., occupant impact velocity, OIV). Given the design challenges associated with such scenarios, developing cost-effective methods of experimentally evaluating breakaway device performance under low speed, passenger car impact conditions is of interest. A surrogate vehicle, with a crushable nose that employs low-cost, easily-replaceable aluminum honeycomb cartridges, provides one such option. When used in conjunction with a gravity pendulum a crushable nose impactor provides an efficient means of experimentally testing new breakaway concepts, identifying potential design flaws, and evaluating key occupant risk measures (e.g., OIV). It is acknowledged that pendulum testing alone is not sufficient to evaluate roof crush or occupant compartment penetration, and that supplementary full-scale production vehicle crash testing may be required. However, design improvements made in response to pendulum testing outcomes will typically enhance the probability of successful production vehicle testing, and thus surrogate vehicle testing remains a valuable evaluation tool.

Since a crushable nose impactor serves as a surrogate (or ‘stand-in’) for a production vehicle, the aluminum honeycomb cartridges in the crushable nose must be designed to reasonably replicate the force-deformation behavior of a corresponding production vehicle. Data used in the cartridge design process must thus be obtained from impact testing of production vehicles. Many implementations of this process have occurred in the past. For example, impact testing of a 1979 Volkswagen Rabbit produced force-deformation data (Figure 3.1a) that were used to design an early crushable nose impactor for the FHWA (Federal Highway

Administration) FOIL (federal outdoor impact laboratory) gravity pendulum. More recently (Marzougui et al. 2011, Marzougui et al. 2013), rigid pole impact testing of a 2006 Kia Rio produced data (Figure 3.1b) that were used to design an updated, MASH-compliant crushable nose 1100C surrogate vehicle (Figure 3.2). Employing a total of eleven (11) consumable aluminum honeycomb cartridges, the NCAC (National Crash Analysis Center) FOIL impactor shown in Figure 3.2 was designed for deformations up to approximately 28 in. (Figure 3.1b). [Note that reproducing the entire range of deformation from the 31 mph Kia Rio test would only be necessary in higher speed impact testing of systems with significant impact resistance (e.g., crash terminals).] As is typical of crushable-nose impactor designs, the system in Figure 3.2 uses a series of aluminum honeycomb cartridges, of varying dimensions and crush-strengths, to successfully approximate the production vehicle force-deformation curve.

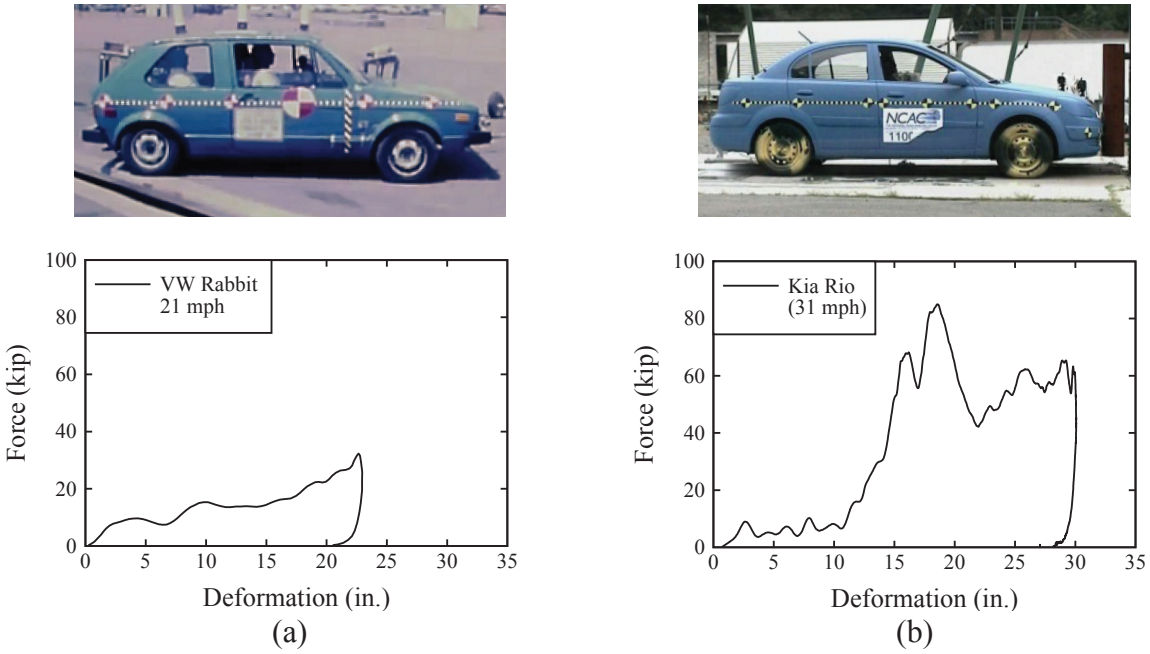

Figure 3.1 Production vehicles and force-deformation data:
(a) 1979 VW Rabbit and 21-mph crash test results
(National Highway Traffic Safety Administration and Federal Highway Administration);
(b) 2006 Kia Rio and 31-mph crash test results
(National Crash Analysis Center, Marzougui et al. 2011)

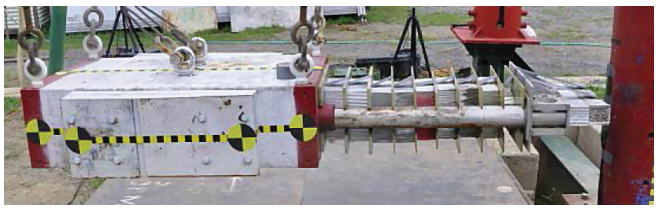

Figure 3.2 NCAC-FOIL 1100C crushable nose impactor
(National Crash Analysis Center, Marzougui et al. 2013)

3.2 Low speed crushable nose with trapezoidal cartridges

Concurrent with the efforts of Marzougui et al. (2013), the University of Florida (UF) and the Florida Department of Transportation (FDOT) used the Kia Rio test data (Marzougui et al. 2011), to design an alternative 1100C crushable nose impactor for use with the FDOT gravity pendulum, located at the Marcus H. Ansley Structures Research Center in Tallahassee, Florida. Designed by UF, and fabricated and operated by FDOT, this high energy pendulum (Consolazio et al. 2012) is capable of swinging a 10,000-lbf impactor (Kantrales et al. 2015) through a drop height of approximately 20 ft to 25 ft (depending on impactor geometry). However, in regard to developing a new 1100C crushable nose impactor, specific interest was given to low energy, low speed (19 mph, as defined by MASH) impact testing of breakaway roadside hardware (e.g., sign supports).

Due to the focus on low speed impact conditions, the crushable nose was designed to reproduce only the portion of the Kia Rio curve that would be engaged (i.e., deformed) during a 19-mph impact. The kinetic energy of a 2,420-lbf (1100C) impactor traveling at 19 mph is approximately 350 kip-in. Integrating the Kia Rio force-deformation curve (Figure 3.1b) established that approximately 18 in. of deformation would be generated by a 19-mph impact. Therefore, development of the new crushable nose focused on reproducing the first 18 in. (the 'low speed impact range') of the Kia Rio test curve. Importantly, guidance received from the lead author of (Marzougui et al. 2011) indicated that the Kia Rio force-deformation curve could be considered to be approximately independent of impact speed, and thus applicable at speeds of both 31 mph (the Kia Rio test speed) and 19 mph (the focus herein). Consequently, developing a crushable nose that reproduced the Kia Rio curve, but only up to 18 in. of deformation (for 19 mph impacts), was confirmed to be a suitable design methodology.

Aluminum honeycomb cartridges used in previous crushable nose designs have typically been rectangular in geometry, with punch-outs used, as necessary, to achieve the desired cartridge strength. Each rectangular cartridge exhibits a nearly constant force level (Figure 3.3a) over a range of deformation nearly equal to the cartridge thickness. Beyond this deformation level, the cartridge stiffness is assumed to increase very rapidly. In a simplified static interpretation—excluding dynamic effects related to the mass of spacer plates, strain rate effects, etc.—a stack of rectangular aluminum honeycomb cartridges will model a production vehicle force-deformation curve in a 'stepwise constant' fashion (Figure 3.3c). Examples of crushable noses designed using rectangular cartridges include the NCAC-FOIL 820C crushable nose (and derivative designs used at other pendulum impact facilities), as well as the NCAC-FOIL 1100C crushable nose.

While rectangular cartridges offer certain advantages, an alternative approach—the use of tapered cartridges—was employed in the present study to improve the accuracy with which a production vehicle can be approximated. As Figure 3.3b illustrates, a linearly tapered (trapezoidal) cartridge, when crushed, exhibits a response curve in which the force varies linearly with increasing deformation. Crush force varies from an initial value to a final value in proportion to the surface areas of the smaller and larger faces of the cartridge, respectively. In a simplified static sense, a stack of tapered aluminum honeycomb cartridges will model a production vehicle force-deformation curve in a piecewise linear fashion (Figure 3.3d), thus improving the approximation.

While crushable nose response is primarily determined by static cartridge crush behavior, in a physical impact testing environment, secondary influences may be contributed by spacer plate inertial forces, strain rate effects, fabrication tolerances, and installation tolerances. Given

such influences, the force-deformation curve produced by use of tapered cartridges will not be precisely piecewise linear in form; neither will the curve produced by rectangular cartridges be precisely stepwise constant. However, matching a production vehicle curve to within a desired level of error (tolerance) is easier to achieve—from a design perspective—when using tapered cartridges, due to the improved approximation. Moreover, since tapered cartridges do not require the use of punch-outs, cartridge fabrication is simplified (since no punch-out process is needed). Conversely, it must be acknowledged that rectangular cartridges (with or without punch-outs) are very stable in terms of crushing behavior, and therefore more tolerant of installation misalignments.

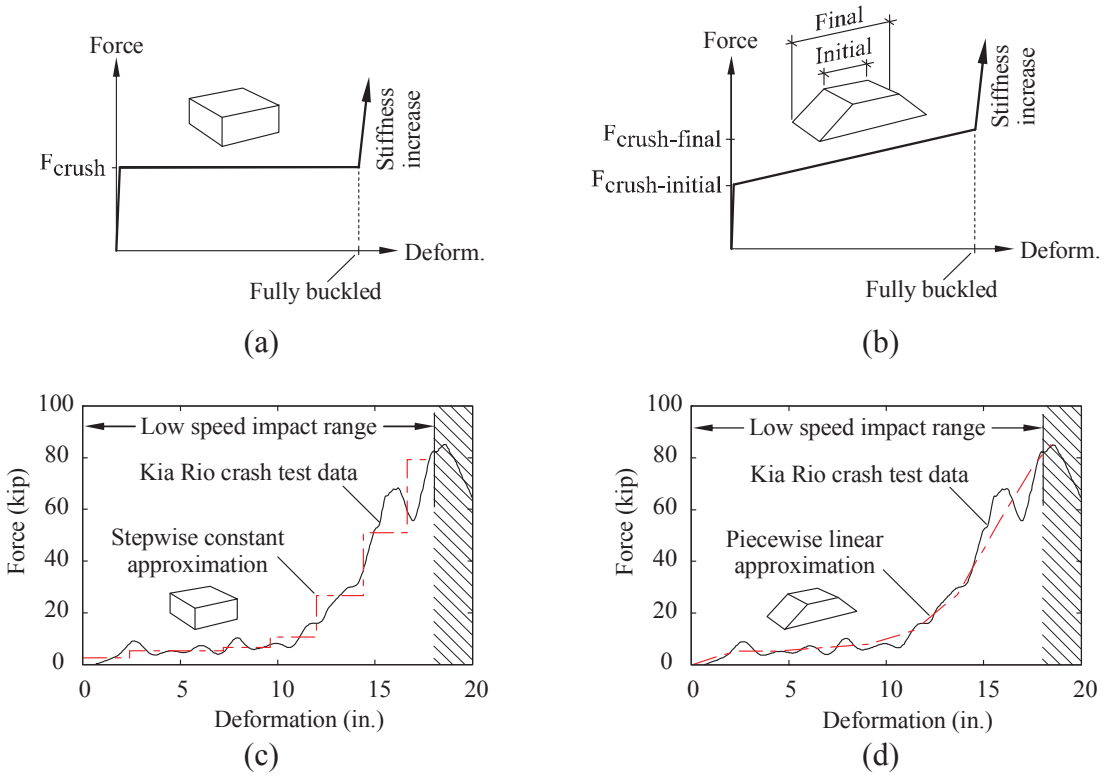

Figure 3.3 Simplified description of production vehicle force-deformation curve approximation: (a) Rectangular cartridge behavior; (b) Tapered (trapezoidal) cartridge behavior; (c) Stepwise constant approximation; (d) Piecewise linear approximation

3.3 Compression behavior of aluminum honeycomb

To generate data needed for the cartridge design process, static laboratory compression tests of aluminum honeycomb materials (Plascore aluminum CrushLite, 1/8 in. cell size) were conducted. As aluminum honeycomb is cellular in structure (Figure 3.4a), its compressive strength is determined by cell size and cell wall thickness, both of which influence the inelastic cell wall buckling that accompanies cartridge compression. Tests on rectangular and tapered cartridges (Figure 3.4b-d) were conducted using a 400 kip Tinius Olsen universal test machine (Figure 3.4e) to characterize the force-deformation relationships that arise during cell buckling. Of particular interest was quantifying the compression behavior of tapered cartridges. As

Figure 3.4f illustrates, in a tapered cartridge, the width of the buckled zone varies as deformation increases. Moreover, the 'state' of the material (i.e., buckled or unbuckled) is non-uniform across the width of the cartridge. Characterizing such behavior was a necessary prerequisite to designing tapered cartridges for use in the crushable nose.

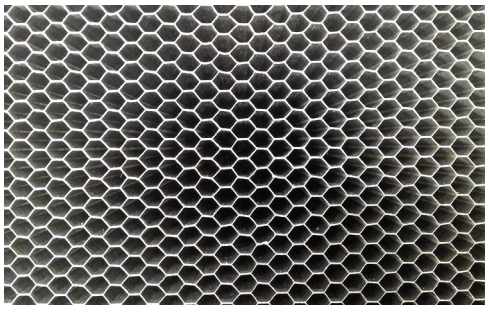

(a)

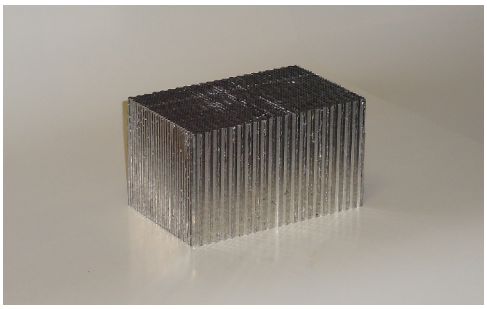

(b)

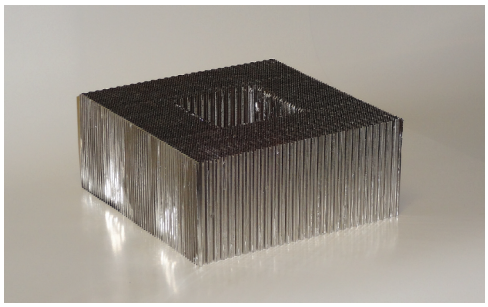

(c)

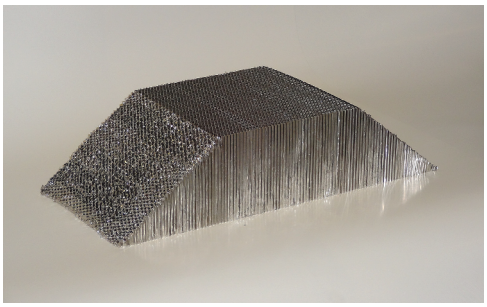

(d)

(e)

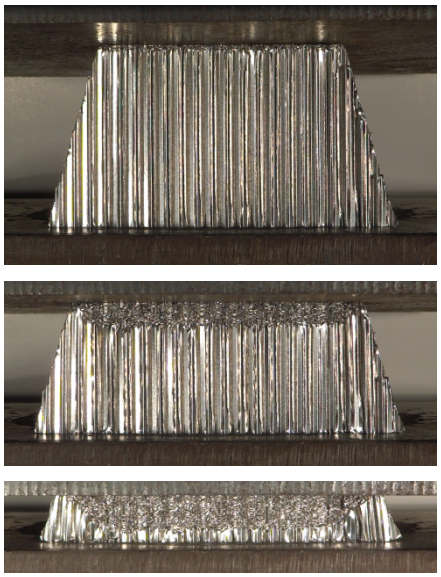

(f)

Figure 3.4 Aluminum honeycomb:
(a) Hexagonal honeycomb cell structure; (b) Rectangular cartridge;
(c) Rectangular cartridge with punch-out; (d) Trapezoidal cartridge;
(e) Cartridge in test machine; (f) Compression test of tapered cartridge

In Figure 3.5, various stages of honeycomb deformation are presented that were identified as being pertinent to crushable nose cartridge design. Mechanically upsetting the surface (Figure 3.5a) prevents the occurrence of a significant force spike that would otherwise be associated with the initiation of buckling. As load is applied, a locally buckled zone forms (Figure 3.5b). When all material in the cartridge has buckled, a 'fully buckled' stage is reached (Figure 3.5c) and the stiffness of the cartridge increases abruptly, as denoted previously in the simplified representations of Figure 3.3a-b. However, cartridge stiffness beyond the fully buckled stage cannot be assumed to be effectively infinite for crushable nose design. Although only moderate additional *deformation* occurs after this stage, significant *energy dissipation* can still take place that must be accounted for in design. As load increases further, the collapsed (thickened) cell walls buckle once again, but as a group (Figure 3.5d). Finally, at a sufficiently high load level, nearly all of the original void space in the material is filled and a state denoted 'fully compressed' is reached (Figure 3.5e).

Compression test data—spanning all of the deformation stages illustrated in Figure 3.5—are shown in Figure 3.6a-b for typical rectangular and tapered cartridges. Over a range of approximately 2.5 in. of deformation, crush forces are constant, or vary linearly, as expected for the rectangular and tapered cartridges, respectively. Beyond the fully buckled state, crush forces increase abruptly until, in each case, a second force plateau is reached. This second plateau corresponds to the onset of group buckling (Figure 3.5d). With further deformation, a second stage of material stiffening occurs as void space in the honeycomb collapses, after which the fully compressed state is approached. In each case, energy dissipation associated with the 'design response mode' (i.e., constant force, linear force) is followed by additional energy dissipation (Figure 3.6a-b) of nearly equal magnitude. As will be noted later, accounting for this additional component of energy dissipation was found to be important when designing smaller, tapered cartridges that are subjected to 'high-deformation' during impact—i.e., deformation between the fully bucked and fully compressed states.

Based on a series of tests similar to, and including, those shown in Figure 3.6a-b, a generalized procedure was developed for calculating idealized force-deformation curves (Figure 3.6c-d) for rectangular and tapered cartridges of arbitrary size and material strength. With the goal of representing the Kia Rio force-deformation curve in an approximately piecewise linear manner (Figure 3.3d), the calculation procedure was used to efficiently generate force-deformation curves for trial cartridge designs.

3.4 Numerical modeling and system design

Low degree-of-freedom one-dimensional dynamic analyses, employing idealized cartridge force-deformation curves, were initially used to iterate toward a candidate crushable nose configuration capable of adequately representing the Kia Rio. This preliminary design was subsequently expanded into a fully-discretized high-resolution finite element model of the entire crushable nose impactor (Figure 3.7a). Using the high-resolution model, simulations were conducted with LS-DYNA (LSTC 2014) to assess the dynamic performance of the impactor during 19 mph impacts against a 10 in. diameter rigid pole structure. To facilitate structural design of the aluminum impact head (Figure 3.7b) and attached tubes, simulations of intentionally non-ideal impact conditions were conducted (e.g., off-center and rotated impacts which to tend to 'rack' the nose assembly). Stresses obtained from such simulations guided the selection of plate thicknesses and tube-wall thicknesses.

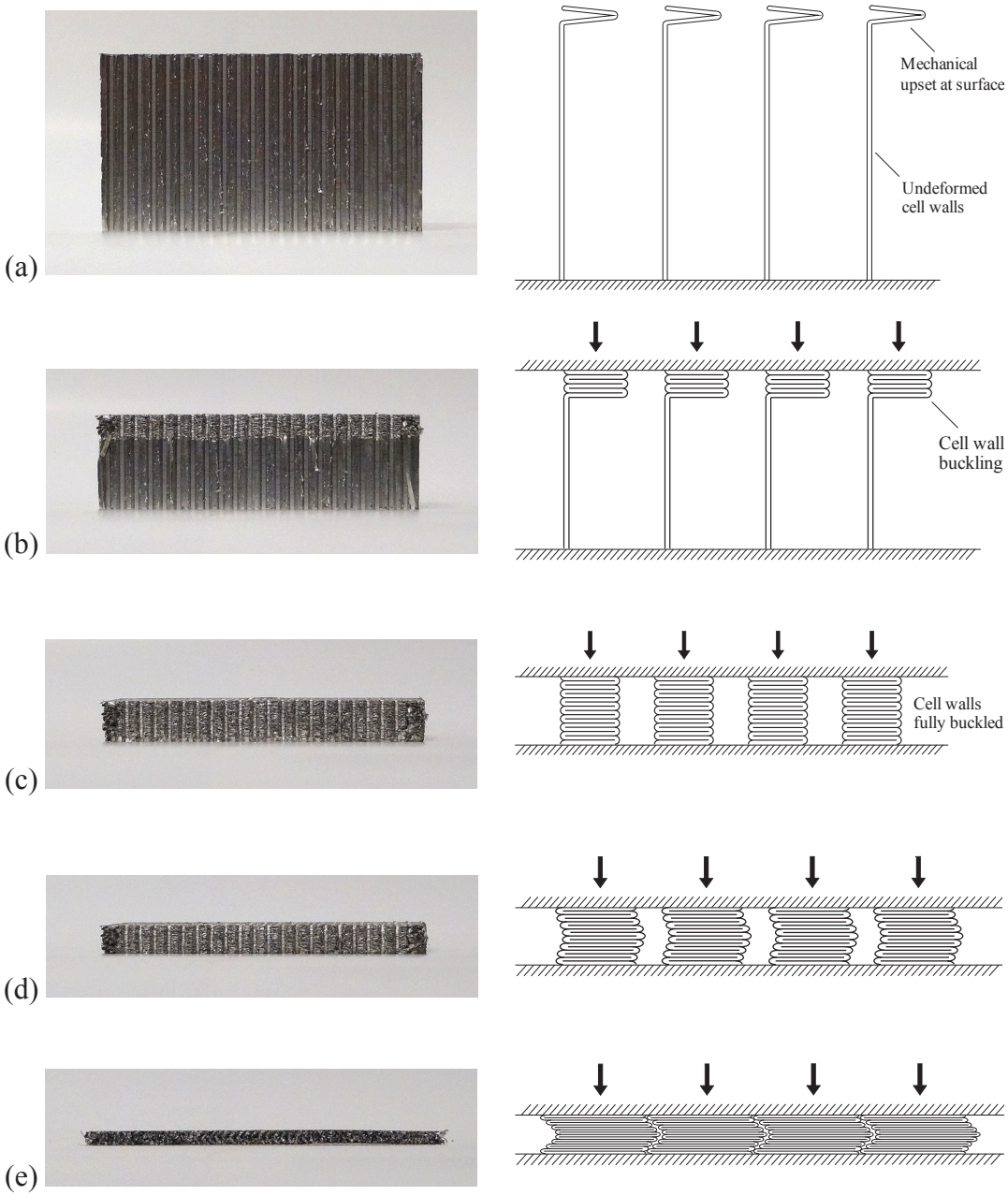

Figure 3.5 Stages of aluminum honeycomb compression behavior:
(a) Surface of cartridge mechanically upset; (b) Cartridge buckling in progress;
(c) Fully buckled stage; (d) Group buckling in progress; (e) Fully compressed stage

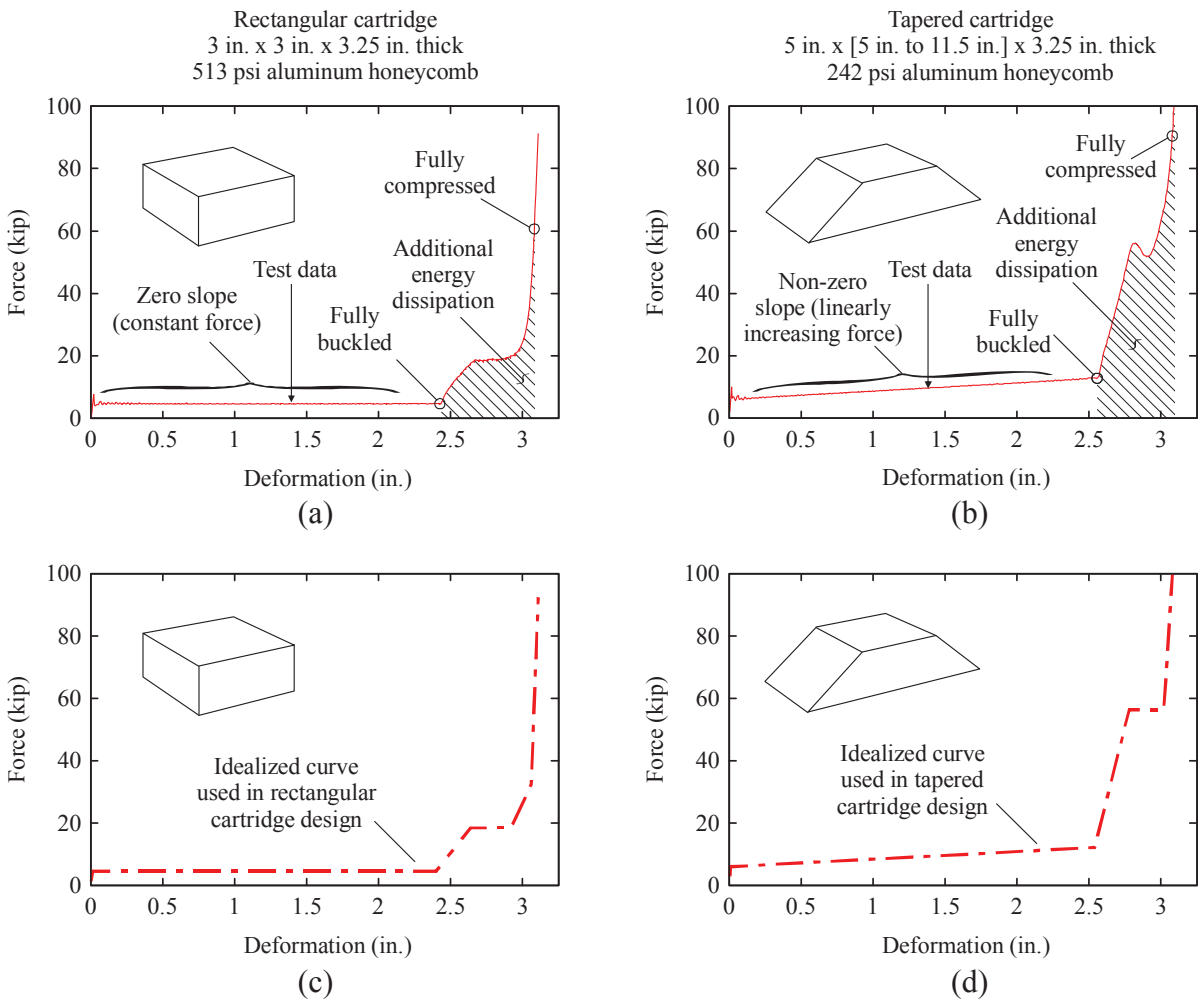

Figure 3.6 Compression test data and idealizations used in cartridge design:
(a) Rectangular cartridge test data; (b) Tapered cartridge test data;
(c) Rectangular cartridge idealization; (d) Tapered cartridge idealization

Impact simulations were also used to determine the necessary thicknesses and material properties of spacer plates that separate each set of adjacent cartridges. Tapered cartridges in the configured nose gradually increase in height from front to back (Figure 3.7c). Consequently, flexing of the spacer plates (Figure 3.7d) must be sufficiently minimized so that reasonably uniform deformation patterns are imposed on the cartridges. Initially, all cartridges were modeled using a continuum honeycomb material model. For certain tapered cartridge configurations, however, unacceptably slow simulation run-times resulted. Since experimental data from cartridge compression tests were available, a computationally efficient alternative approach was employed. In this approach, the idealized honeycomb force-deformation curve calculation procedure noted above was applied on a tributary area basis (Figure 3.8) to each cartridge, producing a grid of nonlinear springs. Using an automated spring generation procedure, appropriate nonlinear curves, element lengths, and gap distances (Figure 3.8) were configured for each spring. Contact definitions were then used to model interactions between the cartridge springs and spacer plates.

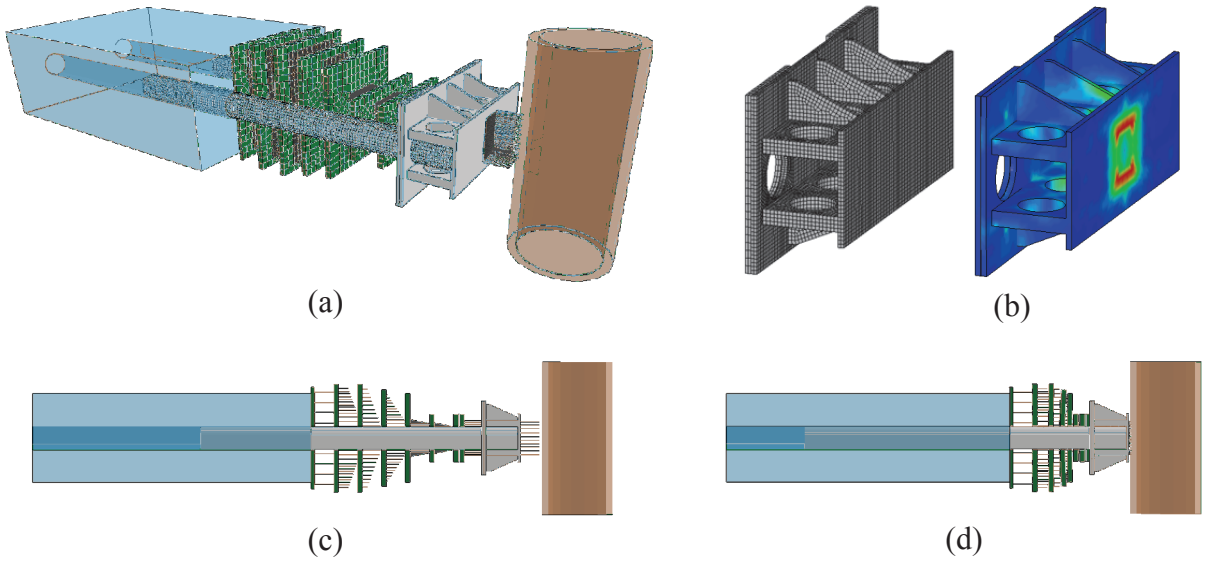

Figure 3.7 Finite element model of 1100C crushable nose surrogate vehicle: (a) Overview; (b) Impact head finite element mesh and typical stress results; (c) Prior to impact; (d) During impact

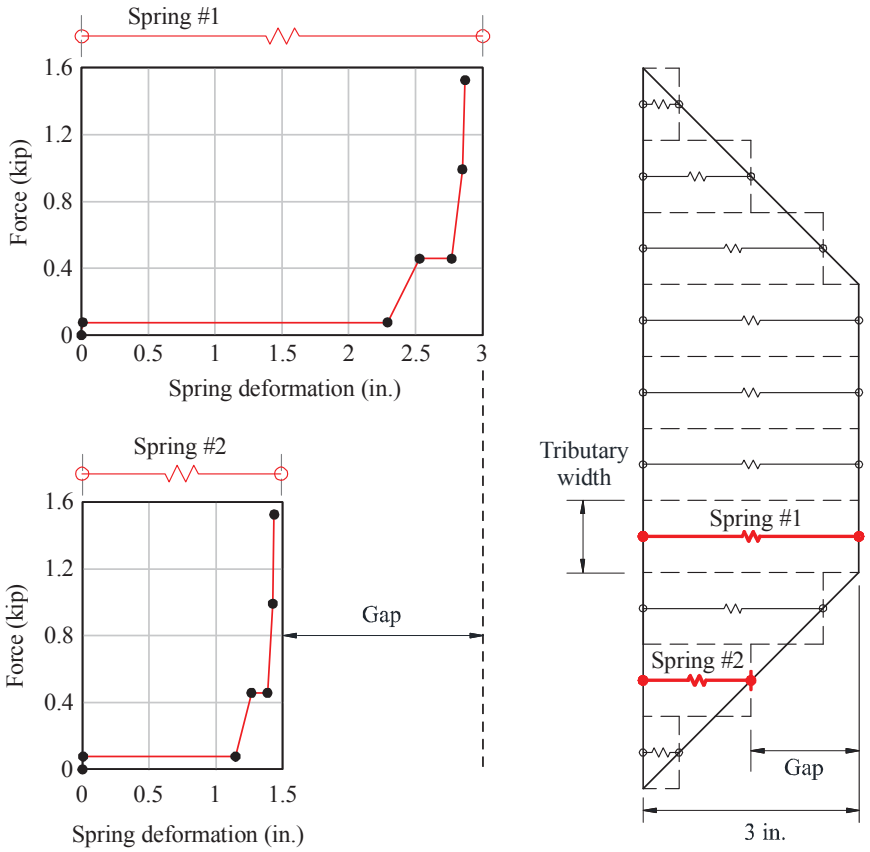

Figure 3.8 Use of nonlinear springs to efficiently model the compression behavior of an aluminum honeycomb cartridge

3.5 Crushable nose 1100C surrogate vehicle

Using finite element simulation results to guide the structural design process, the low speed 1100C surrogate vehicle (impactor) shown in Figure 3.9 was produced. Two major components make up the impactor—a crushable nose and a reinforced concrete back block. The weight of the crushable nose was minimized by fabricating the impact head assembly and attached telescoping tubes from lightweight 6061-T6 aluminum alloy (total weight: 68 lbf). Aluminum honeycomb cartridges, with strengths and dimensions as shown in Figure 3.10, were installed between high-strength, high-stiffness (G-11 glass epoxy laminate) spacer plates. Steel side plates of varying weights were attached, as needed, to the concrete back block to achieve a total impactor weight (including nose) of 2,420 lbf. To mitigate the influence of spacer plate inertial forces, each such plate was minimized in size based on the dimensions of the adjacent aluminum cartridges. Furthermore, friction between the telescoping aluminum tubes of the front block, and steel 'sleeve tubes' embedded within the back block, was virtually eliminated by permanently epoxying Teflon strips to the telescoping tubes, thereby eliminating all metal-to-metal contact.

As noted in Figure 3.10, the cartridge dimensions listed are based on the 'actual' (as-delivered) compressive strengths of the aluminum honeycomb materials acquired during this study. The 'specified' (ordered) material strengths are also included for reference. Tests conducted on subsequently acquired batches of honeycomb material have confirmed that moderate variations in strength (±15%) can be accommodated by inversely scaling the width dimensions listed in Figure 3.10 by the appropriate compressive strength ratio. For example, a 10% increase in material strength, relative to the 'actual strength' values listed in Figure 3.10, would require a 10% reduction of the listed cartridge width.

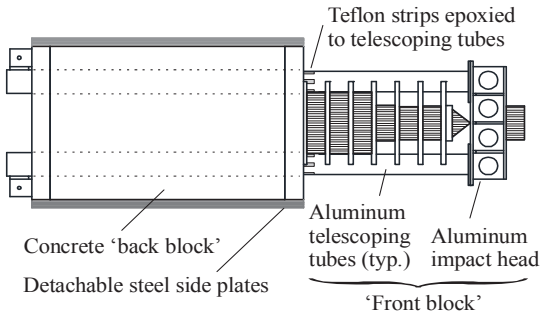

(a)

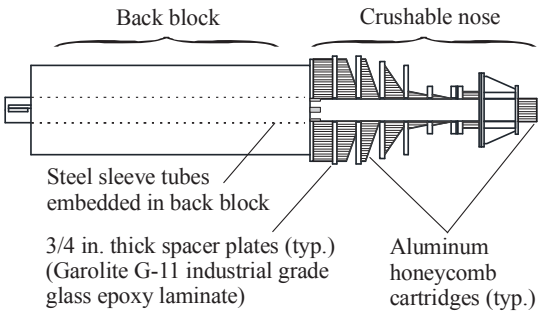

(b)

(c)

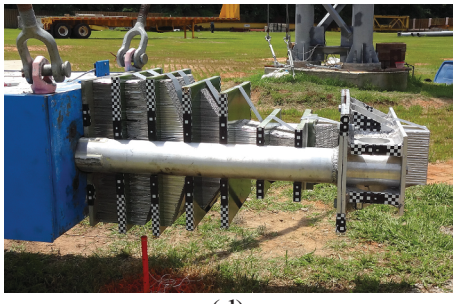

(d)

Figure 3.9 Crushable nose 1100C surrogate vehicle:
(a) Plan view schematic; (b) Elevation view schematic; (c) Overview; (d) Crushable nose detail

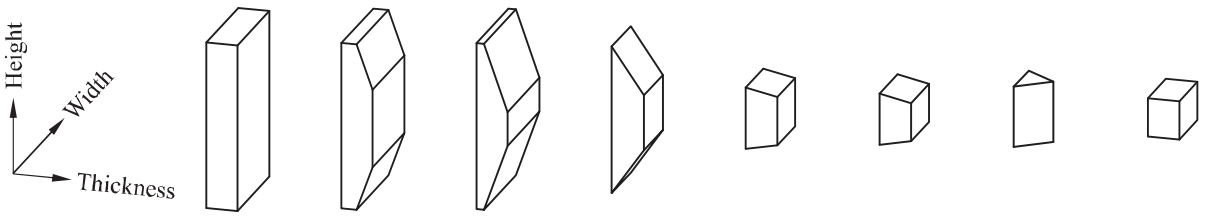

Cartridge #	8	7	6	5	4	3	2	1
Shape	Rect.	Trap.	Trap.	Trap.	Trap.	Trap.	Prism	Rect.
Compressive strength:								
Specified	550 psi	550 psi	550 psi	272 psi	272 psi	272 psi	272 psi	272 psi
Actual	513 psi	513 psi	513 psi	242 psi	242 psi	242 psi	242 psi	242 psi
Vertical height (based on actual compressive strength, not specified strength):								
Minimum.	16.0 in.	7.5 in.	3.25 in.	5.25 in.	4.63 in.	3.63 in.	5.75 in.	5.75 in.
Maximum	16.0 in.	16.0 in.	16.0 in.	14.0 in.	5.88 in.	4.88 in.	5.75 in.	5.75 in.
Lateral width (based on actual compressive strength, not specified strength):								
Minimum	10.38 in.	10.38 in.	10.38 in.	6.00 in.	5.63 in.	5.75 in.	0.00 in.	3.63 in.
Maximum	10.38 in.	10.38 in.	10.38 in.	6.00 in.	5.63 in.	5.75 in.	4.75 in.	3.63 in.
Thickness:								
Minimum	3.00 in.	1.46 in.	0.72 in.	0.00 in.	0.00 in.	0.00 in.	3.00 in.	3.00 in.
Maximum	3.00 in. †	3.00 in. †	3.00 in. †	3.00 in. †	3.00 in†.	3.00 in. †	3.00 in.	3.00 in. †

† Maximum thickness after cartridge pre-crushing. Material thickness prior to pre-crushing was 3.25 in.

Figure 3.10 Aluminum honeycomb cartridge characteristics

3.6 Validation pendulum impact testing

Successful validation impact testing of the crushable nose 1100C surrogate vehicle was conducted on 2013-05-09 using the gravity pendulum at the FDOT Structures Research Center. A drop height of 12 ft was used to generate a 19 mph impact against a rigid pole structure (Figure 3.11). To prevent rotation or translation, the 10 in. diameter concrete-filled steel pole was rigidly attached to a reinforced concrete foundation, and additionally attached to three reaction blocks through a stiff outrigger beam. Test instrumentation included two pairs of infrared optical break beam sensors (used to determine impact speed), a pressure sensitive tape switch (affixed to the face of the pole), four accelerometers, and two high speed video cameras. Break beam, tape switch, and accelerometer data were recorded at a frequency of 10 kHz, while high speed video was recorded at 2 kHz. A 250 *g* accelerometer was mounted to the aluminum impact head of the crushable nose, while a 50 *g* accelerometer was mounted at mid-length to the concrete back block. (Additional 30 *g* and 10 *g* accelerometers were also installed and recorded.) Total impact force was computed as the sum of front block force and back block force. Front block force was determined as the product of 68 lbf of aluminum weight multiplied by acceleration (in units of *g*) measured using the 250 *g* accelerometer. Similarly, back block force was determined as the product of 2,352 lbf of weight multiplied by acceleration (in units of *g*) measured using the 50 *g* accelerometer. Time varying crushable nose deformation was computed by tracking points in the high speed video (Figure 3.12) using the motion tracking (digital image correlation) software package Xcitex ProAnalyst.

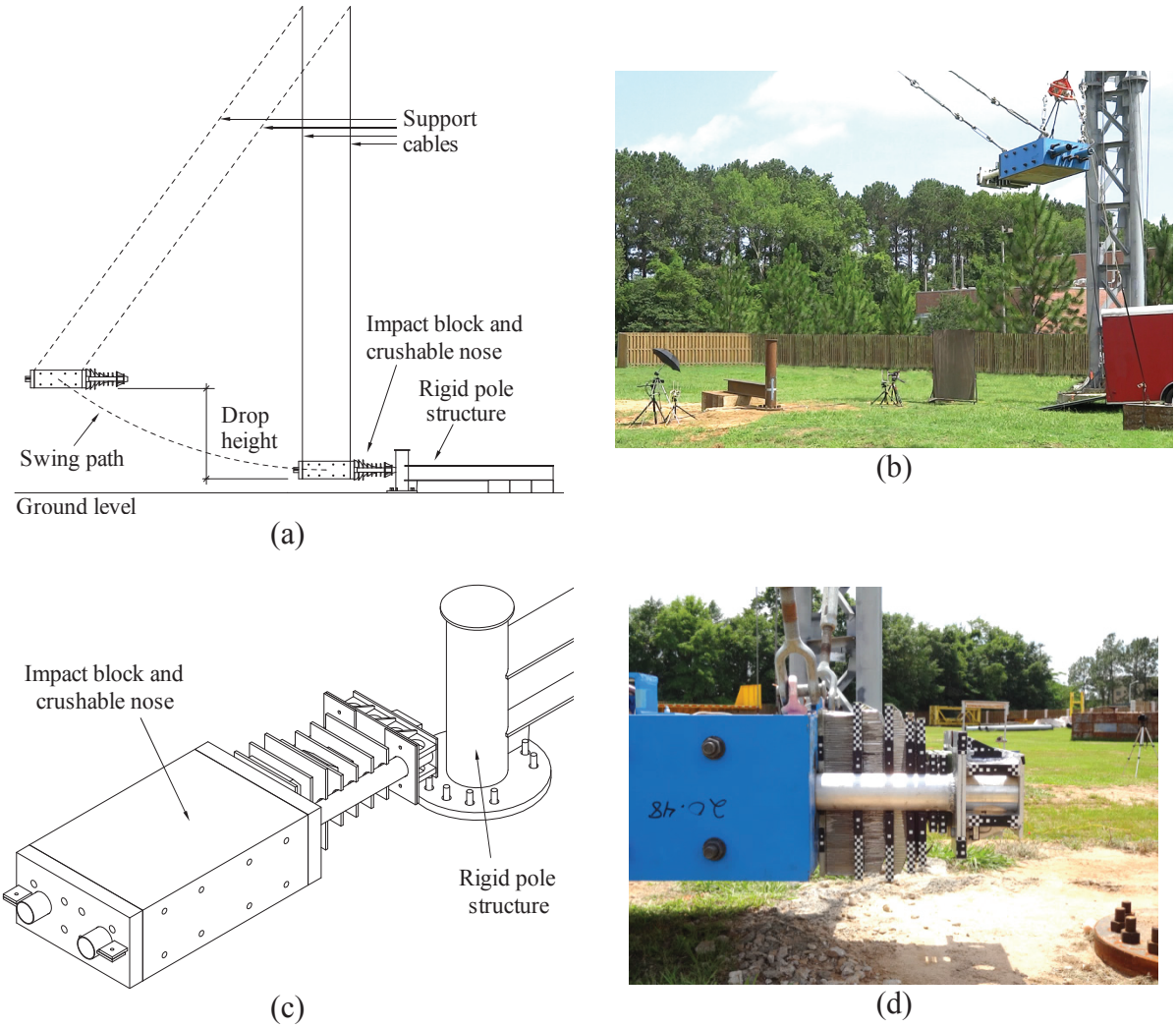

Figure 3.11 Rigid pole pendulum impact testing:
(a) Elevation schematic; (b) Test setup prior to release of surrogate vehicle;
(c) Isometric schematic; (d) Crushable nose after impact test

As Figure 3.11d and Figure 3.12d indicate, smaller cartridges near the front of the nose were subjected to high-deformation levels, and approached the 'fully compressed' stage shown earlier in Figure 3.5. Taking into account—during the cartridge design process—the energy dissipation associated with this stage of deformation was critical in terms of producing the desired force-deformation response. This is known with certainty because an earlier version of the nose, designed prior to conducting 'high-deformation' versions of the laboratory cartridge compression tests (described earlier), produced a force-deformation curve (obtained from pendulum impact testing) that deviated unacceptably from the Kia Rio curve. The source of the deviation was traced to energy dissipation at high-deformation (i.e., between the 'fully buckled' and 'fully compressed' deformation stages). Therefore, use of smaller tapered cartridges in lieu of larger, punched-out rectangular cartridges has advantages (linear force variation, simplified fabrication), but requires careful attention be given to energy dissipation at high-deformation levels.

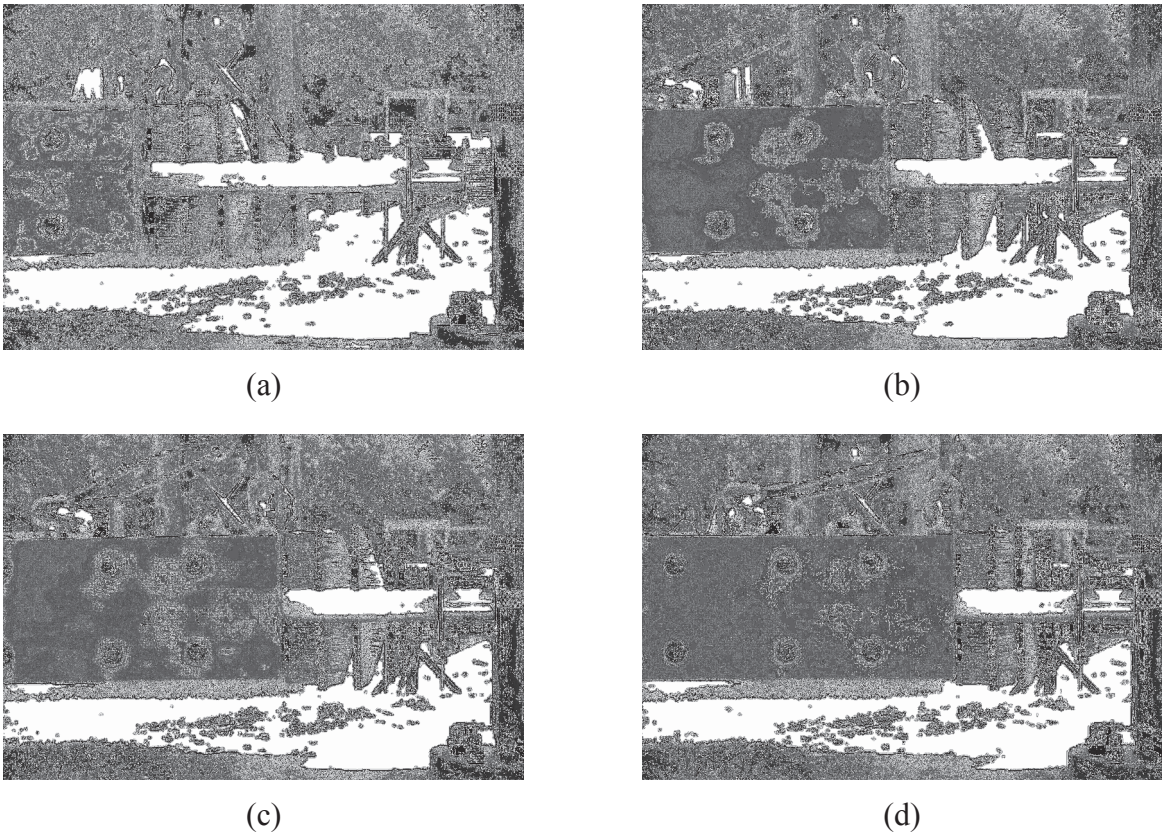

(a) (b)

(c) (d)

Figure 3.12 High speed video frames showing crushable nose deformation during rigid pole impact test

Force-deformation results obtained from the 2013-05-09 pendulum impact test are compared to the Kia Rio crash test (Marzougui et al. 2011) data in Figure 3.13. In general, the two curves are in good agreement, with the only significant differences occurring near the upper range of force and deformation. These differences were not the result of calibration error but rather of an intentional design decision. Upon careful review of the Kia Rio test data, the decision was made to design a crushable nose that would follow an 'average trend' from 15 in. to 18 in. of deformation. As noted earlier, by integrating the Kia Rio test data, maximum expected deformation for a low speed (19 mph) 1100C impact is approximately 18 in. This level of deformation, however, is only reached when the vehicle is brought to a complete stop (e.g., by striking a rigid object). For breakaway devices, the force required to activate the breakaway mechanism is typically far less than the maximum force levels shown in Figure 3.13. Consequently, low speed 1100C impacts on breakaway systems will typically generate far less than 18 in. of deformation. As such, approximating the upper range of the Kia Rio test data with an 'average trend' curve was deemed suitable for the intended application.

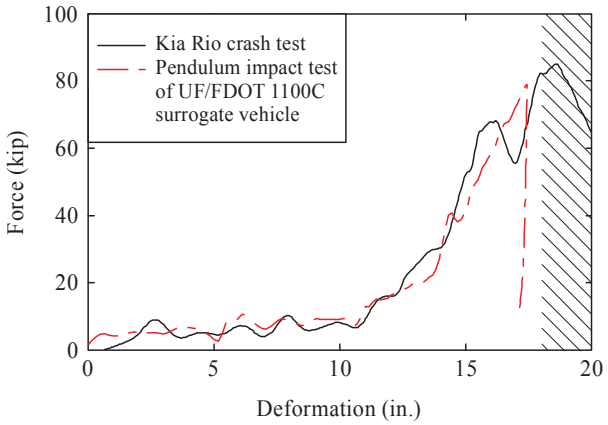

Figure 3.13 Comparison of production vehicle and surrogate vehicle response curves

3.7 Summary

Based on the level of agreement observed between the force-deformation behavior of the UF/FDOT crushable nose 1100C surrogate vehicle, and the Kia Rio production vehicle, the surrogate vehicle was deemed valid for use in subsequent pendulum impact testing of candidate breakaway hybrid connection designs. All pendulum impact tests of breakaway systems described in the remainder of this report made use of the crushable nose 1100C surrogate vehicle described in this chapter.

CHAPTER 4
FIBER-REINFORCED POLYMER (FRP) POST

4.1 Introduction

In preparation for development of hybrid breakaway connection systems employing fiber-reinforced polymer (FRP) composite components, a review of available FRP systems was conducted. Samples of FRP structural components produced by multiple manufacturers (and employing varying methods of production), were obtained and preliminary laboratory testing was performed to assess suitability for use in roadside sign structures. Based on the results of this preliminary phase of static testing, pultruded structural FRP composite components produced by Creative Pultrusions, Inc. (CPI) were identified as possessing characteristics that offered potential advantage for use within breakaway sign post systems. Specifically, the 'Powertrusion' line of 'power pole' (electrical distribution) products produced by CPI was selected for investigation and adaptation in this study. Powertrusion poles are fiberglass reinforced composite utility poles manufactured using electrical grade E-glass that has a minimum tensile strength of 290 ksi. Features that offer potential advantage—relative to steel—for use in breakaway sign structures, include: reduced weight (mass) density, which leads to reduced vehicle occupant risks and easier system installation; a high strength-to-weight ratio; and lack of issues related to corrosion.

From among the commercially-available products produced regularly by CPI, the octagonal CP076 pole section, with an outside (flat-to-flat) 'diameter' dimension of 8 in., was selected for investigation in this study. The flat faces of the octagonal outside geometry (Figure 4.1) are beneficial in that they permit flat steel components, such fuse plates and hinge plates, to be flush-mounted directly to the faces of the FRP post. Conversely, the approximately-circular inside geometry of the section offered the promise of simple integration with structural steel pipes, as would be required at various locations in a sign structure (e.g., at the base).

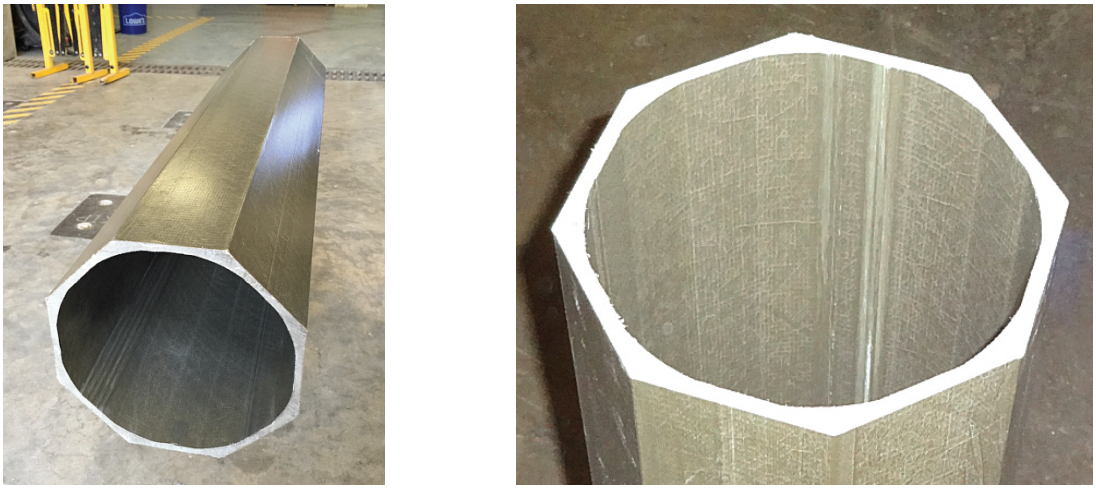

(a) (b)

Figure 4.1 Octagonal CP076 FRP power pole manufactured by Creative Pultrusions: (a) Overview; (b) Detail of cross-sectional shape

4.2 Flexural strength requirement and manufacturer-specified properties

As described earlier in this report, the 'design flexural capacity' of the low-capacity hybrid (i.e. FRP + steel) breakaway system was defined to be 30 kip-ft. When combined with an FRP factor of safety FS = 2.0, as required by Chapter 8 of AASHTO LTS-6, the required ultimate flexural strength of the FRP post was (2.0)(30 kip-ft) = 60 kip-ft. Based on material properties and section properties provided by CPI (Table 4.1), it appeared very likely that the CP076 octagonal post section would possess adequate flexural capacity for the intended sign structure application. Consequently, static capacity testing of the CP076 post section was carried out to experimentally verify that at least 60 kip-ft of ultimate flexural capacity was obtained.

Table 4.1 Properties of CP076 FRP section as specified by Creative Pultrusions, Inc.

Property name	Property value
Ultimate flexural strength	59.6 kip-ft
Modulus of elasticity	4,300 ksi
Moment of inertia	60.87 in^4
Cross-sectional area	7.72 in^2
Weight	6.33 lbf/ft

4.3 Static flexural testing

Static flexural testing of a CP076 post was conducted on August 30, 2013 at the FDOT Structures Research Center in Tallahassee, Florida. A three-point flexure test (Figure 4.2, Figure 4.3) was used to experimentally quantify the ultimate flexural strength and effective modulus of elasticity of the composite CP076 cross-section. The total length of FRP specimen tested was 96 in., however, the effective span length between centerlines of the support points was 76 in. Laboratory equipment used to conduct the test included:

- Enerpac hydraulic actuator with integrated load cell (Figure 4.4a): Load was applied at a rate of 100 lbf/sec. through a spherical load button and receiver plate (Figure 4.4b), and data were recorded at a rate of 10 Hz.
- Five (5) laser displacement sensors (Figure 4.4c) located at the quarter points of the span: Displacement data were collected at a rate of 10 Hz.

At the load application point, beneath the spherical receiver plate (Figure 4.5a), and at both support (reaction) points beneath the post (Figure 4.5b), elastomeric bearing pads were installed to distribute the forces applied to the FRP section, and to minimize stress concentrations. To additionally stabilize the cross-sectional shape, short cylindrical grout plugs (Masterflow 928) were cast inside the FRP post (Figure 4.2, Figure 4.6) at midspan and at the reaction points. The grout plugs served to distribute the applied forces to the entire FRP cross-section so that the ultimate flexural strength of the CP076 post could be determined without being influenced by localized distortion effects.

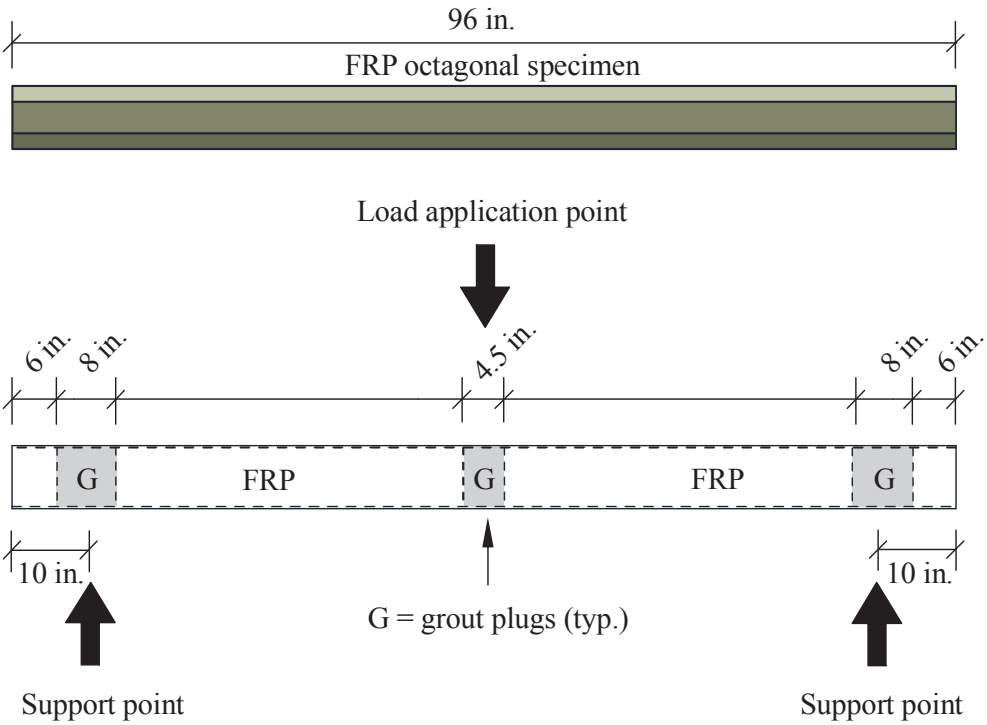

Figure 4.2 Schematic diagram of static three-point flexural test setup

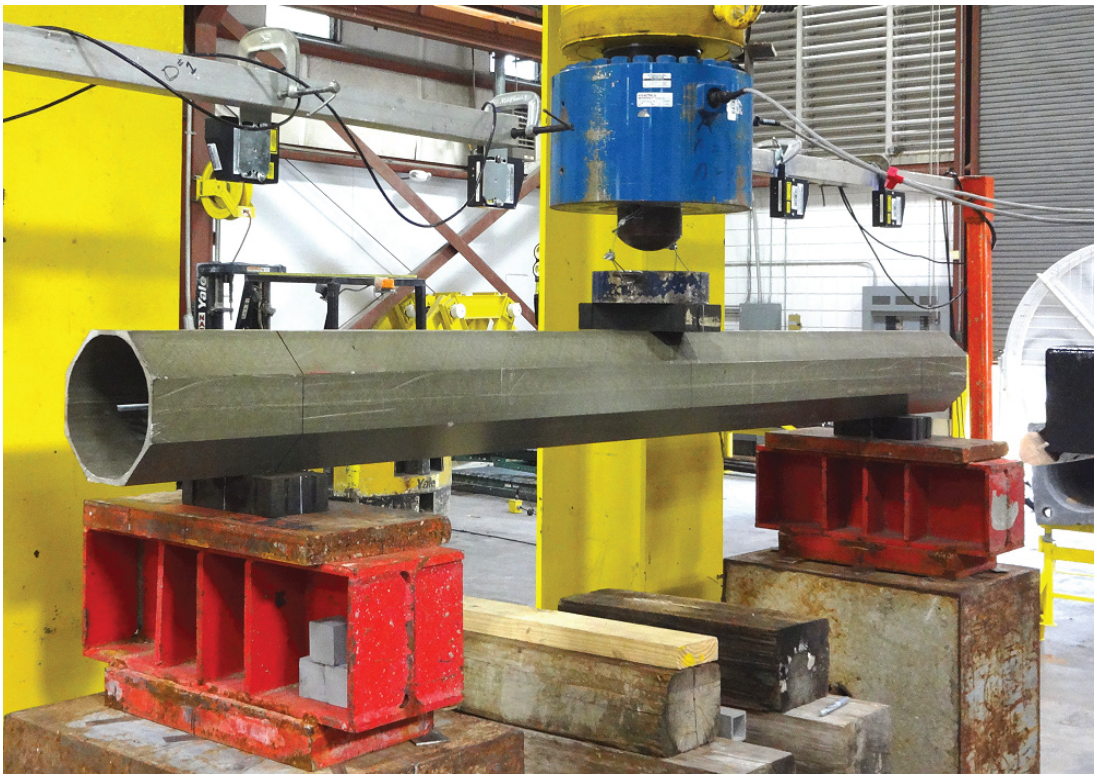

Figure 4.3 Flexural testing of CP076 FRP composite post at FDOT Structures Research Center

(a)

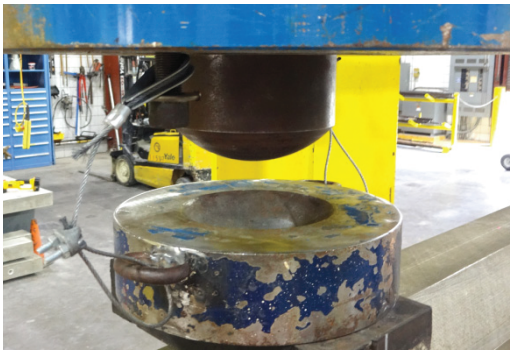

(b)

(c)

Figure 4.4 Details of experimental setup:
(a) Load cell; (b) Spherical load button and receiver plate; (c) Laser displacement sensor

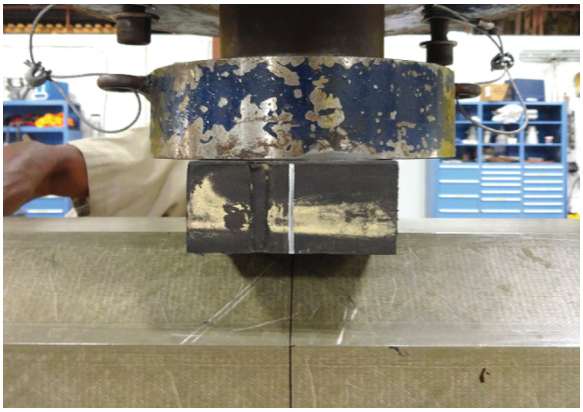

(a)

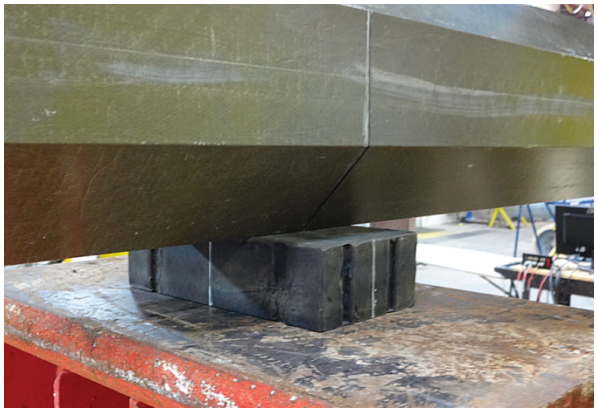

(b)

Figure 4.5 Bearing pads:
(a) At load application point, under receiver plate; (b) At beam support point

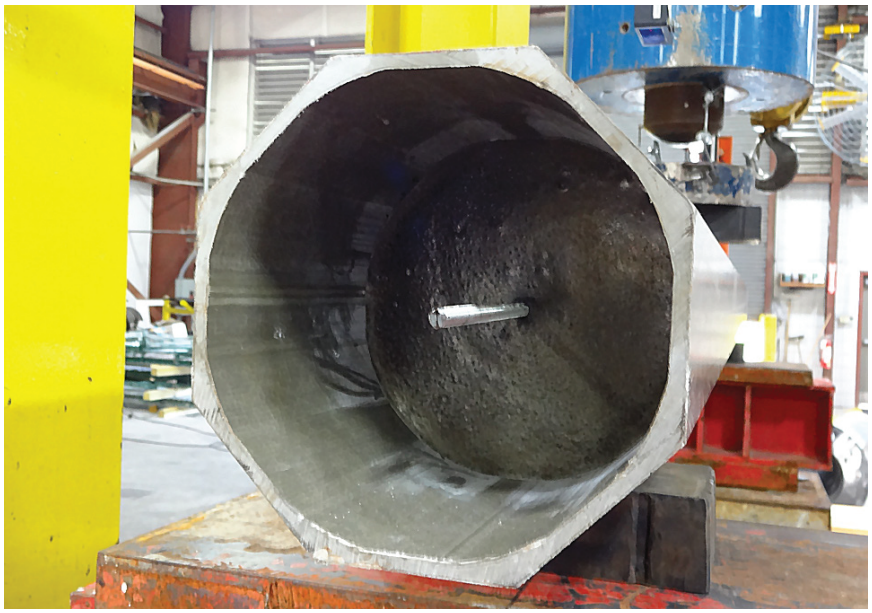

Figure 4.6 Grout plug formed inside FRP post at support point

As load was gradually increased on the post specimen, flexural deformations increased as expected (Figure 4.7a-b) until the ultimate capacity of the section was reached and abrupt failure occurred (Figure 4.7c). Load vs. mid-span deflection data are shown in Figure 4.8 where structural behavior of the post is approximately linear up to the point of abrupt failure (Note that, in order to account for bearing pad compressive deformations during testing, the average of the support point displacements was subtracted from the mid-span displacement to yield the post deflection data show in Figure 4.8). Based on the load at ultimate capacity, and the span length of 76 in., the ultimate flexural capacity of the CP076 FRP section was found to be 71.0 kip-ft (Table 4.2), or 19% larger than the manufacturer-specified value of 59.6 kip-ft (Table 4.1).

To quantify the effective modulus of elasticity of the FRP section—a composite of glass fiber and epoxy resin—least squares curve fitting was used to fit a linear trend line to the load-deflection data in Figure 4.8, up to a maximum load of 40 kip. Using the manufacturer (CPI) specified moment of inertia (Table 4.1) for the CP076 section, and standard beam deflection equations, the effective modulus of elasticity of the FRP composite was found to be 4,443 ksi, or 3% larger than the manufacturer-specified value of 4,300 ksi (Table 4.1).

Shown in Figure 4.9 is a detailed view of the FRP condition at failure, with load still applied to the post. Overall flexural failure appeared to initiate when fibers oriented at ±45° (relative to the longitudinal axis of the post) ruptured, thereby allowing the primary longitudinal fibers to 'part' laterally, and slide upward and around the mid-span grout plug. Due to loss of restraint on the longitudinal fibers, load-carrying capacity was essentially lost. However, once load was released, nearly all downward deflection was recovered as the intact longitudinal fibers slid around the grout plug, and back to the bottom of the section.

Table 4.2 Properties of CP076 FRP section as determined experimentally

Property name	Property value
Ultimate flexural strength	71.0 kip-ft
Modulus of elasticity	4,443 ksi

(a)

(b)

(c)

Figure 4.7 Deformation of CP076 FRP post during flexural testing: (a) Start of test; (b) Near peak load; (c) Failure

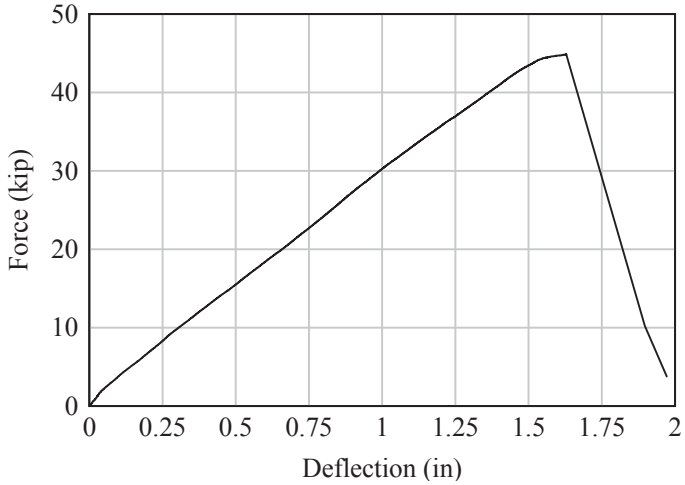

Figure 4.8 Static flexural test results

Figure 4.9 Detailed view of FRP condition after failure

4.4 Summary

Based on the experimentally-determined ultimate flexural capacity of 71 kip-ft noted above, and recalling that the design moment for the low capacity hybrid breakaway connection being designed in this study was defined as 30 kip-ft, the CP076 FRP section exhibited a factor of safety of FS=(71/30)=2.37, which is larger than the FS=2.0 required by AASHTO LTS-6. As such, the CP076 section appeared to possess sufficient capacity for use in development of a low capacity hybrid breakaway base connection for sign structures.

CHAPTER 5
HYBRID BREAKAWAY CONNECTION: SHEAR COLLAR

5.1 Introduction

Two fundamentally different conceptual approaches toward designing a hybrid breakaway connection system around the CP076 FRP post section were investigated in this study. In the first approach—the focus of this chapter—steel components were used to form a 'shear collar' that sheared (i.e., cut or sliced) through fibers in the FRP cross-section during vehicle impact loading. A second, alternative design approach is described in the next chapter.

5.2 Hybrid breakaway connection concept: shear collar

The main objective in developing the shear collar hybrid breakaway connection system was to determine whether the octagonal FRP section could be sheared using metallic cutting edges without generating unacceptable levels of vehicle deceleration or occupant impact velocity. Figure 5.1 illustrates an exploded view of the 'shear collar' connection in order to identify each component. (Note that comprehensive structural drawings for the shear collar connection are provided in Appendix E). In Figure 5.2, a schematic diagram of the fully assembled shear collar system is shown.

Part T1 of the system is the octagonal FRP sign post. Parts T8 and T9 are steel tubes that have machined blades which act as 'scissors', cutting T1 under direct application of shear impact load. The bottom outer portion of the system (T2) keeps the FRP pole restrained, preventing it from moving under impact load. The top outer portion (T3) is impacted by the vehicle, transferring half of the load through shear at the failure (shearing) plane of T1. T5 and T7 prevent the FRP section (T1) from locally buckling during impact loading. In Figure 5.3, photographs during installation and after full assembly are shown.

5.3 Impact testing

Impact testing of the shear collar hybrid connection was conducted on December 3, 2013, at the FDOT Structures Research Center using the 1100C crushable nose surrogate vehicle described earlier in this report and the FDOT pendulum impact test facility.

5.3.1 Test setup

An overall configuration diagram for the impact test conducted on the shear collar system is provided in Figure 5.4. A surrogate vehicle drop height of 12 ft was used to generate the 19-mph, low speed, small car (1100C) impact condition specified by AASHTO MASH. Shown in Figure 5.5 are the surrogate vehicle and the fully-assembled shear collar connection system.

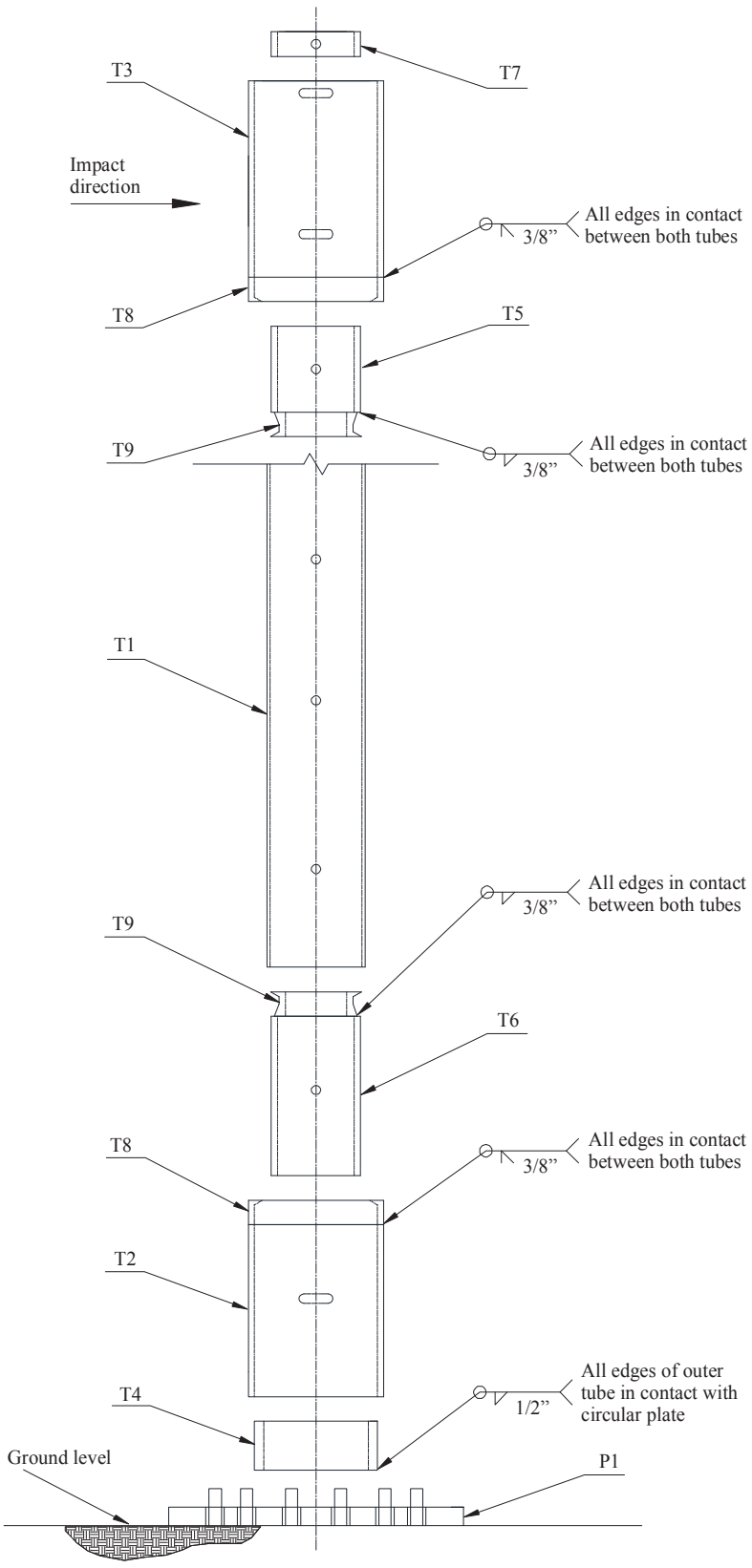

Figure 5.1 Hybrid breakaway system exploded view

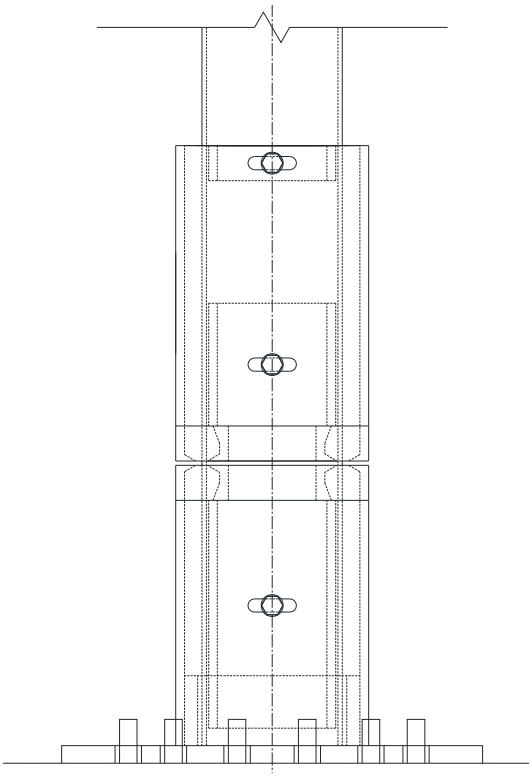

Figure 5.2 Shear collar hybrid breakaway system concept

(a)

(b)

Figure 5.3 Installation of shear collar connection:
(a) Prior to insertion of FRP post; (b) Fully-assembled system

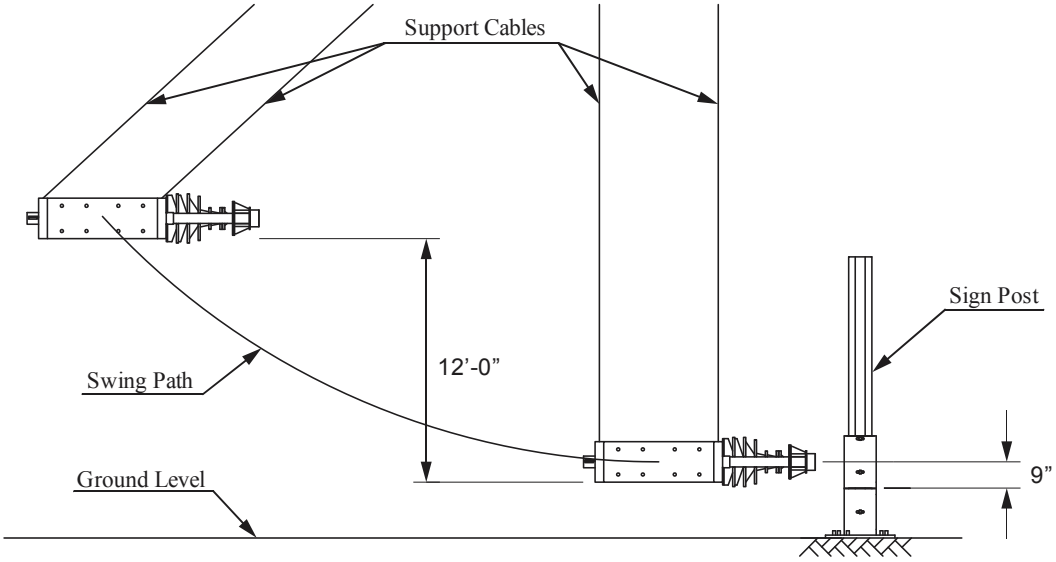

Figure 5.4 Schematic diagram of impact test for shear collar connection concept

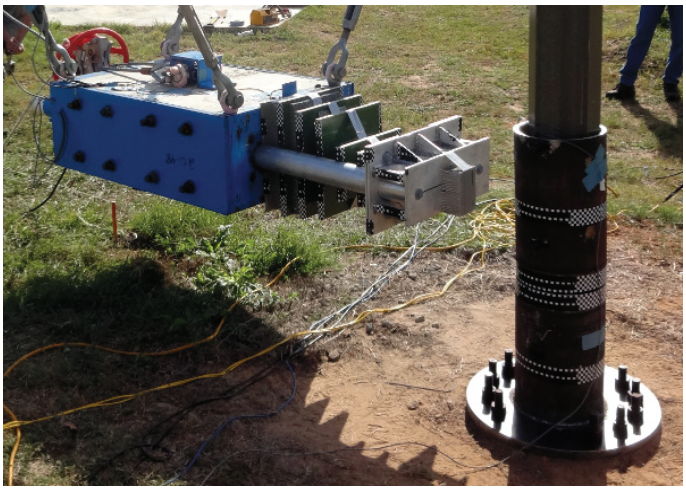

Figure 5.5 Impact test for shear collar connection concept

5.3.2 Test results

Results from the pendulum impact test demonstrated that the machined steel cutting edges in the shear collar connection were able to successfully cut through the FRP pipe cross-section (Figure 5.6), thereby breaking the pipe away from the base. In Figure 5.7, the final conditions of the FRP post and of the steel cutting edges after impact are shown. As is evident in Figure 5.7, the vast majority of longitudinal fibers in the FRP post were 'cleanly' cut (i.e., severed) during impact. Fibers on the 'sides' of the cross-section, however, were not subjected to direct shear by the cutting edges, and were therefore not severed during impact. Instead, rotation of the upper post—relative to the base—loaded these fibers in tension and bending until rupture occurred. Fibers extending from the sides of the cross-section in Figure 5.7 are those that were ruptured in tension/bending rather than cut in shear.

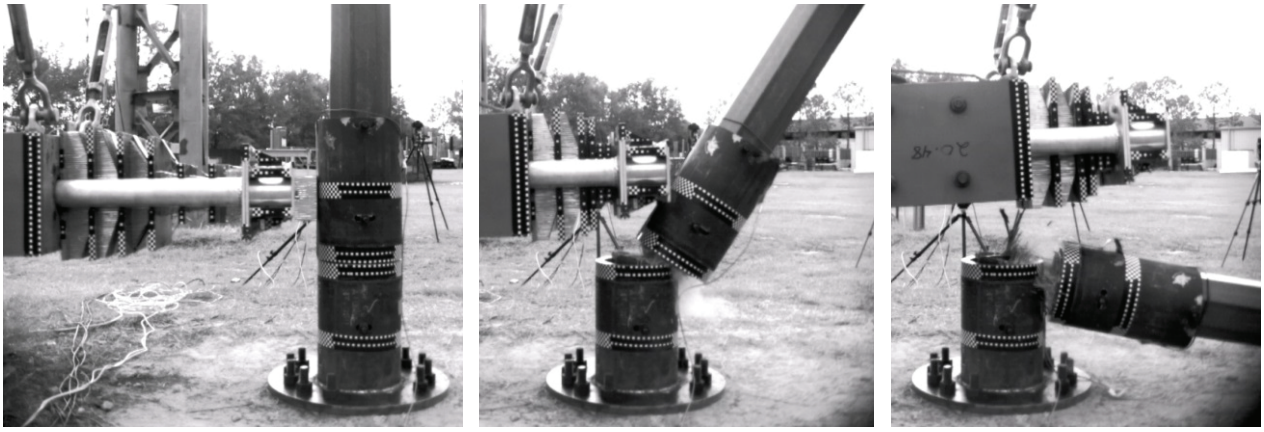

(a) (b) (c)

Figure 5.6 High speed video frames from impact testing of shear collar hybrid connection: (a) Initial contact; (b) Shearing of FRP; (c) Post breaks away from base

(a)

(b)

(c)

Figure 5.7 Condition of FRP post and cutting edges after impact test: (a) Overview with lower portion (stub base) in foreground and sheared upper post in background; (b) Upper portion of post; (c) Lower portion (stub base) of post

During this experiment, the data acquisition system associated with accelerometers mounted to the surrogate vehicle failed to trigger, thus direct measurements of vehicle acceleration were not available. However, two high speed video cameras—recording at 2,000 frames/sec.—triggered properly and recorded the entirety of the impact event. Accordingly, high speed video from the test, pre-test calibration video clips, and motion analysis software (i.e., digital image correlation software—specifically Xcitex ProAnalyst 3-D) were used to process the test results.

By defining t = 0 sec. as the point in time at which the surrogate vehicle made initial contact with the test article (recall Figure 5.6a), and by tracking target-points on the back block using ProAnalyst, a time history of back block displacement was determined (Figure 5.8a). Numerically differentiating this displacement data twice yielded a time history of back block deceleration (Figure 5.8b)—referred to herein more simply as 'acceleration'. An analogous approach was applied to tracking points located on the front block, yielding corresponding front block displacement data (Figure 5.9a) and acceleration data (Figure 5.9b). Individual contributions to overall impact force were then computed by multiplying acceleration data from the back block and front block by the respective masses of these components. Summing both force contributions (i.e., back block + front block) yielded the time history of force (Figure 5.10) that was applied to the shear collar during the impact test.

For purposes of comparing the results from this *breakaway* pole test to the *rigid* pole 1100C validation impact test described earlier in Chapter 3, a force-deformation curve for the shear collar hybrid breakaway connection test was produced. By tracking points on the front block and back block of the surrogate vehicle, a time history of crushable-nose deformation was generated (Figure 5.11a). Subsequently, by time-synchronizing the total force (vs. time) data from Figure 5.10 with the nose deformation (vs. time) data from Figure 5.11a, a surrogate vehicle force-deformation curve (Figure 5.11b) was produced for the shear collar impact test. In Figure 5.12, the *breakaway* test force-deformation data are compared to analogous *rigid* pole test data (previously reported in Figure 3.13). Clearly evident in this figure is the fact that maximum forces acting on the vehicle—and therefore acting on the vehicle *occupants*—during impact were significantly reduced (by ~50%) as a result of introducing the shear collar breakaway connection.

To rigorously evaluate occupant risk, the occupant flail space model defined by AASHTO MASH, and described in detail in Consolazio et al. (2012), was used to quantify occupant impact velocity (OIV) and occupant ride-down acceleration (ORA) for the shear collar impact test. Using back block velocity data, the time at which the theoretical occupant had travelled 2 ft (relative to the vehicle) in the longitudinal direction and impacted the vehicle compartment was determined to be t = 0.17 sec. Computing the relative velocity between the occupant and the vehicle at this same point in time (Figure 5.13) resulted in a computed OIV of 16.7 ft/sec. As documented in Section 2.3.2 of this report, AASHTO MASH limits OIV to no greater than 16 ft/sec, with values less than 10 ft/sec being preferred. Consequently, the FRP shear collar connection tested in this study nearly met the AASHTO MASH limit, exceeding it by ~4%.

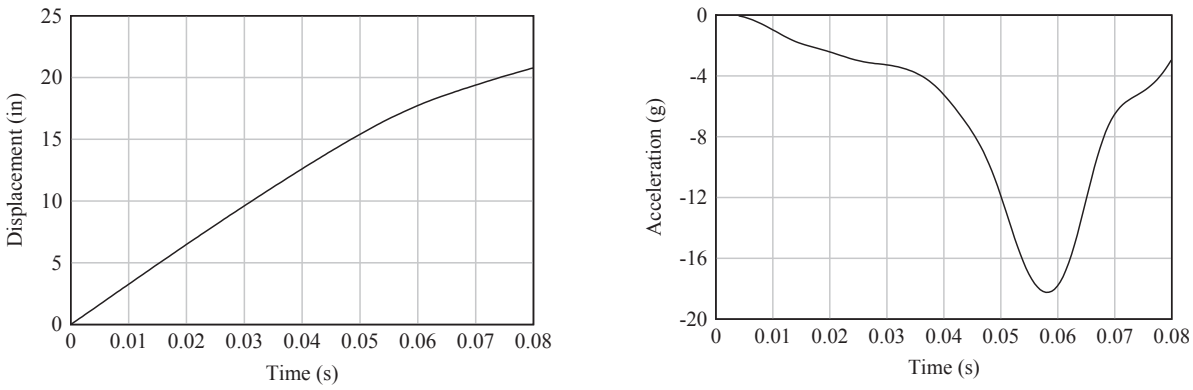

Figure 5.8 Back block data:
(a) Displacement; (b) Acceleration

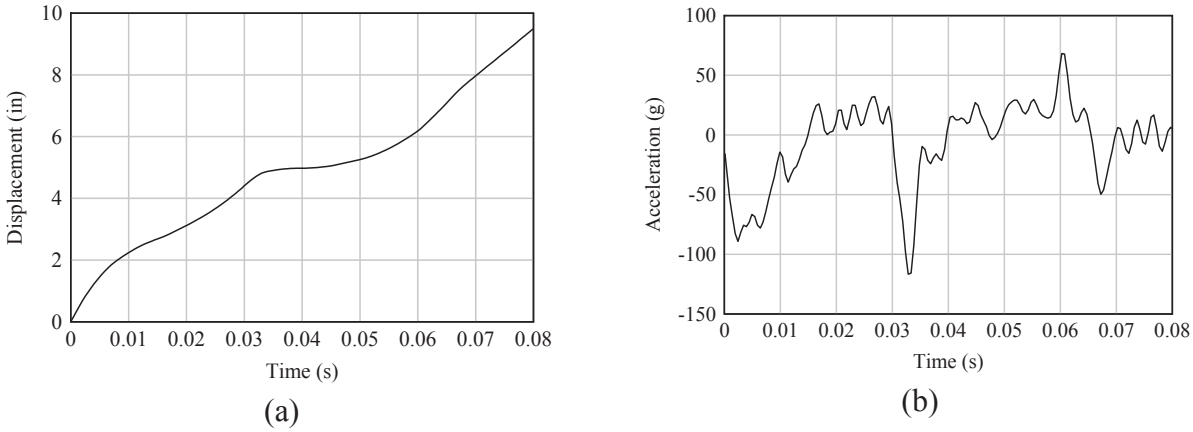

Figure 5.9 Front block data:
(a) Displacement; (b) Acceleration

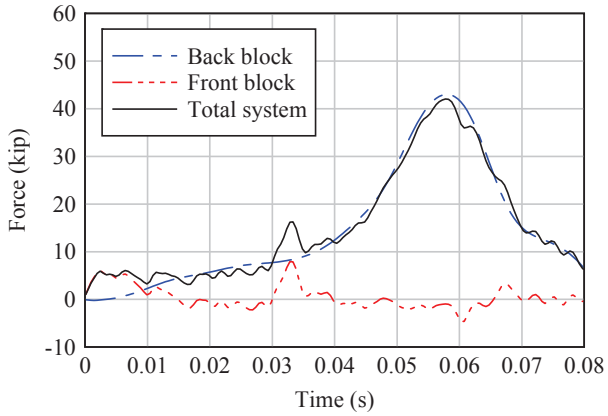

Figure 5.10 Contributing impact forces and total impact force

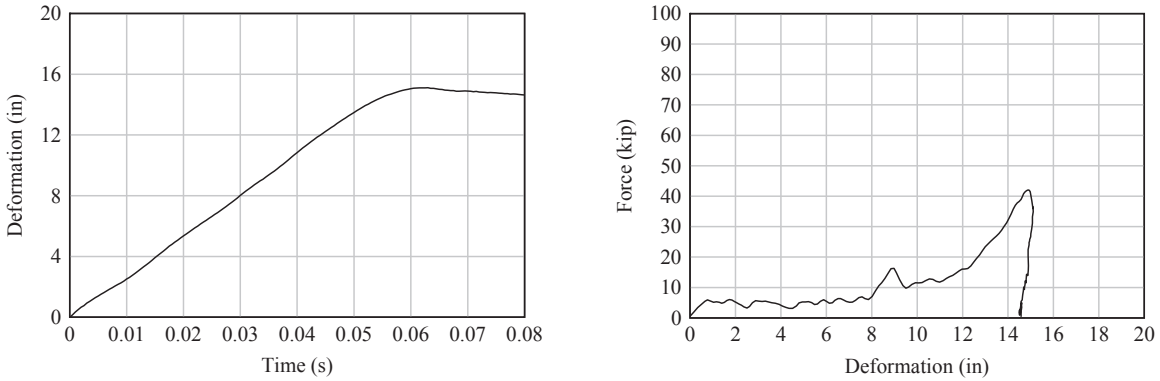

Figure 5.11 Crushable nose data from shear collar impact test:
(a) Nose deformation vs. time; (b) Impact force vs. deformation

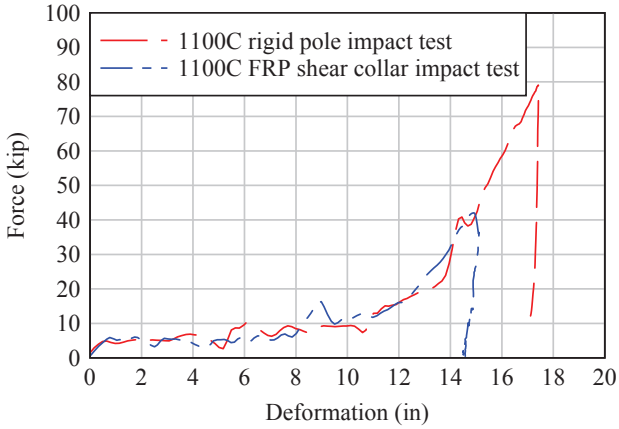

Figure 5.12 Comparison of vehicle force-deformation data from
breakaway shear collar test and rigid pole test

AASHTO MASH also limits the maximum occupant ride-down acceleration (ORA) to 20.49 g, but sets the preferred limit at 15 g. ORA is defined as the maximum vehicle acceleration (or 'deceleration') *after* the occupant has impacted the vehicle compartment (i.e., t = 0.174 sec for this test). Examining the vehicle acceleration data in Figure 5.14 after the time of occupant impact, the maximum acceleration levels are found to be negligible (~0.9 g) in comparison to the AASHTO preferred ORA limit of 15 g.

5.4 Summary

A summary of key results from pendulum impact testing of the FRP shear collar connection is provided in Table 5.1. To reduce the FRP shear collar OIV below the AASHTO MASH limit, a modified shear collar design was developed and subjected to impact testing and static flexural testing. To preclude the need for tensile/bending rupture of longitudinal fibers in

the FRP post (recall Figure 5.7a), the modified design introduced triangular cutouts in the sidewalls of the FRP post (at the shearing plane). Impact testing of the modified system yielded a reduced OIV of 16 ft/sec (permissible per AASHTO MASH), however, separate issues regarding the shear collar design were identified. In particular, it was noted that while the machined cutting blades of the breakaway connection performed satisfactorily under impact testing, their use could potentially lead to undesirably-high machining (fabrication) costs, and might also be susceptible to corrosion-induced dulling, which could adversely affect system performance. Consequently, an alternative hybrid 'FRP + steel' approach was investigated, as described in the next chapter.

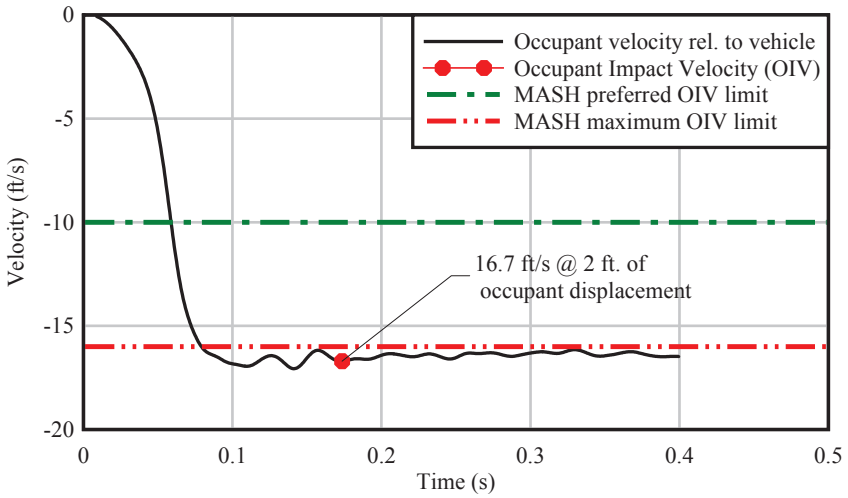

Figure 5.13 Occupant impact velocity (OIV) from head-on (0 deg.) 19 mph impact test

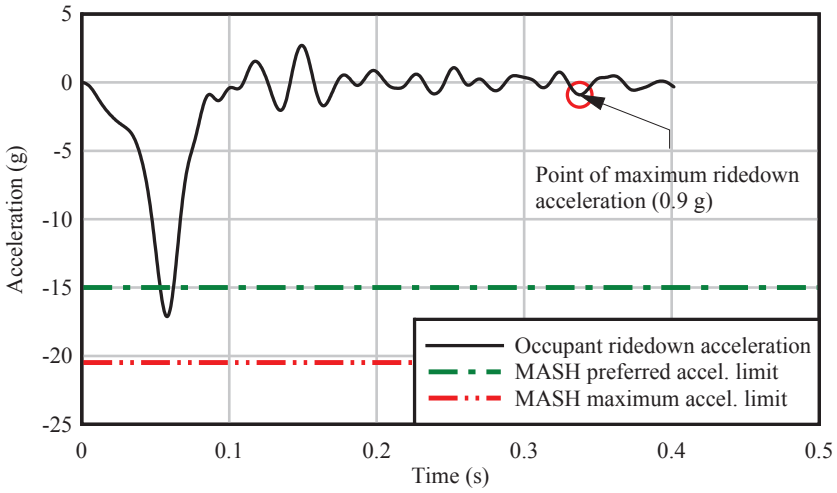

Figure 5.14 Occupant ride-down acceleration (ORA) from head-on (0 deg.) 19 mph impact test

Table 5.1 FRP octagonal section experimental impact shear test results

Risk parameter	Value
Occupant impact velocity (OIV)	16.7 ft/sec
Occupant ride-down acceleration	0.9 g
Maximum impact force	42.0 kip

CHAPTER 6
HYBRID BREAKAWAY CONNECTION: MOMENT COLLAR

6.1 Introduction

To alleviate potential issues (such as blade dulling) that could degrade the ability of steel components to reliably slice through an FRP sign post, an alternative design approach was investigated wherein the FRP post was joined to a steel breakaway connection. In this alternative hybrid design concept, key aspects of breakaway performance were made dependent on steel components failing in a predictable manner (e.g., through tensile failure of bolts) rather than on the ability of steel components to cut through FRP.

6.2 Hybrid breakaway connection concept: moment collar

In a parallel study (BDV31-977-24, Consolazio and Innocent 2016), a breakaway connection system composed entirely of steel components, and intended for use with steel wide-flange sign posts, was developed. Three versions of the connection—referred to as a 'moment collar' connection—were developed: high-capacity, medium-capacity, and low-capacity (as summarized earlier in Section 1.1.1). Since the design flexural capacity (30 kip-ft) of the hybrid connection developed in the present study matched that of the 'low capacity' moment collar connection (recall Figure 1.6) developed in the parallel study BDV31-977-24, this latter system was adapted for use with FRP posts.

6.2.1 Adaptation of all-steel connection

In transforming the 'all-steel' low-capacity breakaway system of BDV31-977-24 (Figure 6.1a) into a hybrid 'FRP + steel' system (Figure 6.1b), the steel wide-flange sign post of the former was replaced with a circular HSS (hollow structural shape) steel stem that was inserted into the end of the FRP sign post. The vast majority of components in the 'all steel' moment collar system (Figure 6.1a) were conceptually preserved in the hybrid adaption (Figure 6.1b), but were dimensionally modified (e.g. plate thickness, etc.) as necessary to produce the required flexural capacity. In Figure 6.2, all components of the hybrid moment collar connection are identified.

When wind load is applied to a sign panel, flexural moment is developed in each supporting FRP sign post. Moment is transmitted from the FRP post to the steel connection through a 20 in. tall (= 2.5 x 8 in. [the FRP 'diameter']) vertical overlap between the FRP post and steel HSS stem; the latter of which is welded to the upper flange plate. Moment is transmitted from the upper flange plate to the lower flange plate partially through the action of the upper and lower binding plates in each collar half (Figure 6.2). On the 'tension side' of the connection, the upper and lower binding plates transmit vertical force from one flange plate to the other. On the 'compression side', force is transmitted through direct contact between the flange plates. The ultimate flexural capacity of the connection is related to the thicknesses (and strengths) of the flange plates, binding plates, and primary plates in the connection, as well as the HSS stem.

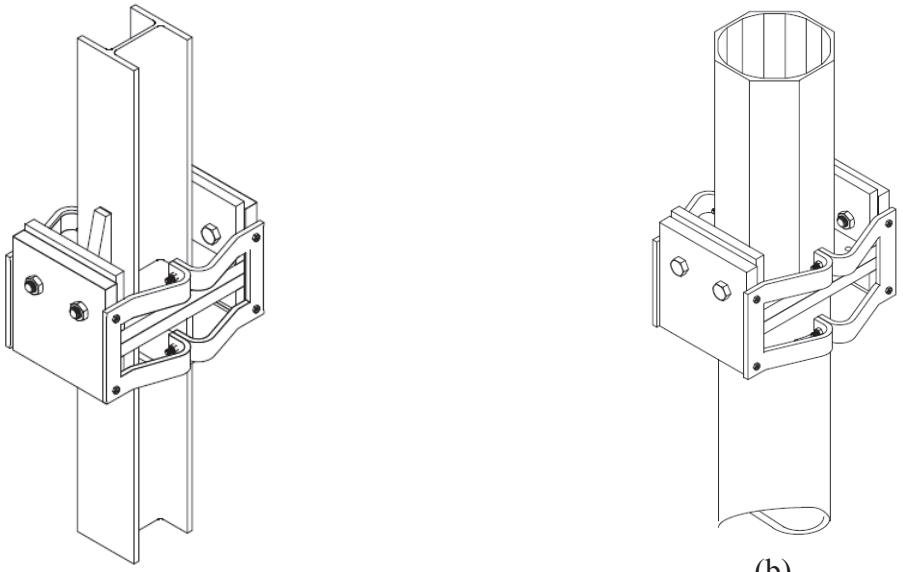

Figure 6.1 Adaptation of moment collar connection:
(a) All-steel system with steel wide-flange post;
(b) Hybrid system with steel HSS stem and FRP post

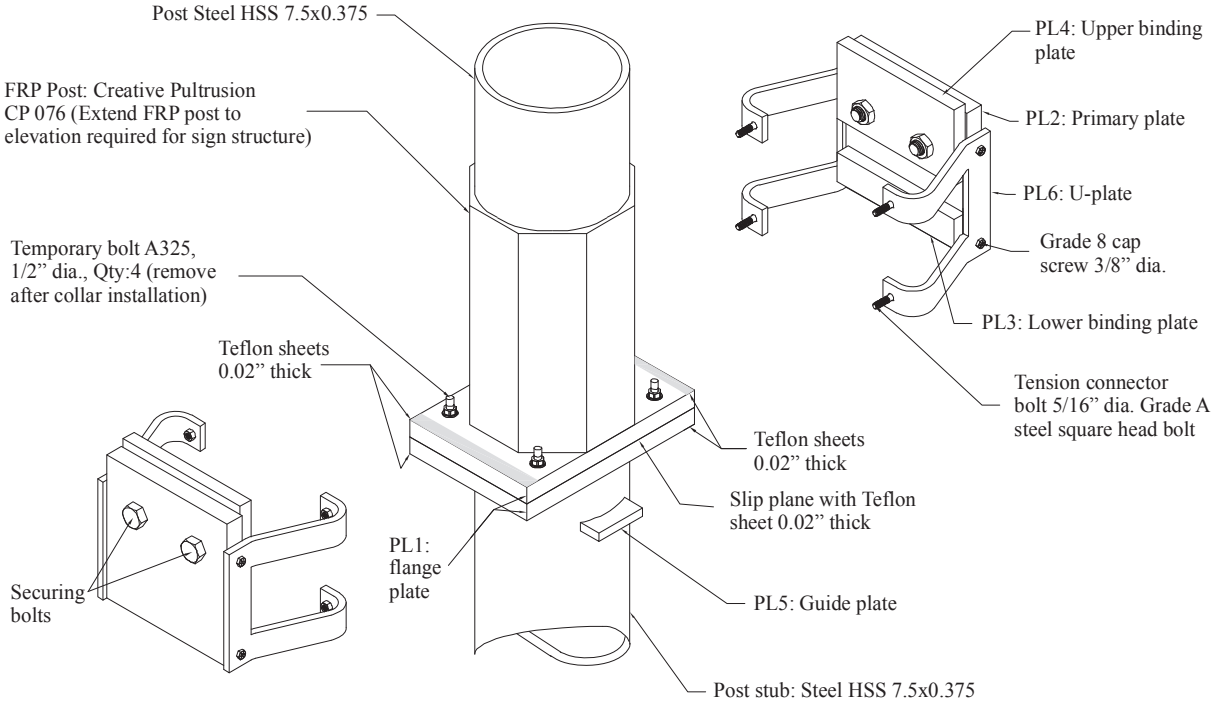

Figure 6.2 Exploded view of moment collar connection adapted for use with an FRP post

Under the action of vehicle impact load, force is applied to the portion of the connection located vertically above the slipping plane. When impact load exceeds the tensile capacity of the four tensile 'connector bolts' (Figure 6.2), the connection breaks (i.e. the two halves of the collar separate), allowing components above the slipping plane (the FRP post and steel HSS stem) to separate from the base (recall Figure 1.2).

6.2.2 Quasi-static FEA pushover simulation

To quantify the ultimate flexural capacity of the connection under equivalent-static wind loading conditions, finite element models representing each 'candidate' (i.e., trial) design of the moment collar connection, and attached segments of HSS stem and FRP sign post, were subjected to quasi-static 'pushover' analyses. In each analysis, a stiff horizontal spring was attached to the sign post (Figure 6.3a) at the elevation of the center of wind pressure. The node at the end of the spring opposite the sign post was given a 'slow' (quasi-static) time-varying horizontal displacement. As the node displaced, axial force generated in the spring acted as an equivalent wind load on the sign post, thus generating flexural moment in the breakaway moment collar connection at the base of the post. By using this type of displacement control (prescribed displacement), rather than load control (prescribed load), it was possible to deform each trial connection-and-post model to the point of structural collapse (plastic pushover), permitting a clear evaluation of the ultimate flexural capacity of the base connection. Interpretation of pushover analysis results was accomplished by computing and plotting moment-rotation (Figure 6.3b) response curves for each candidate breakaway moment collar connection.

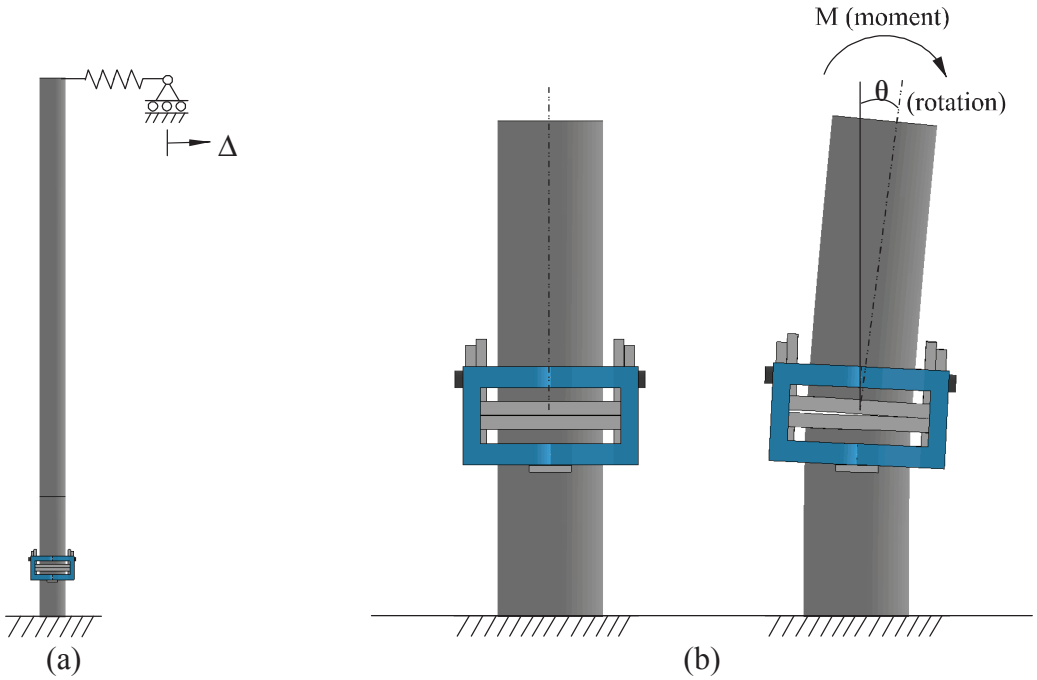

Figure 6.3 Finite element pushover analysis:
(a) Overall model showing location of prescribed displacement; (b) Relationship between moment and section rotation

When combined with a factor of safety FS = 1.5, as required by Chapter 12 of AASHTO LTS-6 for breakaway connections, the required ultimate flexural strength of the moment collar connection was (1.5)(30 kip-ft) = 45 kip-ft. Results from a quasi-static pushover analysis (Figure 6.4) of the finalized hybrid moment collar indicated that yielding first occurred on the tension-side of the HSS tube, near the junction with the upper flange plate. Ultimate capacity was eventually controlled by formation of a plastic hinge in the HSS stem.

In Figure 6.5, moment-rotation data—determined per Figure 6.3b —from the pushover analysis are compared to the design moment (30 kip-ft) and to the ultimate moment required by AASHTO LTS-6 (45 kip-ft). Per finite element pushover simulation, the moment collar connection and HSS stem possessed an ultimate flexural strength that exceeded the AASHTO required value by a considerable margin. It must be noted that selection of the HSS stem diameter was primarily dictated by ensuring a close dimensional match between the outer diameter of the HSS and the inner diameter of the FRP composite CP076 post section. While reducing the diameter of the HSS would have been feasible from a strength perspective, doing so would have created an unacceptably large diameter mismatch—and gap—between the HSS stem and the FRP post. (Detailed drawings of the finalized hybrid moment collar connection components are provided in Appendix F.)

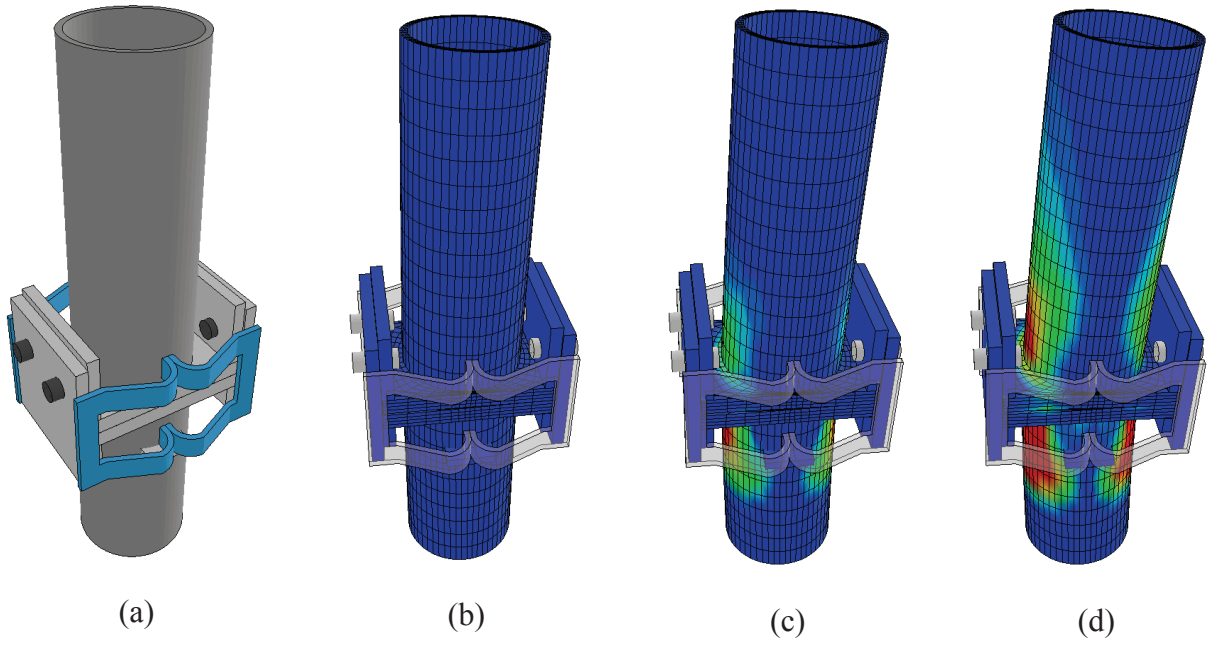

Figure 6.4 Plastic strains from pushover analysis of moment collar with HSS stem: (a) Unstressed model; (b) Initial loading; (c) Yielding of HSS stem; (d) Maximum flexural capacity (Legend: blue = $\varepsilon_P = 0$ in/in; red = $\varepsilon_P = (10)\varepsilon_Y$)

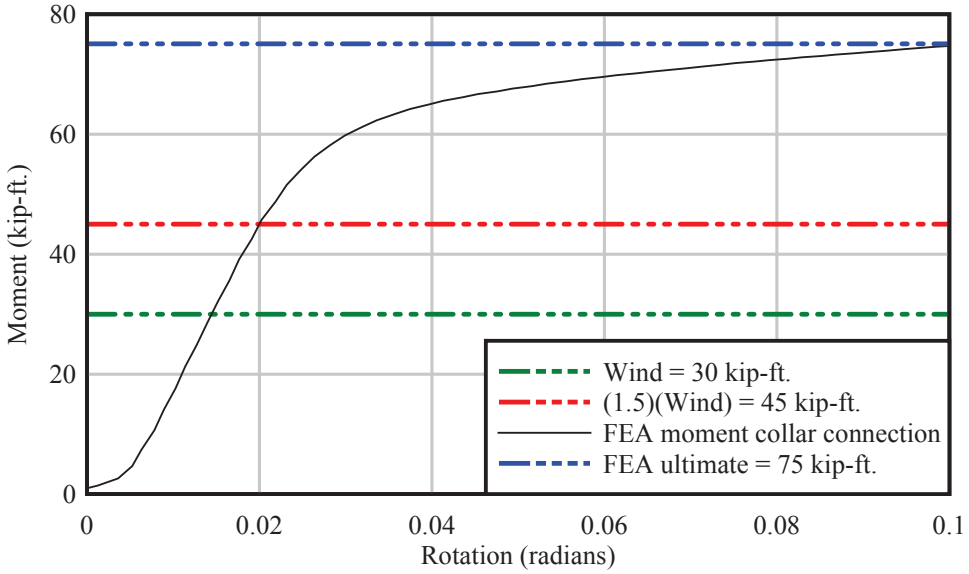

Figure 6.5 Pushover analysis results

6.3 Impact testing

Impact tests of the moment collar hybrid connection were conducted at the FDOT Structures Research Center using the FDOT pendulum impact test facility (Figure 6.6). To be consistent with the requirements of AASHTO MASH, impact tests were conducted using the 1100C crushable nose surrogate vehicle described earlier in this report, an impact speed of 19 mph [produced by using a drop height of 12 ft (Figure 6.7)], and impact angles of 0 deg. and 25 deg. Instrumentation used during each impact test included:

- Uniaxial accelerometers (50 g, quantity =2) on the back block of the surrogate vehicle
- Uniaxial accelerometer (250 g, quantity =1) on the impact head of the surrogate vehicle
- High speed video cameras (zoomed view, and wide angle view, quantity = 2)
- Emitter/receiver pairs of infrared optical break beam sensors (quantity = 2)
- A tape switch affixed to the impact face of the test article (FRP post)

Both high speed video cameras recorded data at a rate of 2,000 frames/sec. All remaining sensors (accelerometers, etc.) were sampled and recorded at a frequency of 10 kHz.

6.3.1 Head-on (0 degree) impact test

On January 20, 2016, a single-post integrated test article—consisting of a stub base, the moment collar breakaway connection (Figure 6.2), steel HSS stem, FRP composite CP076 lower-segment post (recall Figure 1.1a), fuse/hinge plates, and FRP composite CP076 upper-segment post (recall Figure 1.1a)—was installed (Figure 6.8) and subjected to a head-on (0 deg.) impact from the UF/FDOT 1100C surrogate vehicle (Figure 6.9). In accordance with the dimensions of the Kia Rio production vehicle from which the surrogate vehicle was developed, the impact elevation (mid-height of the impact head) on the hybrid lower-segment post was 18 in. above the theoretical ground plane (i.e., 14 in. above the slip plane in the breakaway connection, leaving a 4 in. permanent stub, as permitted by AASHTO MASH).

Figure 6.6 Impact pendulum at FDOT Structures Research Center (Tallahassee, FL)

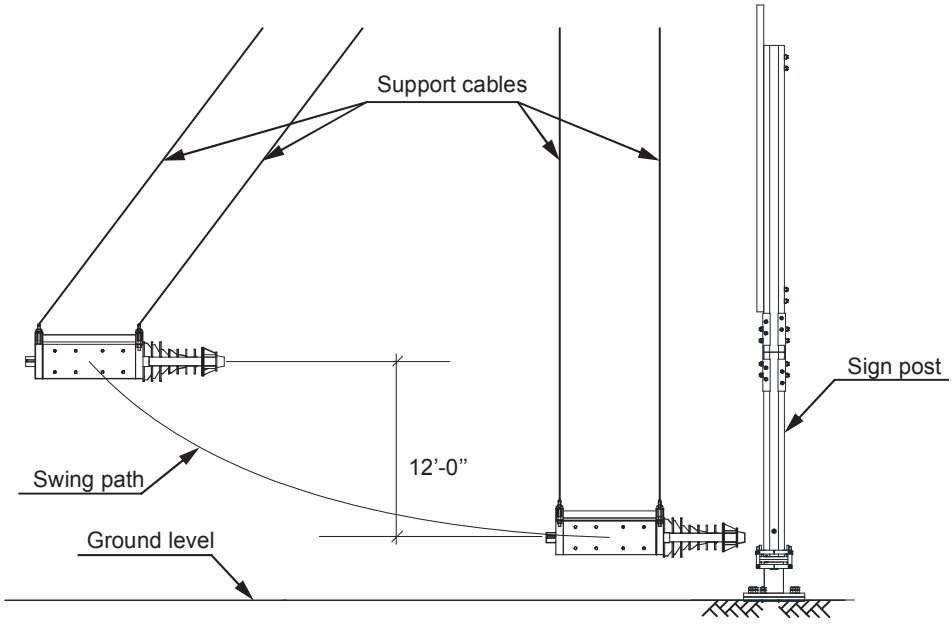

Figure 6.7 Schematic diagram of impact test

(a)

(b)

(c)

(d)

Figure 6.8 Installation of test article for head-on (0 deg.) impact test:
(a) Post and stem mounted to stub with temporary fit-up bolts; (b) Collar halves ready for installation; (c) Binding plate compression tools attached; (d) Collar installed

In Figure 6.10, frames from high speed video of the head-on impact test confirm that the two halves of the moment collar broke apart cleanly—as intended—after the tension bolts holding them together reached their failure loads. On the upstream (impact) side, one collar-half remained with the stub and dropped to the ground. On the downstream (non-impact) side, the other collar-half cleared the stub without snagging and traveled with the lower-post. As noted in Section 2.3.2, MASH states that detached (breakaway) elements—e.g., the downstream collar half—are not permitted to penetrate the vehicle occupant compartment or present an undue hazard to other traffic, pedestrians or nearby personnel. Since the trajectory of the downstream collar half is *away* from the impacting vehicle, the risk of vehicle compartment penetration is negligible. Furthermore, the downstream collar travels in the *same direction* that the vehicle travels after passing beneath the sign structure (recall Figure 1.2). In a pendulum impact test, forward motion of the surrogate vehicle is halted by gravitational resistance (caused by the

upward arc of the swing path). However, in a roadside environment, the vehicle will—by design—continue traveling past the sign structure, thus essentially following the path of downstream collar half. While a finite level of risk is acknowledged to be associated with the motions of both the vehicle and of the downstream collar half, 'undue hazards' are not deemed to be introduced by such motions.

(a)

(b)

(c)

Figure 6.9 Head-on (0 deg.) impact test:
(a) Fully-installed test article; (b) Elevation view; (c) Isometric view

In Figure 6.11, frames from wide angle high speed video again show clean separation of the post from the stub. In contrast to a 'full' multi-post and sign panel system (recall Figure 1.3), where the stiffness of non-impacted posts restrains rotation of the sign panel and, in turn, rotation of the upper-segment of the impacted post, no such stiffness was present in the single-post test setup. Consequently, there was insufficient resistance to break the fuse plate at mid-height, and the entire post (lower and upper segments) rotated as a single entity (Figure 6.11).

Acceleration data from two 50g accelerometers mounted on the 1100C surrogate vehicle back block were averaged together and time-integrated (using trapezoidal integration) to compute the occupant impact velocity (OIV), which was found to be 8.9 ft/sec (Figure 6.12). For comparison, AASHTO MASH specifies a preferred OIV limit of 10 ft/sec and a maximum permissible limit of 16 ft/sec. AASHTO MASH also limits the maximum occupant ride-down acceleration (ORA) to 20.49 g, but sets the preferred limit at 15 g. Examining the acceleration data in Figure 6.13 after the time of occupant impact (i.e., $t = 0.27$ sec for this test), the maximum occupant acceleration levels are found to be negligible in comparison to the AASHTO preferred ORA limit of 15 g.

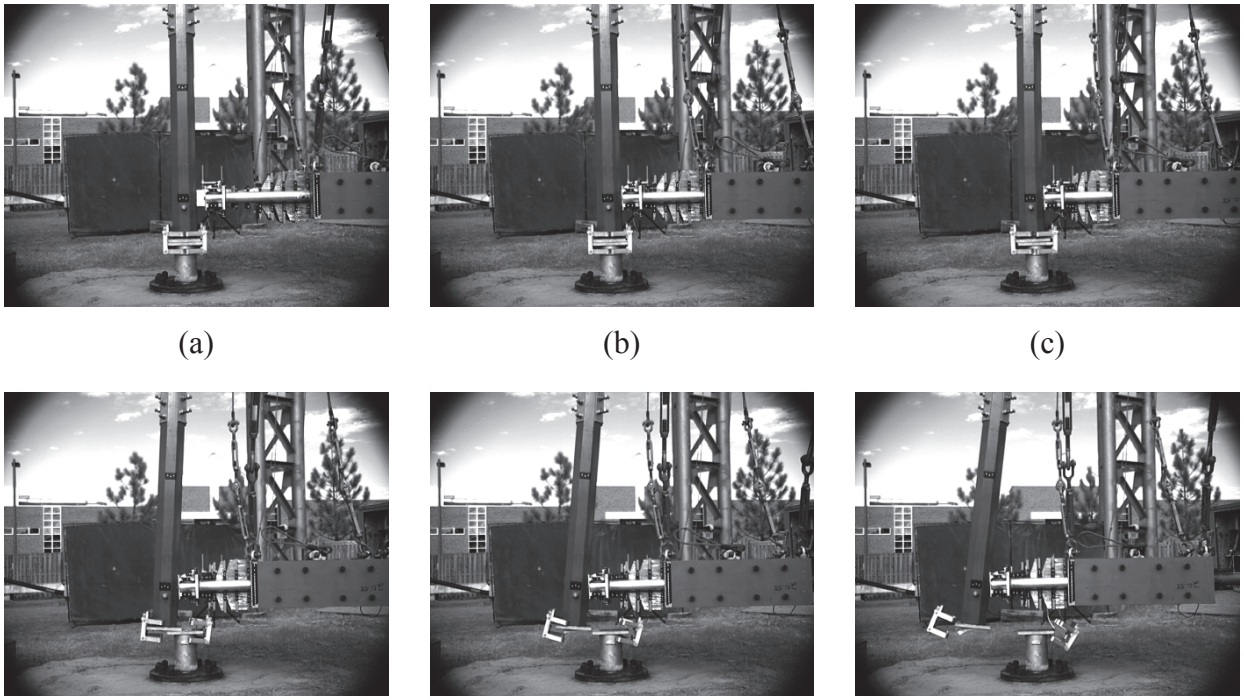

(a) (b) (c)

(d) (e) (f)

Figure 6.10 High speed video frames from head-on (0 deg.) 19-mph impact test

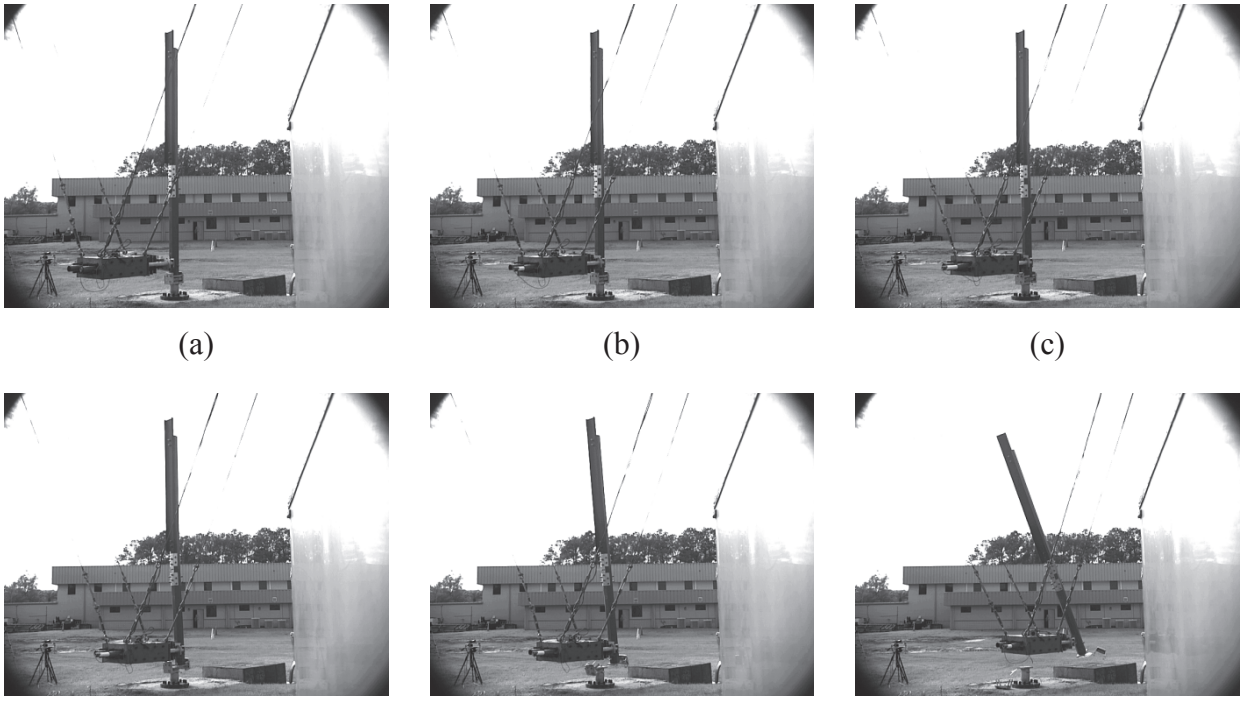

(a) (b) (c)

(d) (e) (f)

Figure 6.11 Wide angle high speed video frames from head-on (0 deg.) 19-mph impact test

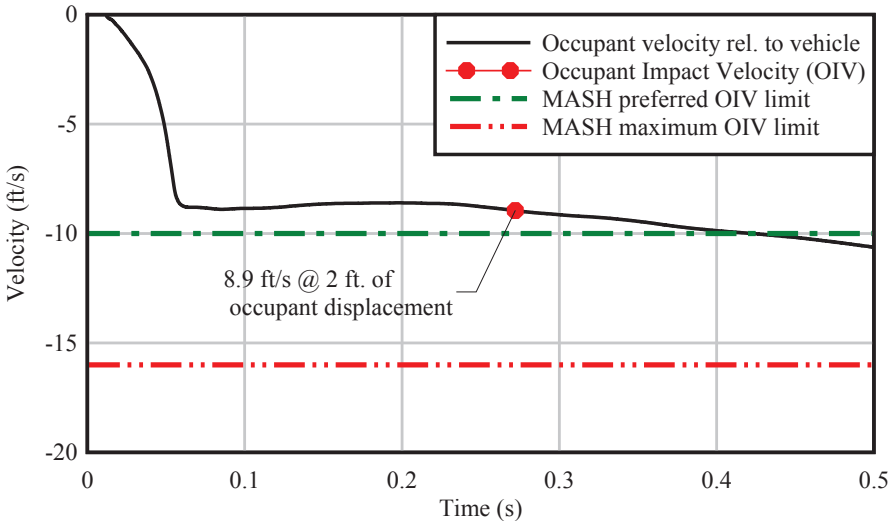

Figure 6.12 Occupant impact velocity (OIV) from head-on (0 deg.) 19-mph impact test

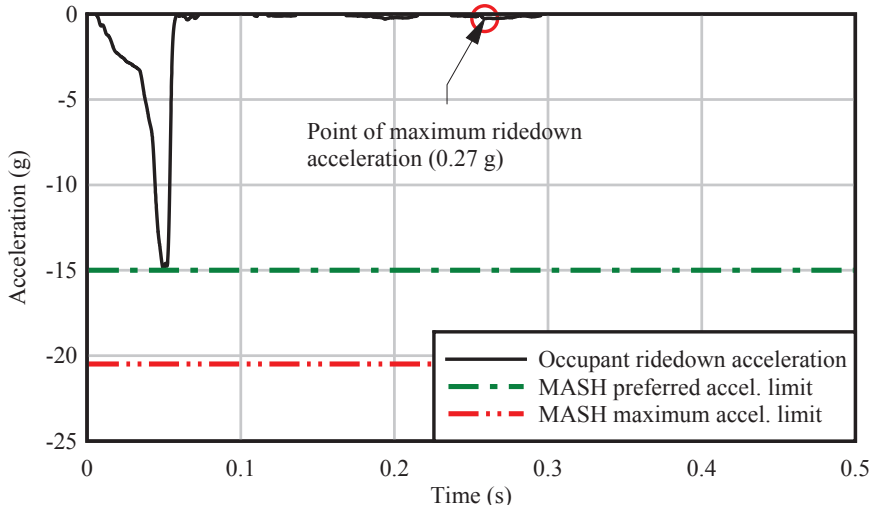

Figure 6.13 Occupant ride-down acceleration (ORA) from head-on (0 deg.) 19-mph impact test

6.3.2 Oblique (25 degree) impact test

On February 5, 2016, an oblique angle (25 deg.) impact test was performed (Figure 6.14) to assess the potential for breakaway component snagging and abrupt vehicle deceleration. In Figure 6.15, frames from high speed video of the oblique impact test confirm that no significant snagging occurred. In Figure 6.16, frames from wide angle high speed video again show clean separation of the post from the base. Similar to the head-on (0 deg.) impact, in the oblique (25 deg.) impact test, there was insufficient upper-segment post resistance to break the fuse plate at mid-height, thus the entire post (lower and upper segments) rotated as a single entity.

(a)

(b)

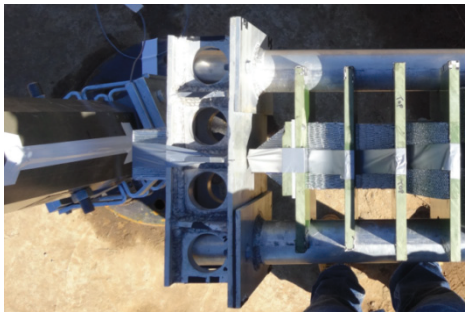

(c)

Figure 6.14 Oblique (25 deg.) impact test:
(a) Fully-installed test article; (b) Isometric view; (c) Overhead view at impact point

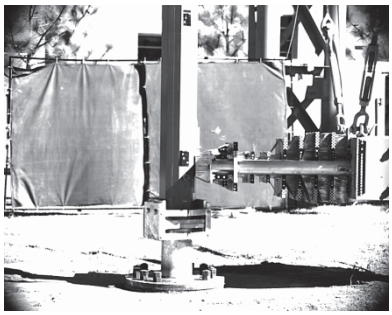

(a)

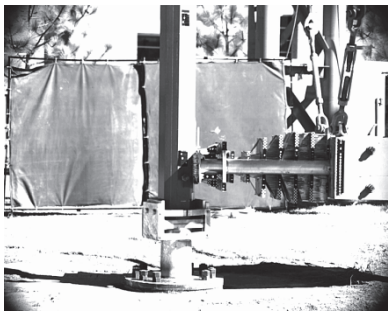

(b)

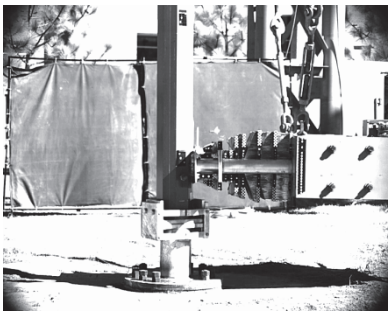

(c)

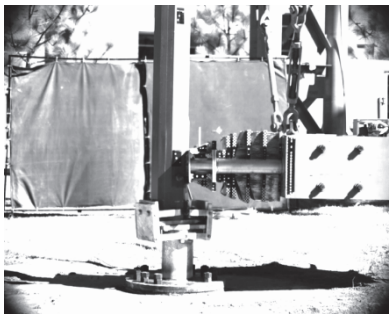

(d)

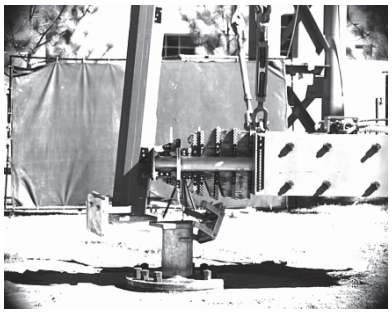

(e)

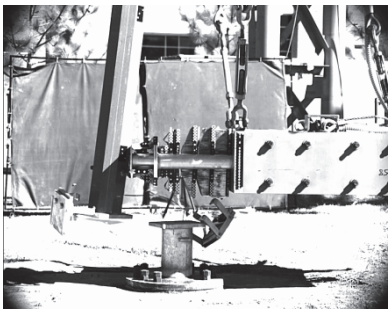

(f)

Figure 6.15 High speed video frames from oblique (25 deg.) 19-mph impact test

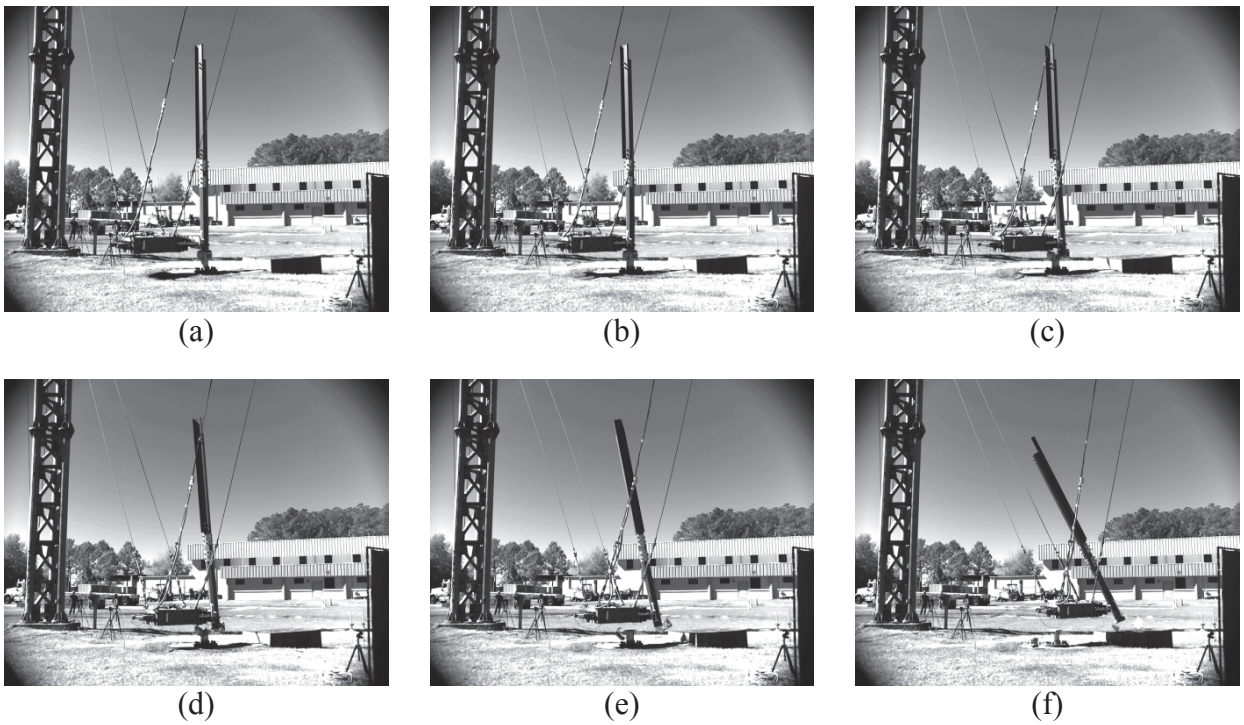

Figure 6.16 Wide angle high speed video frames from oblique (25 deg.) 19-mph impact test

Acceleration data from two 50g accelerometers mounted on the 1100C surrogate vehicle back block were averaged together and time-integrated (using trapezoidal integration) to compute the occupant impact velocity (OIV), which was found to be 8.8 ft/sec (Figure 6.17). For comparison, AASHTO MASH specifies a preferred OIV limit of 10 ft/sec and a maximum permissible limit of 16 ft/sec.

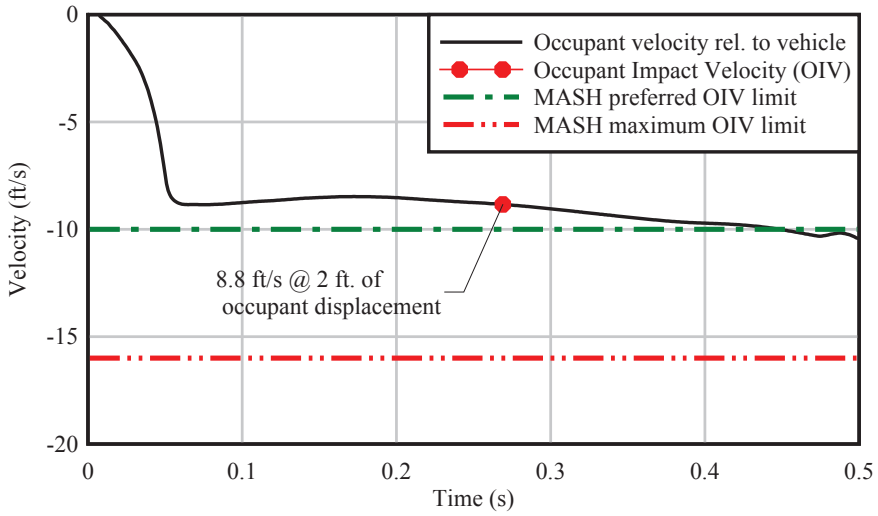

Figure 6.17 Occupant impact velocity (OIV) from oblique (25 deg.) 19-mph impact test

Maximum occupant ride-down acceleration (ORA), occurring after the time of occupant impact (i.e., t = 0.27 sec for this test), was found to be negligible in comparison to the AASHTO MASH preferred ORA limit of 15 g, or the maximum limit of 20.49g. Hence the experimental OIV and ORA were both well within the permissible limits established by AASHTO MASH.

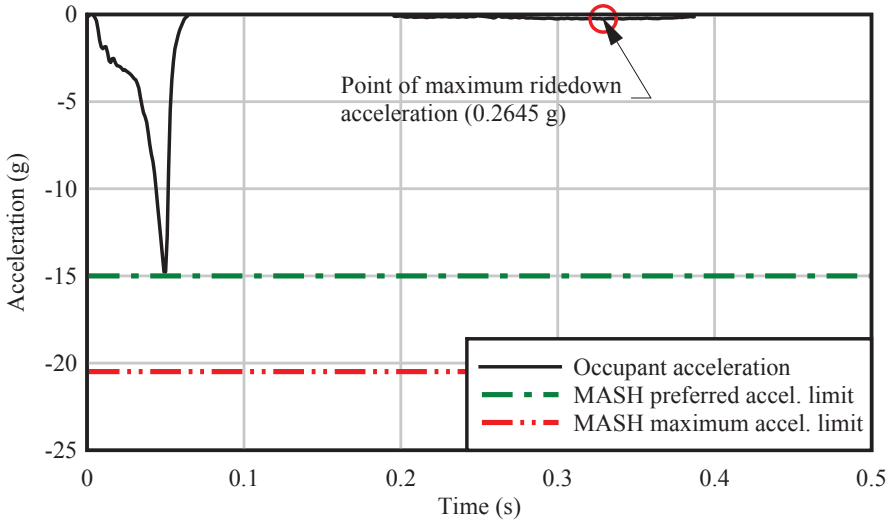

Figure 6.18 Occupant ride-down acceleration (ORA) from oblique (25 deg.) 19-mph impact test

6.3.3 Fuse plate testing

Since pendulum impact testing of the single-post test articles did not produce fuse plate rupture—as would occur in a multi-post sign structure (recall Figure 1.3)—a separate test setup was developed to collect data relating to fuse plate elongation and failure. Using results from a finite element simulation of an 1100C vehicle impact against a three-post sign structure, data relating to the tensile loading rate of the fuse plate were quantified. A special-purpose single-post pendulum impact experiment (Figure 6.19a) was then designed to load a fuse plate at a rate similar to that obtained from the three-post impact simulation. Achieving the target fuse plate load rate required designing a revised set of aluminum honeycomb cartridges, and computing a revised impact speed (and corresponding impact block drop height). Tracking points were imprinted on the fuse plate in a grid pattern (Figure 6.19a) so that high speed video recorded during the test could be processed to determine fuse plate elongations and average strains.

On May 18, 2016, an impact test was conducted on the special-purpose fuse plate test setup. Unfortunately, during the test, failure occurred not in the fuse plate, but instead at the base of the FRP post (Figure 6.19c). Based on the magnitude of impact force that was generated during the experiment, and the vertical moment arm, the flexural moment at the base was determined to be well below the known ultimate flexural capacity of the FRP post (discussed in Chapter 4). The FRP failure mode appeared to be the result of inadequate circumferential fiber strength at the base of the post. This result was consistent with results from *static* flexural tests which were conducted in the same general timeframe (and which are discussed in the sections that follow).

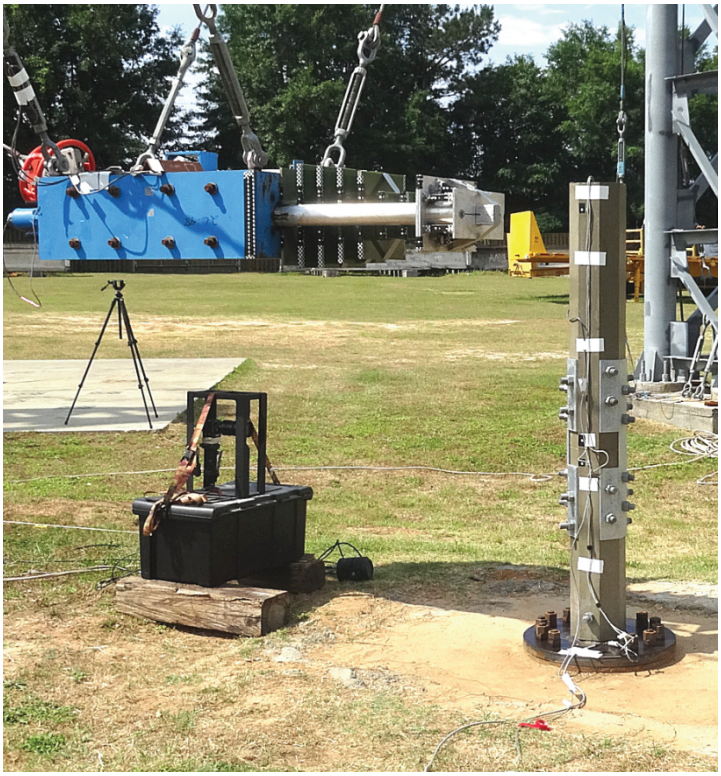

(a)

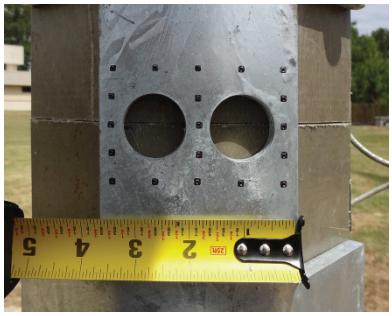

(b)

(c)

Figure 6.19 Fuse plate impact test:
(a) Experimental test setup; (b) Fuse portion of plate with tracking points;
(c) Flexural failure at base of FRP

6.4 Flexural testing

Static flexural testing of the moment collar breakaway connection was conducted at the University of Florida Structures Research Lab. Per AASHTO LTS-6 (2015), laboratory testing must demonstrate that a breakaway system possesses an adequate factor of safety relative to the design loading condition (wind in this situation). Since the design flexural capacity of the hybrid breakaway system was defined as 30 kip-ft, to satisfy AASHTO LTS-6, the FRP portion of the system had to possess a FS>2.0 (i.e., 60 kip-ft capacity), and the steel breakaway portion had to possess a FS>1.5 (i.e., 45 kip-ft capacity). Prior static flexural testing (discussed in Chapter 4) had demonstrated that the FRP composite CP076 post possessed an ultimate flexural capacity of 71 kip-ft, corresponding to a FS=2.37 (i.e. FS>2.0). Thus static flexural testing was undertaken to demonstrate that the steel breakaway portion of the system possessed an ultimate flexural capacity of (FS=1.5)(30 kip-ft)=45 kip-ft, or greater. Based on simulation results (recall Figure 6.5), it was anticipated that the steel connection would demonstrate a capacity not only greater than the required 45 kip-ft (FS>1.5), but likely greater than 60 kip-ft (FS>2.0).

Two instances of static flexural testing (configured as shown in Figure 6.20) were conducted. In each test, there were five main components: a reaction frame, a HSS 7.5x0.375 stub base, the moment collar connection, a 20-in. long HSS 7.5x0.375 stem, and an FRP composite CP076 post. Two ungalvanized test articles were fabricated by Precision Tool and

Engineering (PTE) in Gainesville, Florida. Teflon sheets were installed at all steel-to-steel contact interfaces (i.e., between the binding plates and flange plates, and between the two flange plates). Introduction of the Teflon sheets was in accordance with the intended field-installation procedure for the system. Additionally, the presence of these sheets ensured that the ungalvanized state of the test articles (vs. a galvanized state) would not unduly increase the flexural capacity of the connection during testing.

To assemble the test articles, the stub, stem, and FRP post were aligned and secured together with two halves of the moment collar. An 'approximately-fixed' support condition was created by horizontally attaching the stub to the reaction frame with four 1-1/2 in. diameter bolts. Moment collar components—specifically primary plates and binding plates—were positioned and installed flush to the flange plates. Securing bolts that connected the binding plates to primary plates were installed and torqued to 250 lbf-ft.

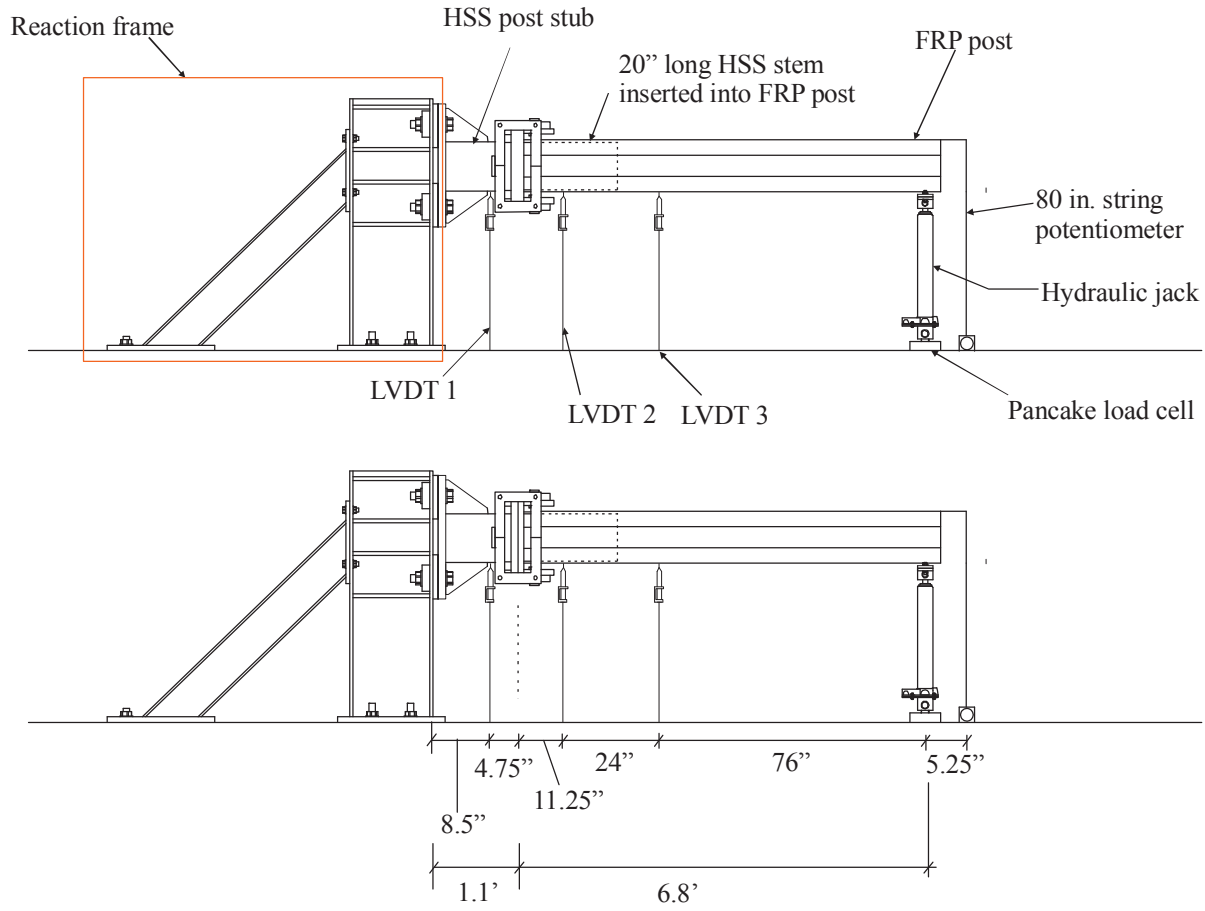

Figure 6.20 Schematic diagrams of static flexural test setup

A hydraulic jack (16 kip capacity), was used to apply load near the end of the test article, approximately 7 ft from the slipping plane (between the flange plates) of the breakaway connection. At this loading position, the load location was in agreement with specifications provided in AASHTO LTS-6, which states that load must be applied at a distance of at least five times the maximum major bending dimension of the post tested. Load applied by the hydraulic jack to the post was measured using a pancake load cell (50 kip capacity, manufactured by

National Scale Technology), positioned under the jack with a pin joint and spherical washer-set. A 1 in. thick steel support plate, anchored to the lab floor, was used as the base for the load cell.

Vertical steel guides were placed on both sides of the FRP post, at the jack location, to prevent lateral post deflection during testing. Vertical displacements were measured at several locations along the post using DCTH Series LVDTs (manufactured by RDP Electrosense) while load was applied through the jack at an approximate rate of 2 kip/min. System response during testing was monitored by way of a load vs. tip-deflection plot. Loading was continued until failure of the FRP post occurred.

6.4.1 Static flexural capacity test: unbonded HSS stem

On April 27, 2016, an initial static flexural capacity test was conducted (Figure 6.21) on the first of two hybrid connection test articles. In this test, flexural moment in the FRP composite CP076 post was transmitted into the steel HSS stem by way of a 20 in. (2.5 x the 'diameter' of the FRP post) snug-fit unbonded overlap, and a single ½ in. diameter threaded bar that passed through the neutral axes of the FRP post and steel HSS stem. Unfortunately, although load and deflection data were measured and displayed in real time during the test, corruption of the exported data file occurred after completion of the test, and detailed test results were thus not available. However, a review of video recorded during the test indicated that the maximum moment reached before failure was approximately 27 kip-ft at the slip-plane of the moment collar connection. Unexpectedly, the 27 kip-ft failure moment, which was 40% less than the 45 kip-ft needed to demonstrate adequacy of the steel breakaway connection (FS>1.5 per AASHTO LTS-6), was controlled not by formation of a plastic hinge in the steel HSS stem (recall Figure 6.4), but rather by rupture of the FRP post (Figure 6.22). Given that previous static flexural testing (Chapter 4) had shown the FRP composite post possessed an ultimate flexural capacity of 71 kip-ft, it was not anticipated that FRP rupture would occur prior to reaching 45 kip-ft in the steel connection.

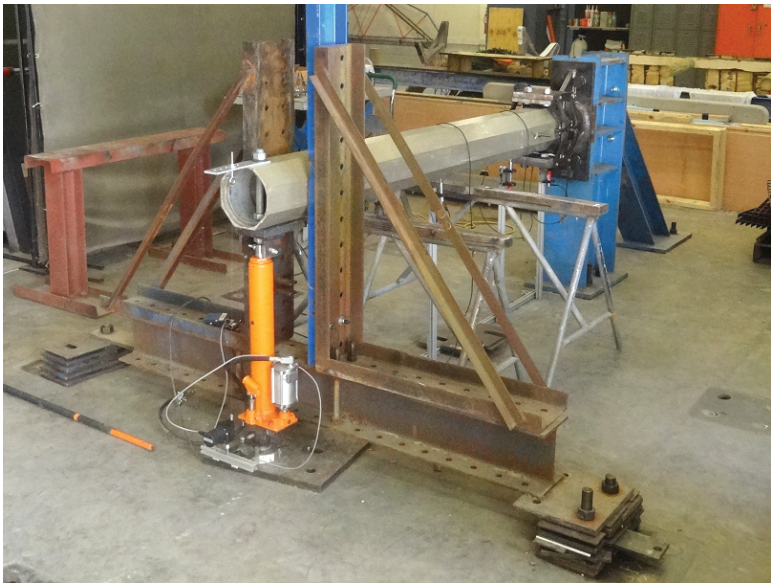

Figure 6.21 Overview of static flexural capacity test with un-epoxied stem

Flexural failure was found to be associated with the formation and propagation of longitudinal splits along the FRP post section (Figure 6.22d). As shown in Figure 6.23, longitudinal splitting occurred along two faces, located 180 deg. opposite to each other. It is noted that splitting did not occur along the faces through which the threaded bar passed, and thus was not associated with drilling holes through the FRP post to accommodate threaded bar installation.

As shown in Appendix C, the inside shape of the CP076 FRP post cross-section is *approximately* circular in form, but not perfectly so. To determine whether the mismatch between the 'approximately circular' inside geometry of the FRP CP076 section, and the 'truly circular' outside geometry of the steel HSS 7.5x0.375 stem was the cause of the lower-than-expected failure moment, an alternate installation procedure was employed in the subsequent flexural test.

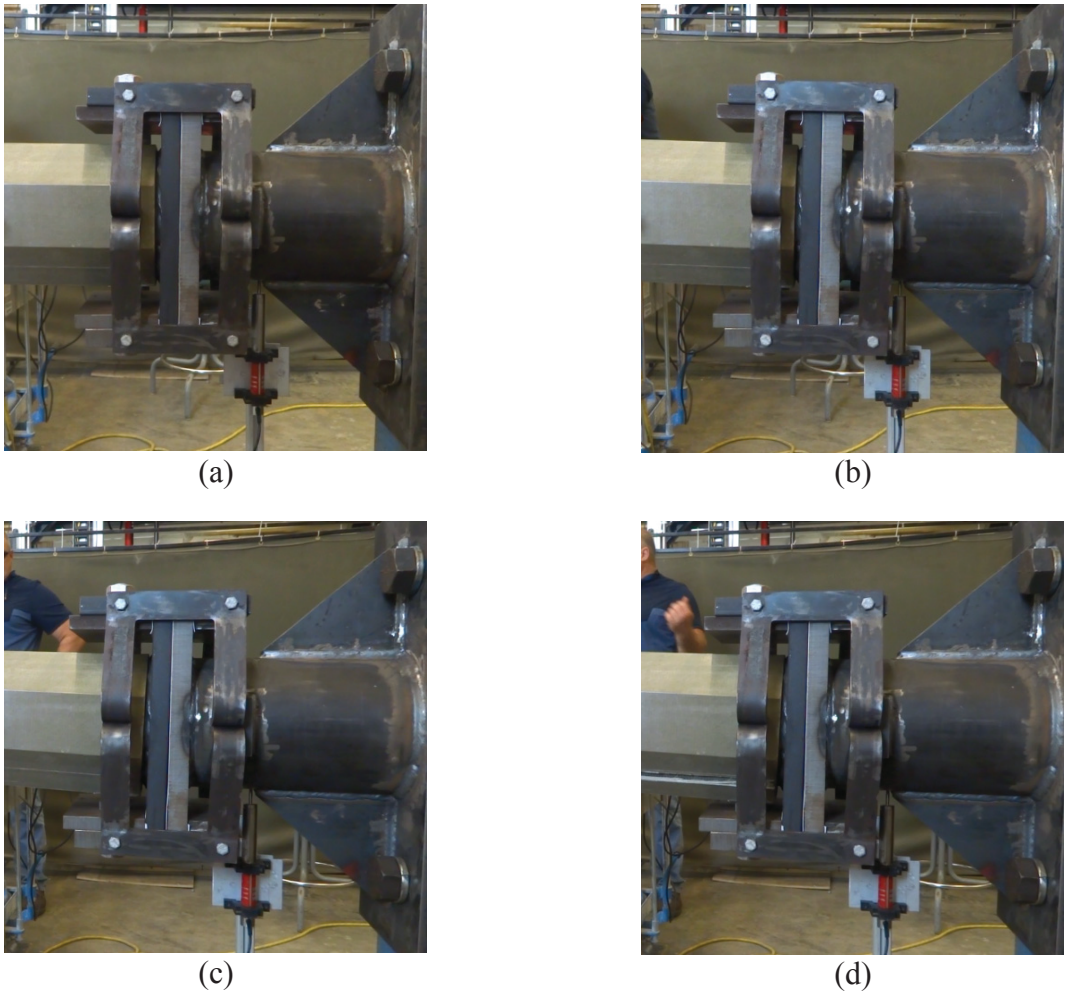

(a) (b) (c) (d)

Figure 6.22 Deformations of FRP post, breakaway moment collar connection, and base stub during flexural testing

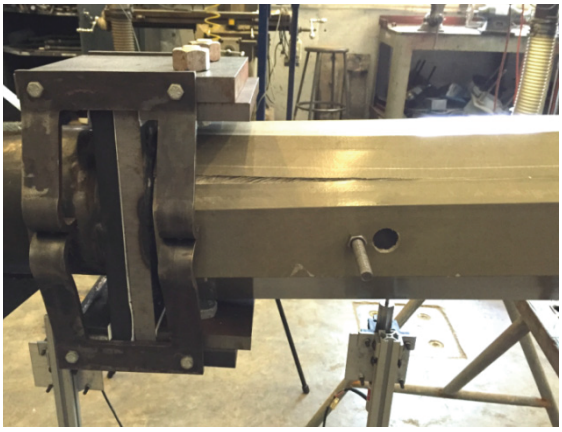

(a)

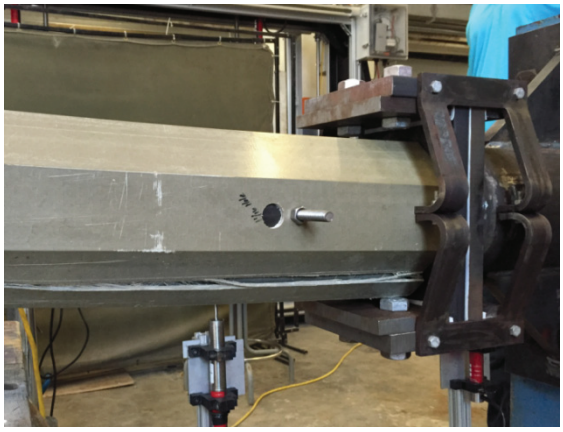

(b)

Figure 6.23 Longitudinal failure lines:
(a) North side of FRP post; (b) South side of FRP post

6.4.2 Static flexural capacity test: bonded HSS stem

To produce a matched fit—free of both interferences and gaps—between the outer surface of the steel HSS stem and the inner surface of the FRP post, and to add the aspect of bond strength (i.e., adhesion) between the steel and FRP, a modified installation procedure was developed. Using this procedure, eight (8) flattened lines were ground along the entire length of the steel HSS stem (Figure 6.24a) to produce small gaps between the steel stem and octagonal FRP pipe, even along the 'flat spots' of the FRP inner geometry (see Appendix C). Next, the flange plate to which the HSS stem was welded was taped off to prevent accidental epoxy adhesion, and the inner surface of the FRP post was thoroughly cleaned with acetone. After mixing a two-part epoxy (Concresive™, manufactured by BASF, Figure 6.24b), the entire outer surface of the steel HSS stem and ~20 in. (in length) of the inner surface of the FRP post were both liberally 'painted' with epoxy. The steel stem was then inserted into the FRP post, adjusted slightly for alignment, and then given adequate time to cure. Subsequently, the bonded stem/post assembly was installed on the stub base assembly, and the breakaway moment collar connection was attached to produce the completed test article (Figure 6.24c).

On June 21, 2016, a static flexural capacity test (Figure 6.25) was conducted on the bonded (epoxied) hybrid connection test article. In Figure 6.26, photographs of deformations in the HSS stem (hidden), FRP post, moment collar breakaway connection components, and stub base are shown at various stages of loading. As in the previous test, failure strength was controlled not by plastic hinge formation in the steel HSS stem, but rather by longitudinal splitting of the FRP post (Figure 6.26d and Figure 6.27). Also similar to the previous test, longitudinal splitting occurred along two faces that were located 180 deg. opposite to each other (Figure 6.28).

However, with the introduction of bond into the installation procedure, the flexural capacity increased from 27 kip-ft (unbonded) to 37 kip-ft (bonded). By eliminating interferences/ gaps, and by adding bond, the flexural capacity (Figure 6.29) improved, but was still less than the 45 kip-ft required by AASHTO LTS-6 for the steel breakaway connection, and far less than the 71 kip-ft produced during earlier FRP flexural testing.

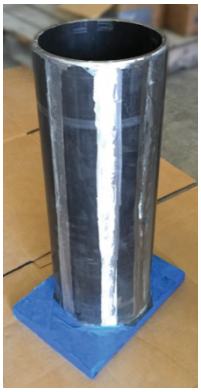

(a)

(b)

(c)

Figure 6.24 Preparation and installation of bonded test article:
(a) Steel HSS stem chamfered at end and ground flat along eight (8) lines in accordance with inner geometry of FRP CP076 post; (b) 'Concresive' two-part epoxy used to bond steel stem to FRP post; (c) HSS stem epoxied into FRP post and attached to stub base with moment collar

Figure 6.25 Overview of static flexural capacity test with epoxied stem

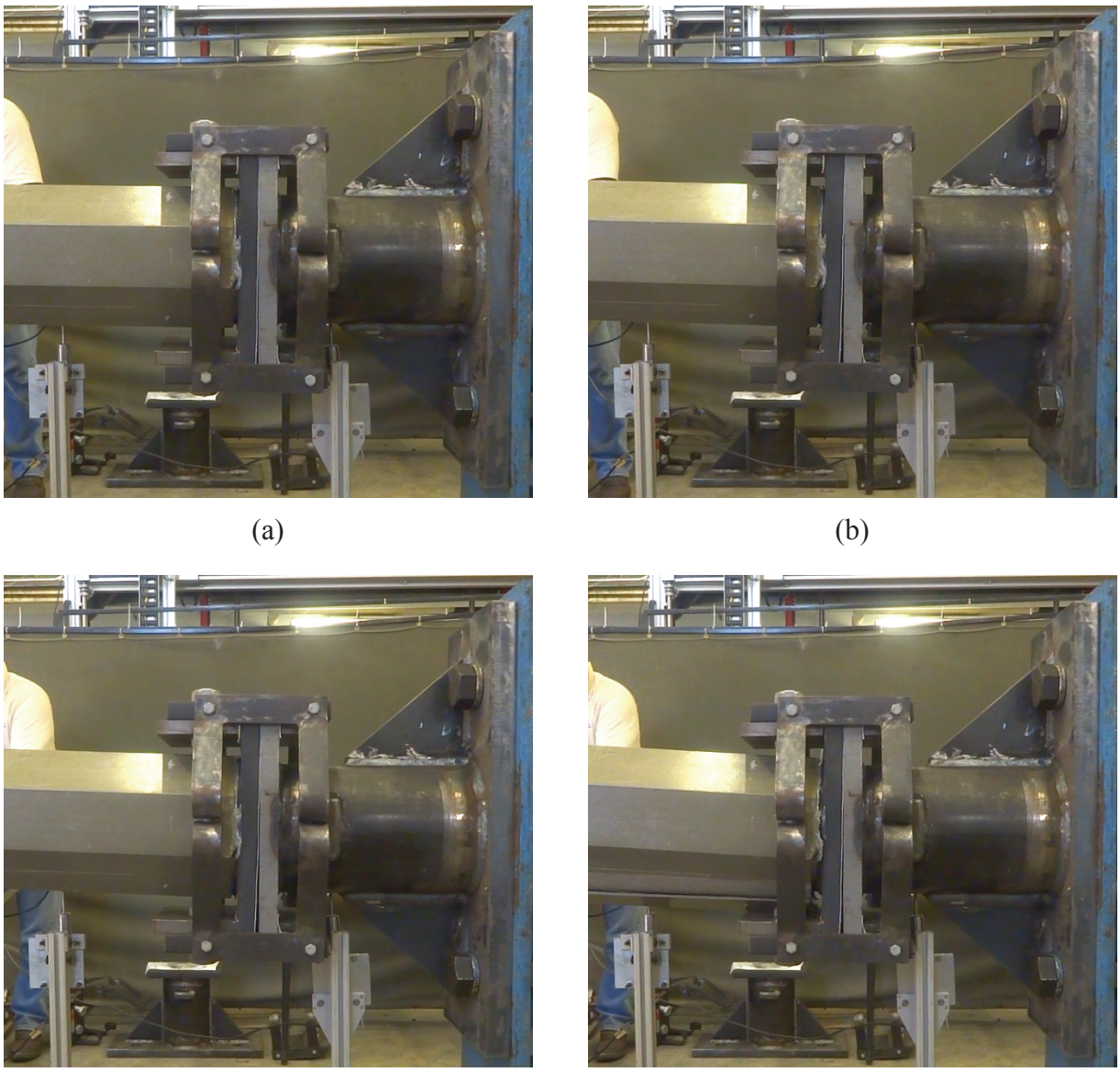

(a) (b)

(c) (d)

Figure 6.26 Deformations of FRP post, breakaway moment collar connection, and base stub during flexural testing of epoxy-installed system

Figure 6.27 Longitudinal failure line along south side of FRP post

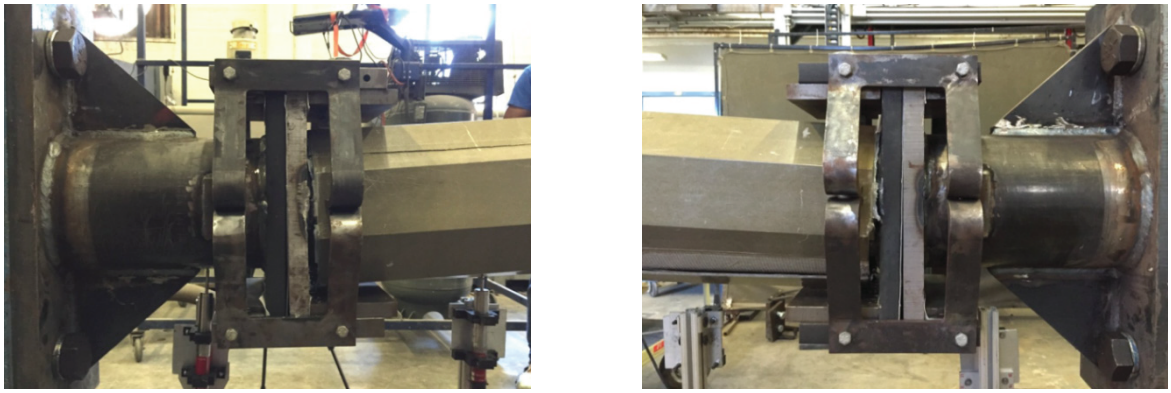

(a) (b)

Figure 6.28 Longitudinal failure lines:
(a) North side of FRP post; (b) South side of FRP post

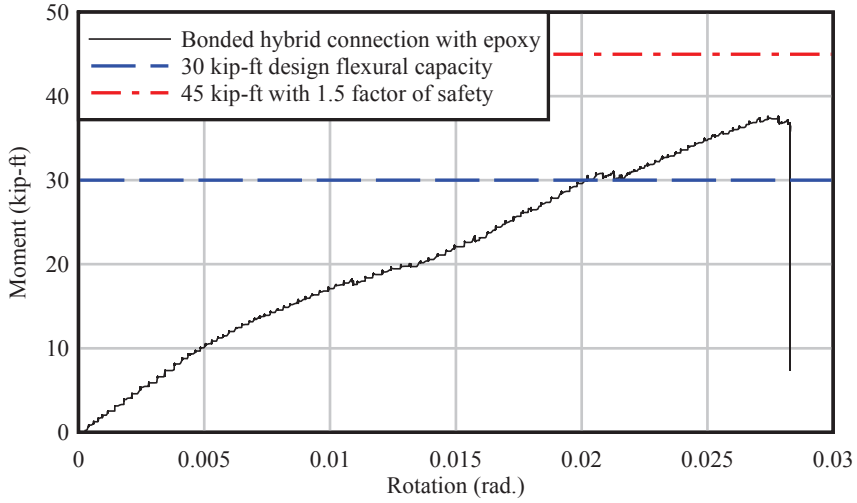

Figure 6.29 Results from static flexural capacity test of bonded (epoxied) hybrid system

6.5 Summary

Although three-point flexure testing (discussed in Chapter 4) demonstrated that the FRP CP076 section had sufficient capacity to exceed that required by AASHTO LTS-6, joining the FRP post to a steel stem in a manner that preserved the FRP capacity was found to be problematic. Failure of both the unbonded and bonded hybrid connection test articles appeared to be related to two key issues: differences in stiffness between the steel HSS stem and the FRP post, and lack of adequate circumferential fiber strength at the base-end of the FRP post. Due in part to the former (differences in stiffness), circumferential stresses in the FRP arose that helped initiate longitudinal splitting.

If additional circumferential fiber strength were added to the terminal end of the FRP post, then the observed splitting failure might be preventable. However, the disadvantage of requiring special fiber reinforcement (i.e., FRP detailing) at the end of the post section would offset a key advantage of using FRP—i.e., the ability to freely cut post segments to the length required for a particular roadside installation. Additionally, due to the relatively low bolt-bearing strength of the FRP post material, far more 1 in. dimeter threaded bars (12 in total) were necessary (to secure the steel fuse and hinge plates to the FRP post section) than would have been necessary based strictly on bar shear strength.

While combining FRP and steel components offers the promise of advantages related to reduction of weight (mass), reduction of occupant impact risk, and improvement in impact safety, to realize such benefits, it appears that specialized FRP detailing would be required, rather than the use of ‘stock’ (i.e., standard) FRP post products. While it is possible that specialized FRP detailing could remedy the flexural capacity issues encountered in this study, it is unclear whether the associated increase in FRP fabrication cost, as well as the loss of flexibility (in terms of ease of installation), would more than offset the potential benefits.

CHAPTER 7
LABORATORY ACCREDITATION

7.1 ISO 17025 Accreditation

A component of this study involved reviewing the process required for the FDOT pendulum impact test facility to gain laboratory accreditation as it relates to conducting AASHTO MASH-compliant impact tests of breakaway roadside safety hardware. Per FHWA (Federal Highway Administration) documentation, it was determined that laboratories conducting such tests "must be accredited to ISO 17025 if the [impact test] reports are to be submitted to the FHWA for acceptance purposes". ISO 17025 refers to the ISO (International Organization for Standardization) standard 17025: "General requirements for the competence of testing and calibration laboratories". It was further determined that laboratories that conduct crash/impact tests are accredited through the 'mechanical' testing accreditation program of ISO 17025, with specific test 'methods' being identified (e.g., NCHRP 350, AASHTO MASH, etc.). In fact, test 'facilities' themselves are not accredited; rather, the competency of such facilities to conduct specific tests (e.g., AASHTO MASH Test 3-60) is actually what is accredited.

To assist the FDOT Structures Research Center in assessing the effort required to gain accreditation for MASH-compliant pendulum impact testing, the following steps were carried out:

- Discussions with NCAC & FHWA FOIL: Engineers at the NCAC (National Crash Analysis Center) and at the FHWA FOIL (Federal Outdoor Impact Laboratory) were contacted to discuss laboratory accreditation procedures as they pertain to AASHTO MASH pendulum impact testing of roadside hardware. Discussion topics additionally covered best strategies for successful accreditation; options with regard to accreditation bodies; gaining assistance from an accreditation specialist; costs; and future maintenance of accreditation.

- ISO 17025 accreditation process: A review of the overall ISO 17025 mechanical accreditation process was conducted, including: the purchase and comprehensive review of the ISO 17025 document; identification of the appropriate accreditation body; detailed steps involved in the accreditation process; and accreditation maintenance requirements.

- Determination of costs: The accreditation body A2LA (the American Association for Laboratory Accreditation) was contacted to obtain a 'mechanical ISO 17025' accreditation cost estimate.

- Accreditation specialist: Qualifications from specialists interested in assisting UF/FDOT in the ISO 17025 accreditation process were solicited and a suitable specialist was selected. Discussions between the accreditation specialist, UF, and the FDOT Structures Research Center were carried out to review ISO 17025 accreditation procedures, scope, and effort; best strategies for successfully gaining accreditation; typical tests conducted using the FDOT pendulum impact test facility; the current state of FDOT documentation related to laboratory management and quality assurance; and other issues.

- Example documentation: Based on discussions with the accreditation specialist, development of a comprehensive laboratory Quality Management System (QMS) for the FDOT Structures Research Center was identified as being a critical component of the ISO 17025 accreditation process. To help gauge the level of detail typically included in such a document, and the preparation effort necessary, an example FDOT QMS document was obtained. Specifically, the QMS document developed by the FDOT SMO (State Materials Office) in connection to ISO 17025 accreditation of SMO for testing of construction materials (not impact testing), was obtained and reviewed.

At the conclusion of these steps, it was determined that the FDOT Structures Research Center will pursue pendulum impact accreditation in an incremental manner, wherein the internal documentation necessary for ISO 17025 accreditation (e.g., QMS documents) will be developed over time, and in conjunction with ongoing laboratory quality assurance measures.

CHAPTER 8
CONCLUSIONS

8.1 Development of 1100C surrogate vehicle for pendulum impact testing

To facilitate experimental impact testing of breakaway roadside safety hardware—using the FDOT pendulum impact test facility at the FDOT Structures Research Center—a new crushable nose surrogate vehicle has been developed, tested, and validated. Since NCHRP 350 is being phased out as the accepted standard for the design of roadside safety hardware, and AASHTO MASH is being phased in, the new surrogate vehicle has been designed to be consistent with MASH—specifically, consistent with the 1100C small car defined by MASH. Impact force and vehicle deformation data collected from separate full-scale crash testing of a Kia Rio production passenger car with a mass of 1,100 kg were used to design an innovative new crushable nose impactor that closely mimics the behavior of the Kia Rio during frontal impacts.

Similar to crushable nose impactors used at other (non-FDOT) pendulum impact test facilities, the FDOT surrogate vehicle utilizes low-cost, consumable, replaceable aluminum honeycomb cartridges to generate the desired force-deformation behavior. However, the newly designed 1100C impactor differs from existing designs in several ways: (1) it is intended specifically for use in low speed (19-mph) 1100C impact testing of breakaway hardware (and therefore uses fewer consumable cartridges than the alternate NCAC system); (2) it uses tapered (i.e., trapezoidal) aluminum honeycomb cartridges that yield an improved approximation of the production vehicle force-deformation curve; and (3) the cartridge design process incorporated new insights gained through high-deformation compression testing of aluminum honeycomb materials.

Rigid pole validation impact testing of the surrogate vehicle, conducted using the FDOT gravity pendulum, yielded force-deformation data that are in good agreement with the production vehicle (Kia Rio) data. To date, the new 1100C crushable nose impactor has been used to conduct more than 15 low speed, small car impact tests on approximately six (6) different breakaway structural systems, as well as rigid structures.

8.2 Use of FRP in breakaway roadside sign structures

With the goal of increasing roadside safety by reducing occupant risks during vehicle collisions with large sign structures, ‘hybrid’ breakaway structural systems—employing both fiber-reinforced polymer (FRP) and steel—have been designed, fabricated, and subjected to both impact testing and static flexural testing in this study. The risk of occupant injury occurring when a vehicle collides with a breakaway sign structure generally decreases as the weight (and mass) of the sign structure decreases. Reducing the inertial resistance (mass) of breakaway components reduces vehicle decelerations—and therefore occupant deceleration—during impact, and thus also reduces measures of occupant risk such as occupant impact velocity (OIV). Since a substantial portion of sign structure mass is concentrated in the vertical support posts, the use FRP posts—which are considerably lighter than traditional steel posts—has been investigated in this study. Specifically, an 8 in. diameter octagonal cross-section FRP composite post (CP076, manufactured by Creative Pultrusions, Inc.) was selected and used to develop two separate hybrid breakaway design concepts. In the first, circular cutting blades—manufactured from machined steel pipe sections—were used to form a ‘shear collar’ (essentially, circular scissors)

that sliced through the FRP post during vehicle impact loading. In the second, the FRP post was joined to a steel 'moment collar' breakaway connection.

Pendulum impact testing of the shear collar concept demonstrated that the machined steel blades were able to successfully cut through the cross-section of the FRP pipe, thereby breaking the sign post away from the base. However, it was noted that fabrication costs associated with forming the cutting blades could potentially elevate overall connection construction costs. Additionally, concern was noted over whether the cutting efficacy of the blades might degrade over time, due to corrosion-induced dulling, and thus increase occupant risk measures such as OIV and ORA.

Consequently, an alternative hybrid design approach was investigated in which a steel breakaway base connection was combined with FRP composite posts. A 'moment collar' breakaway base connection developed in a parallel study (BDV31-977-24, Consolazio and Innocent 2016), intended for use with steel wide-flange sign posts, was adapted in the present study for integration with FRP posts. The wide-flange steel post of the BDV31-977-24 system was replaced with a circular steel HSS (hollow structural shape) stub which was, in turn, inserted into the CP076 FRP sign post. Pendulum impact testing of the system, conducted using the 1100C surrogate vehicle, yielded OIV and ORA results within MASH limits, and indicated good agreement with *a priori* finite element predictions of behavior. However, whereas 3-point bending tests conducted earlier in the study confirmed that the CP076 section possessed adequate capacity for the intended application, flexural testing of the *integrated* FRP post and steel breakaway connection system failed to achieve the necessary capacity. To increase the flexural capacity of the integrated system, a subsequent test was conducted wherein the HSS stub was epoxied into the FRP post. Despite the epoxy bond that was present between the FRP and steel, the FRP post still failed prematurely, and at a flexural moment well below that previously obtained from 3-point bending tests.

Results from multiple series of tests (Table 8.1) on hybrid FRP/steel connection systems developed in this study indicate that while the lighter weight of FRP posts—relative to steel posts—offers the prospect of reduced occupant risk during collision, realizing such benefits may require connection detailing that is more complex and costly than would typically be required in an all-steel breakaway system.

Table 8.1 Summary of results from experimental impact tests of hybrid breakaway systems

Breakaway system	Risk parameter	Risk value
Shear collar	Occupant impact velocity (OIV)	16.7 ft/sec
	Occupant ride-down acceleration (ORA)	0.9 g
Moment collar (0 deg.)	Occupant impact velocity (OIV)	8.9 ft/sec
	Occupant ride-down acceleration (ORA)	0.27 g
Moment collar (25 deg.)	Occupant impact velocity (OIV)	8.8 ft/sec
	Occupant ride-down acceleration (ORA)	0.26 g

8.3 Accreditation of FDOT pendulum impact test facility

A component of this study involved reviewing the process required for the FDOT pendulum impact test facility to gain ISO 17025 laboratory accreditation as it relates to conducting AASHTO MASH-compliant impact tests of breakaway roadside safety hardware. Pertinent accreditation documents were acquired and reviewed; accreditation cost estimates were obtained; an accreditation specialist was selected and consulted in regard to scope of effort required; and Quality Management System (QMS) documents previously developed by the FDOT SMO (State Materials Office) in relation to ISO 17025 accreditation were obtained and reviewed. Based on document reviews, discussions with the ISO 17025 accreditation specialist, and internal departmental discussions, the FDOT Structures Research Center will pursue pendulum impact accreditation in an incremental manner, wherein the internal documentation necessary for ISO 17025 accreditation (e.g., QMS documents) will be developed over time, and in conjunction with ongoing laboratory quality assurance measures.

REFERENCES

AASHTO (2009), *Manual for Assessing Safety Hardware (MASH),* American Association of State Highway and Transportation Officials, Washington, D.C., 2009.

AASHTO (2013), *Standard Specification for Structural Supports for Highway Signs, Luminaires and Traffic Signals, 6th Edition (LTS-6)*, American Association of State Highway and Transportation Officials, Washington, D.C., 2013.

AASHTO (2015), *Interim Revisions to Standard Specification for Structural Supports for Highway Signs, Luminaires and Traffic Signals, 6th Edition (LTS-6)*, American Association of State Highway and Transportation Officials, Washington, D.C., 2015.

AISC (2005), Steel Construction Manual, 13th Ed., American Institute of Steel Construction, Chicago, IL.

Consolazio, G., Bui, L., and Walters, R. (2012). *Pendulum impact testing of an impact-breakaway, wind resistant base connection for multi-post ground signs* (FDOT Research Project BDK75-977-40), Structures Research Report No. 2012/92174, University of Florida, Gainesville, FL.

Consolazio, G. and Innocent, D. (2016). *Scaling and validation of breakaway connection for multi-post ground signs* (FDOT Research Project BDV31-977-24), Structures Research Report No. 2016/114986-114987, University of Florida, Gainesville, FL.

FDOT LTS-6 (2015), *FDOT Modifications to Standard Specification for Structural Supports for Highway Signs, Luminaires and Traffic Signals (LTS-6)*, FDOT Structures Manual, Vol. 3, Florida Department of Transportation, Tallahassee, FL, Jan. 2015.

FDOT SDG (2015), *FDOT Structures Design Guidelines*, FDOT Structures Manual, Vol. 1, Florida Department of Transportation, Tallahassee, FL, Jan. 2015.

Kantrales G.C., G.R. Consolazio, D. Wagner, and S. Fallaha. (2015), "Experimental and Analytical Study of High-Level Barge Deformation for Barge-Bridge Collision Design", *J. Bridge Eng.,* 2015, http://ascelibrary.org/doi/10.1061/(ASCE)BE.1943-5592.0000801.

LSTC (Livermore Software Technology Corporation) (2014). *LS-DYNA Keyword User's Manual*. LSTC, Livermore, CA.

Marzougui, D., C. Story, L. Nix, C.D. Kan , and E. Arispe. *Crash Testing of Kia Rio Sedans into an Instrumented Rigid Pole*. NCAC 2011-R-005. National Crash Analysis Center, Ashburn, VA., 2011.

Marzougui, D., S. Dolci, C. Story, and A. Eskandarian. *1100C Pendulum Nose Development*. NCAC 2012-R-003. National Crash Analysis Center, Ashburn, VA., 2013.

Ross H.E., Jr., D.L. Sicking, R.A. Zimmer, and J.D. Michie (1993). *NCHRP Report 350: Recommended Procedures for the Safety Performance Evaluation of Highway Features*. TRB, National Research Council, Washington, D.C.

APPENDIX A
STRUCTURAL DRAWINGS: 1100C SURROGATE VEHICLE IMPACT-BLOCK

Presented in this appendix are fabrication drawings for the 1100C surrogate vehicle impact-block (i.e., ‘back-block’) components.

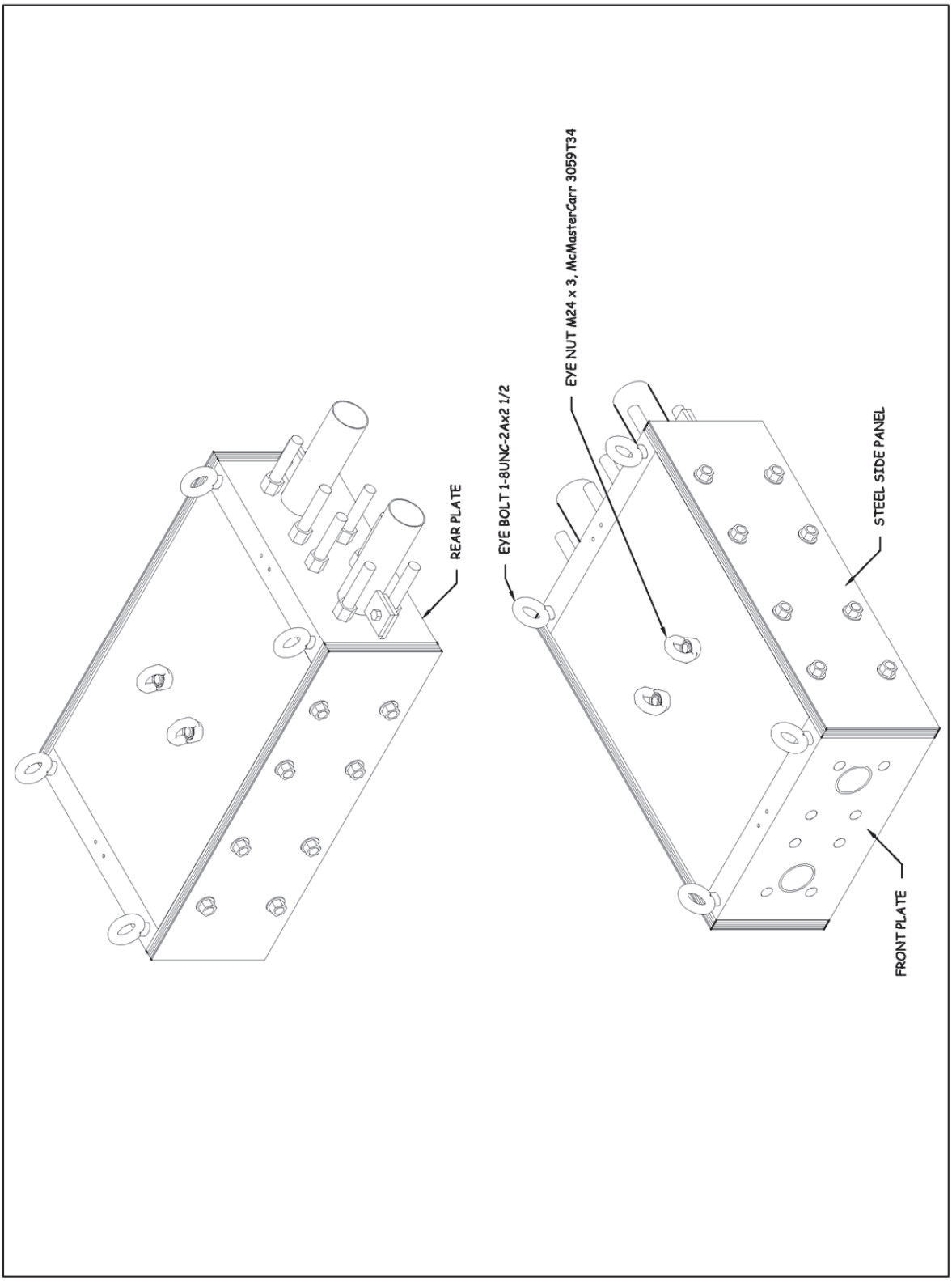
REAR PLATE
EYE BOLT 1-8UNC-2Ax2 1/2
EYE NUT M24 x 3, McMasterCarr 3059T34
STEEL SIDE PANEL
FRONT PLATE

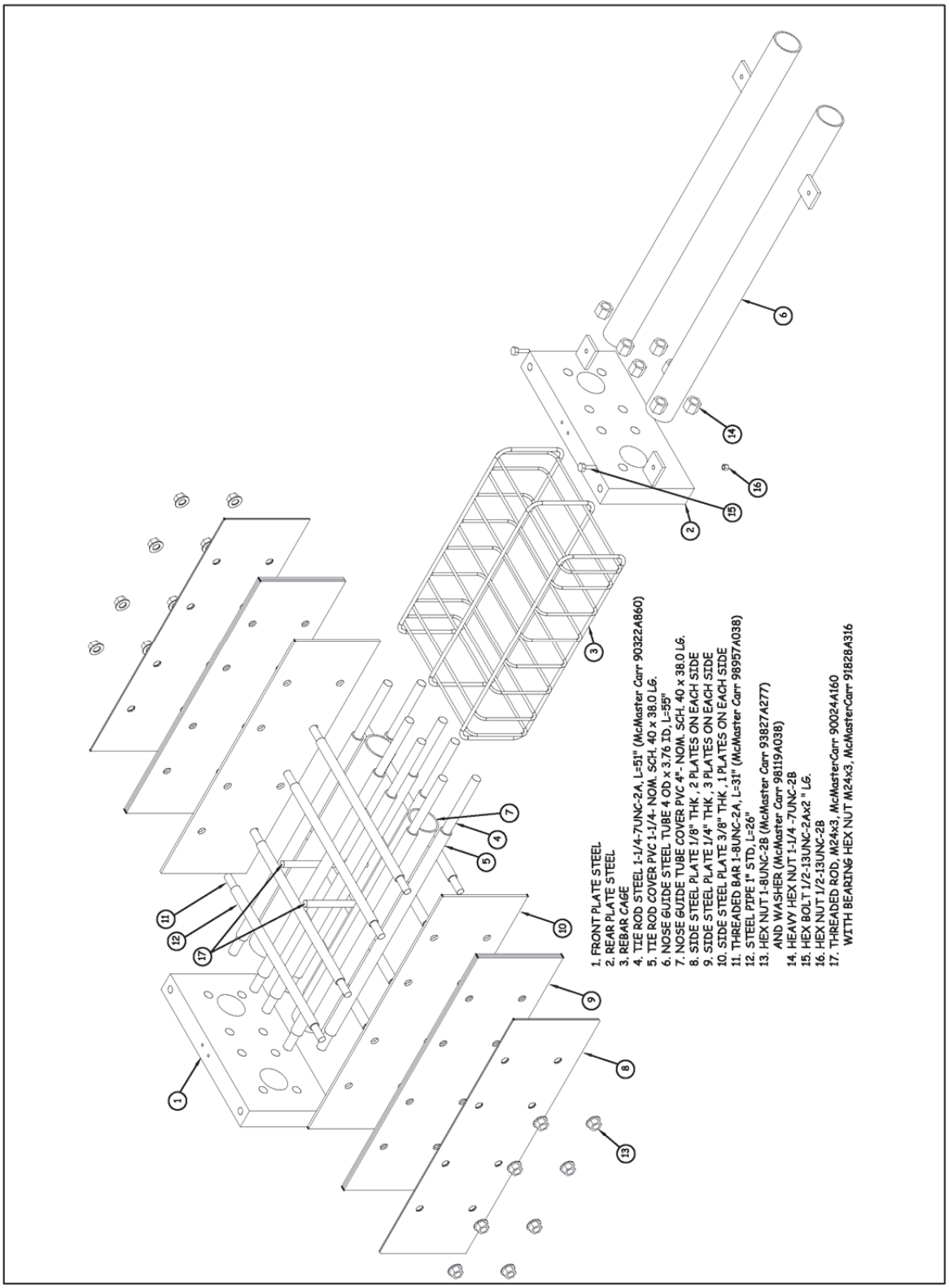
1. FRONT PLATE STEEL
2. REAR PLATE STEEL
3. REBAR CAGE
4. TIE ROD STEEL 1-1/4-7UNC-2A, L=51" (McMaster Carr 90322A860)
5. TIE ROD COVER PVC 1-1/4- NOM. SCH. 40 x 38.0 LG.
6. NOSE GUIDE STEEL TUBE 4 OD x 3.76 ID, L=55"
7. NOSE GUIDE TUBE COVER PVC 4"- NOM. SCH. 40 x 38.0 LG.
8. SIDE STEEL PLATE 1/8" THK , 2 PLATES ON EACH SIDE
9. SIDE STEEL PLATE 1/4" THK , 3 PLATES ON EACH SIDE
10. SIDE STEEL PLATE 3/8" THK , 1 PLATES ON EACH SIDE
11. THREADED BAR 1-8UNC-2A, L=31" (McMaster Carr 98957A038)
12. STEEL PIPE 1" STD, L=26"
13. HEX NUT 1-8UNC-2B (McMaster Carr 93827A277)
AND WASHER (McMaster Carr 98119A038)
14. HEAVY HEX NUT 1-1/4 -7UNC-2B
15. HEX BOLT 1/2-13UNC-2Ax2 " LG.
16. HEX NUT 1/2-13UNC-2B
17. THREADED ROD, M24x3, McMasterCarr 90024A160
WITH BEARING HEX NUT M24x3, McMasterCarr 91828A316

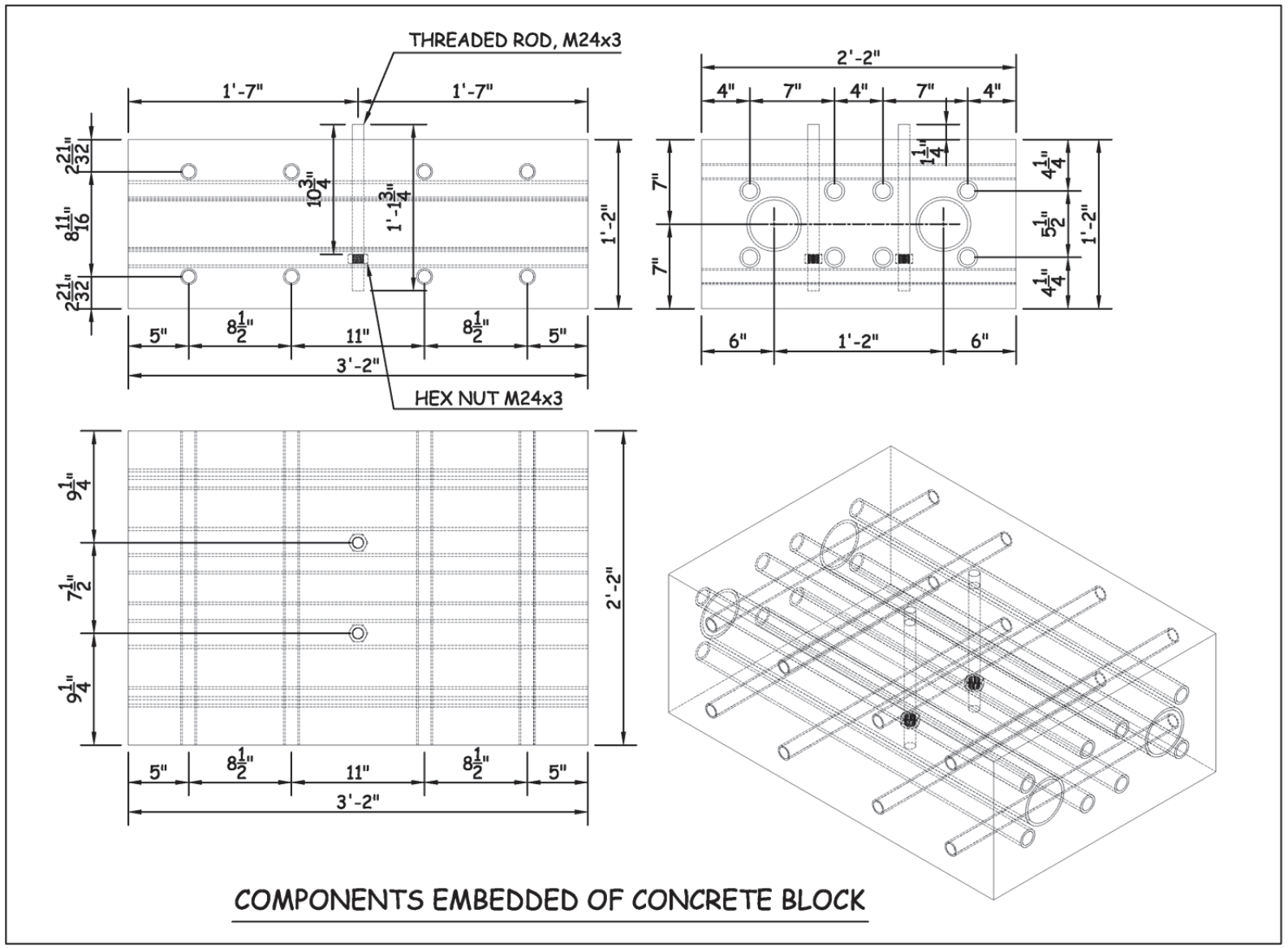
THREADED ROD, M24x3
1'-7"
1'-7"
2'-2"
4"
7"
4"
7"
4"
HEX NUT M24x3
5"
11"
3'-2"
6"
1'-2"
COMPONENTS EMBEDDED OF CONCRETE BLOCK

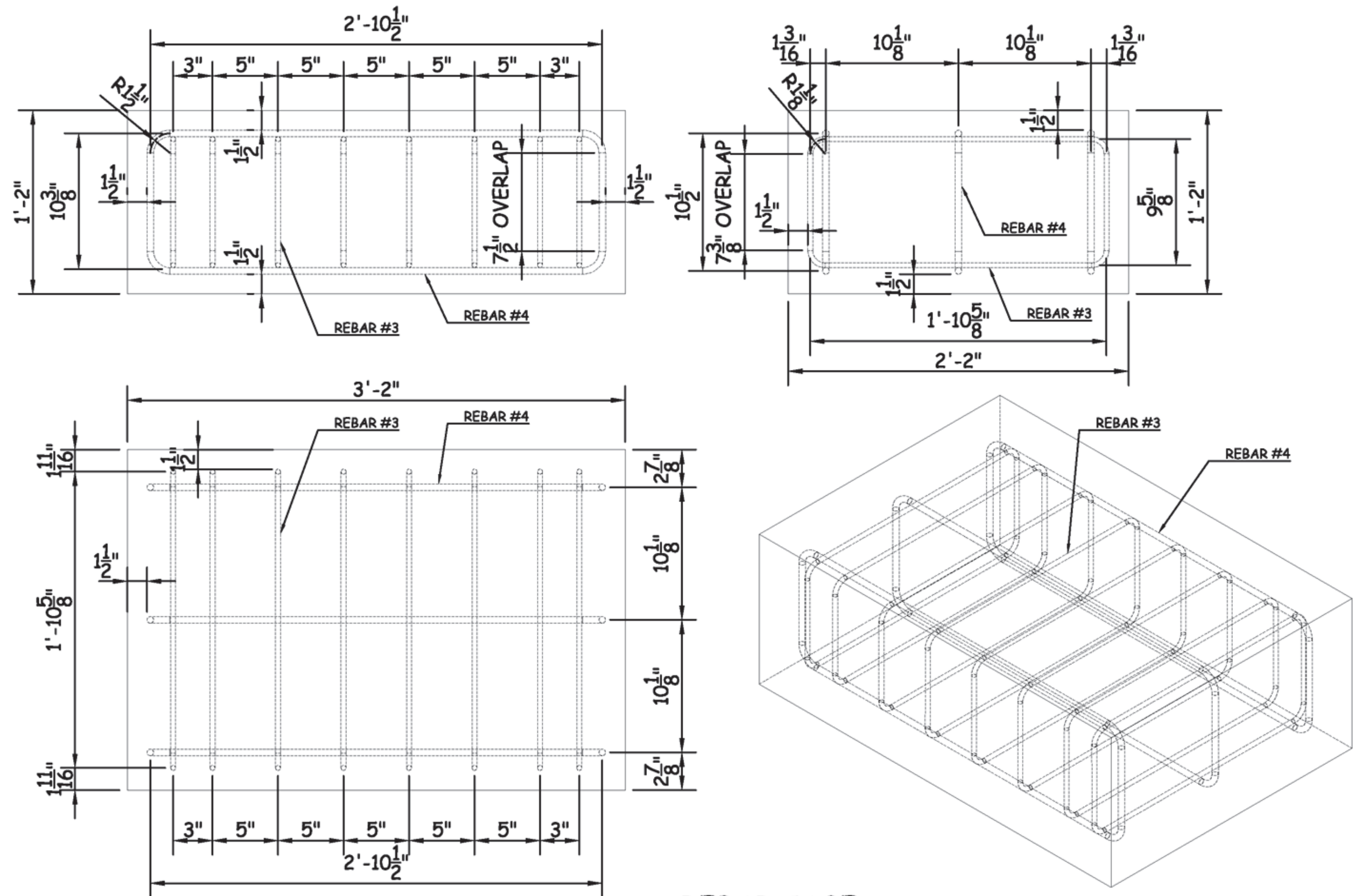
2'-10½"
3"
5"
5"
5"
5"
5"
3"
R1½"
1'-2"
10⅜"
1½"
1½"
1½"
1½"
7½" OVERLAP
REBAR #3
REBAR #4
1 3/16"
10⅛"
10⅛"
1 3/16"
R1⅛"
10½"
7⅜" OVERLAP
1½"
1½"
1½"
REBAR #4
REBAR #3
9⅝"
1'-2"
1'-10⅝"
2'-2"
3'-2"
REBAR #3
REBAR #4
1 11/16"
1½"
1½"
1'-10⅝"
1 11/16"
2⅞"
10⅛"
10⅛"
2⅞"
3"
5"
5"
5"
5"
5"
3"
2'-10½"
REBAR #3
REBAR #4

REBAR CAGE

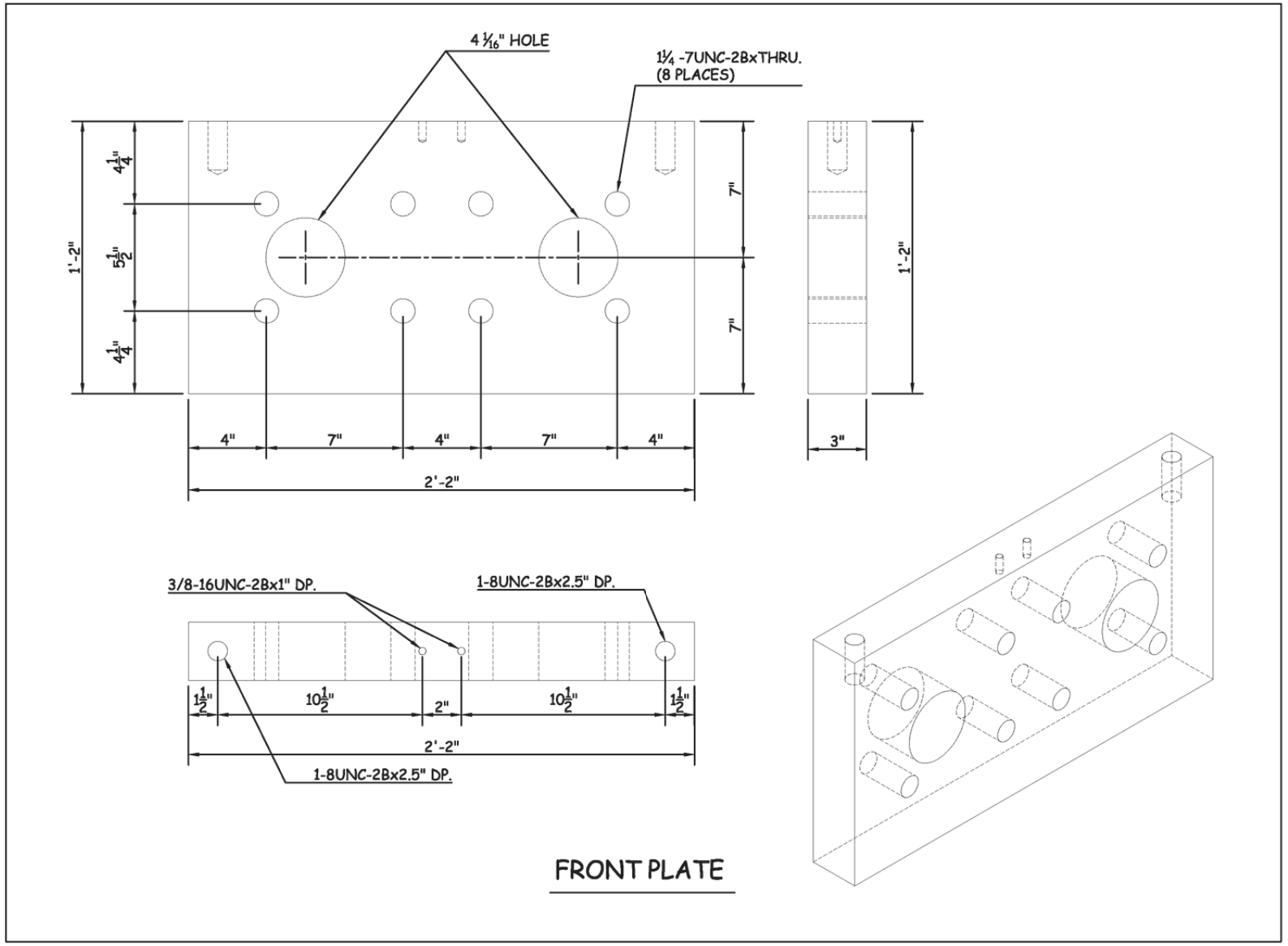
4 1/16" HOLE
1¼ -7UNC-2BxTHRU.
(8 PLACES)
4¼"
5½"
4¼"
1'-2"
7"
7"
1'-2"
4"
7"
4"
7"
4"
2'-2"
3"
3/8-16UNC-2Bx1" DP.
1-8UNC-2Bx2.5" DP.
1½"
10½"
2"
10½"
1½"
2'-2"
1-8UNC-2Bx2.5" DP.
FRONT PLATE

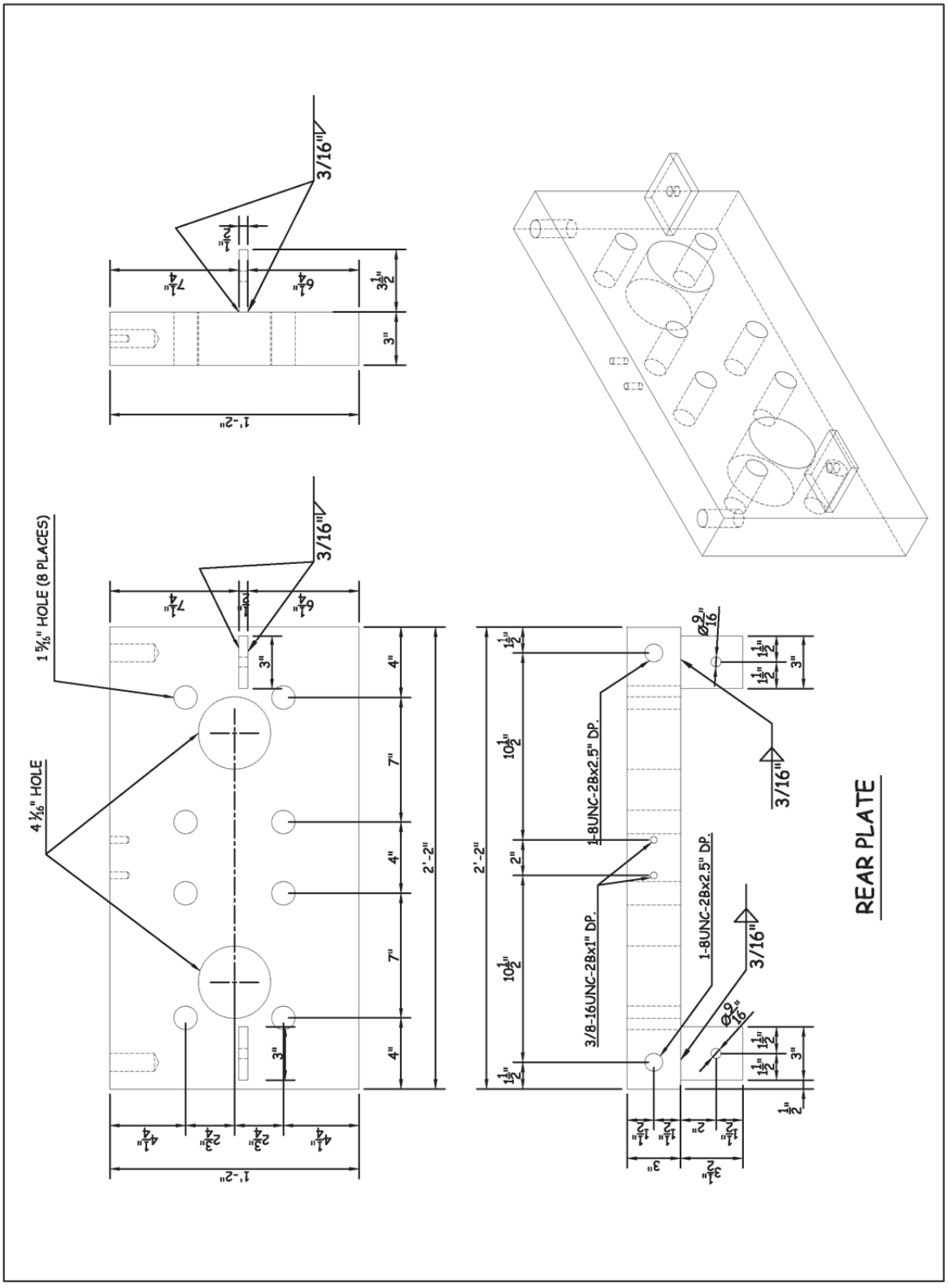
REAR PLATE
1 5/16" HOLE (8 PLACES)
4 1/16" HOLE
3/16"
3/8-16UNC-2Bx1" DP.
1-8UNC-2Bx2.5" DP.
2'-2"
1'-2"

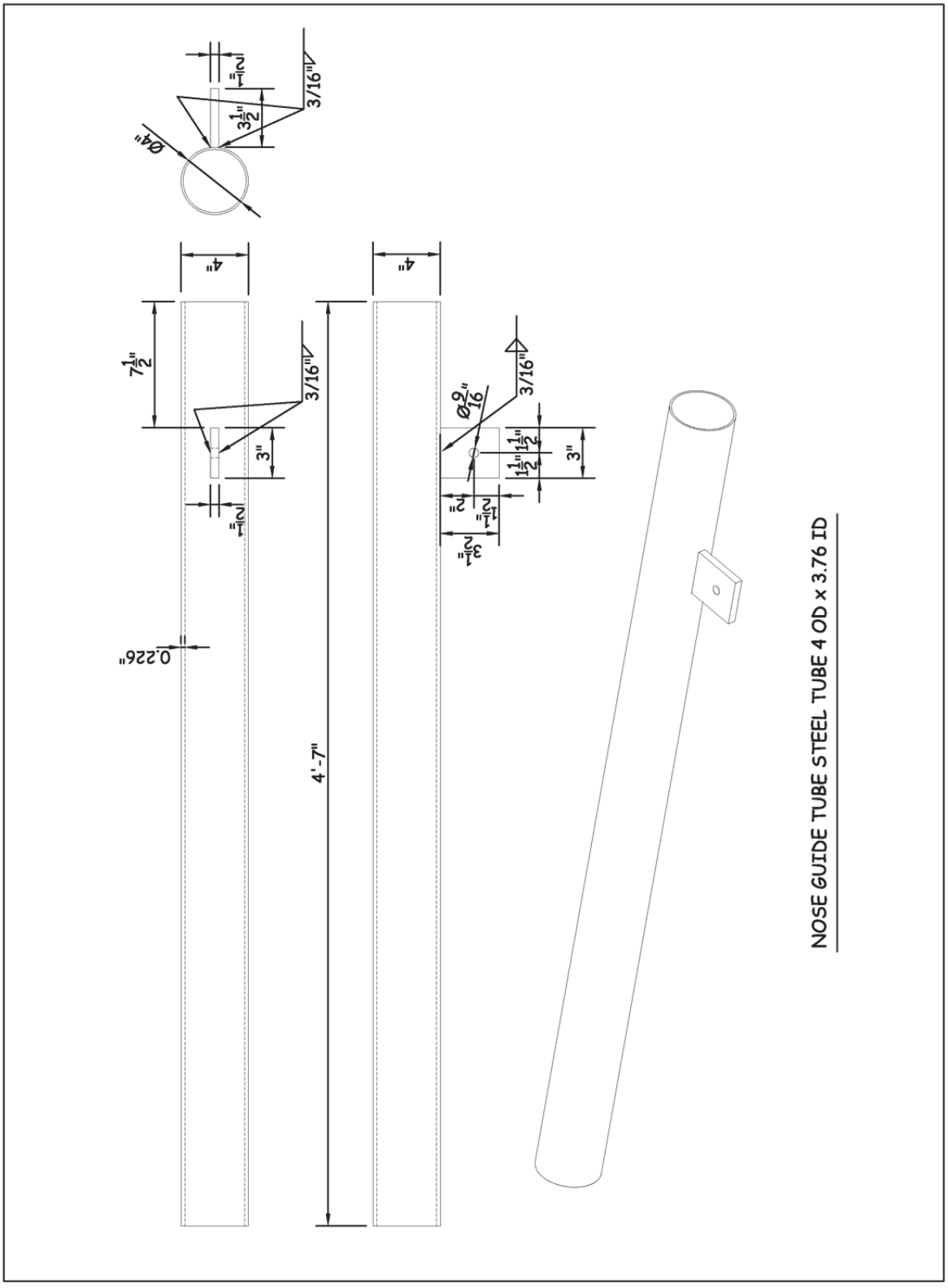

NOSE GUIDE TUBE STEEL TUBE 4 OD x 3.76 ID

3'-8"
8"
8 1/2"
11"
8 1/2"
8"
Ø1 1/16" (8 PLACES)
1'-2"
2 21/32"
8 11/16"
2 21/32"
1/4"
4 1/4"
SIDE STEEL PLATE (QTY: 6)
3'-8"
8"
8 1/2"
11"
8 1/2"
8"
Ø1 1/16" (8 PLACES)
1'-2"
2 21/32"
8 11/16"
2 21/32"
3/8"
8 3/8"
SIDE STEEL PLATE (QTY: 2)

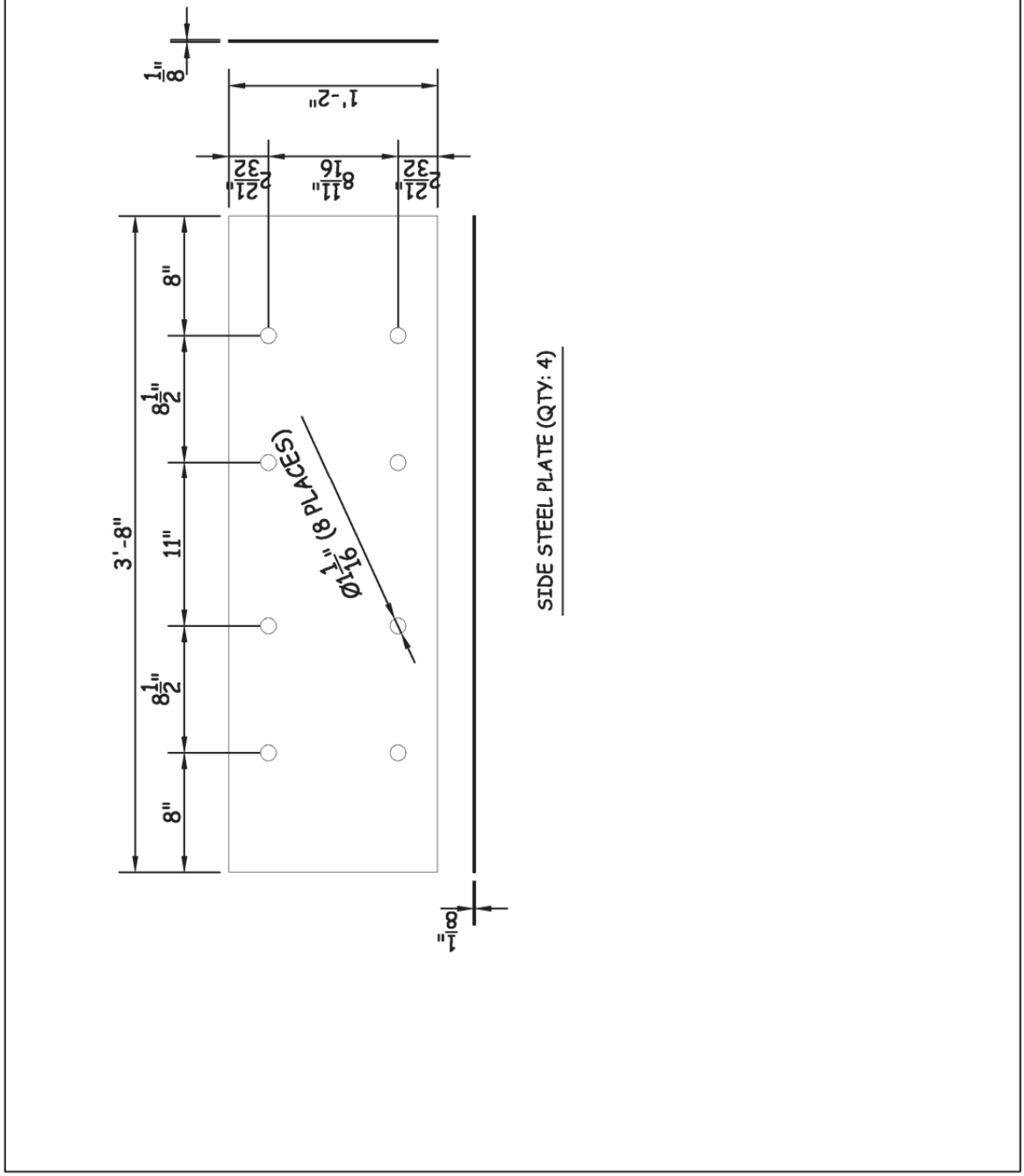

SIDE STEEL PLATE (QTY: 4)

1'-2"
2'-6 3/4"
9 1/4"
7 1/2"
9 1/4"
3/8"
4"
7"
4"
7"
4"
3/8"
2'-2"
1/4"
1/4"
3'-8"
1'-10"
1'-10"
7"
11"
8"
8 1/2"
11"
8 1/2"
8"
2 21/32"
8 11/16"
2 21/32"
1'-2"
5"
4"
5"
4'-7"
3'-2"
2'-6 3/4"
2'-2"
10"
7"
7"
4"
4"
4"
4"
4"
3"
5"
8 1/2"
11"
8 1/2"
5"
3"
3'-8"
4'-3"

APPENDIX B
STRUCTURAL DRAWINGS: SURROGATE VEHICLE CRUSHABLE-NOSE

Presented in this appendix are fabrication drawings for the 1100C surrogate vehicle crushable-nose (i.e., ‘front block’, or ‘impact-head’) components.

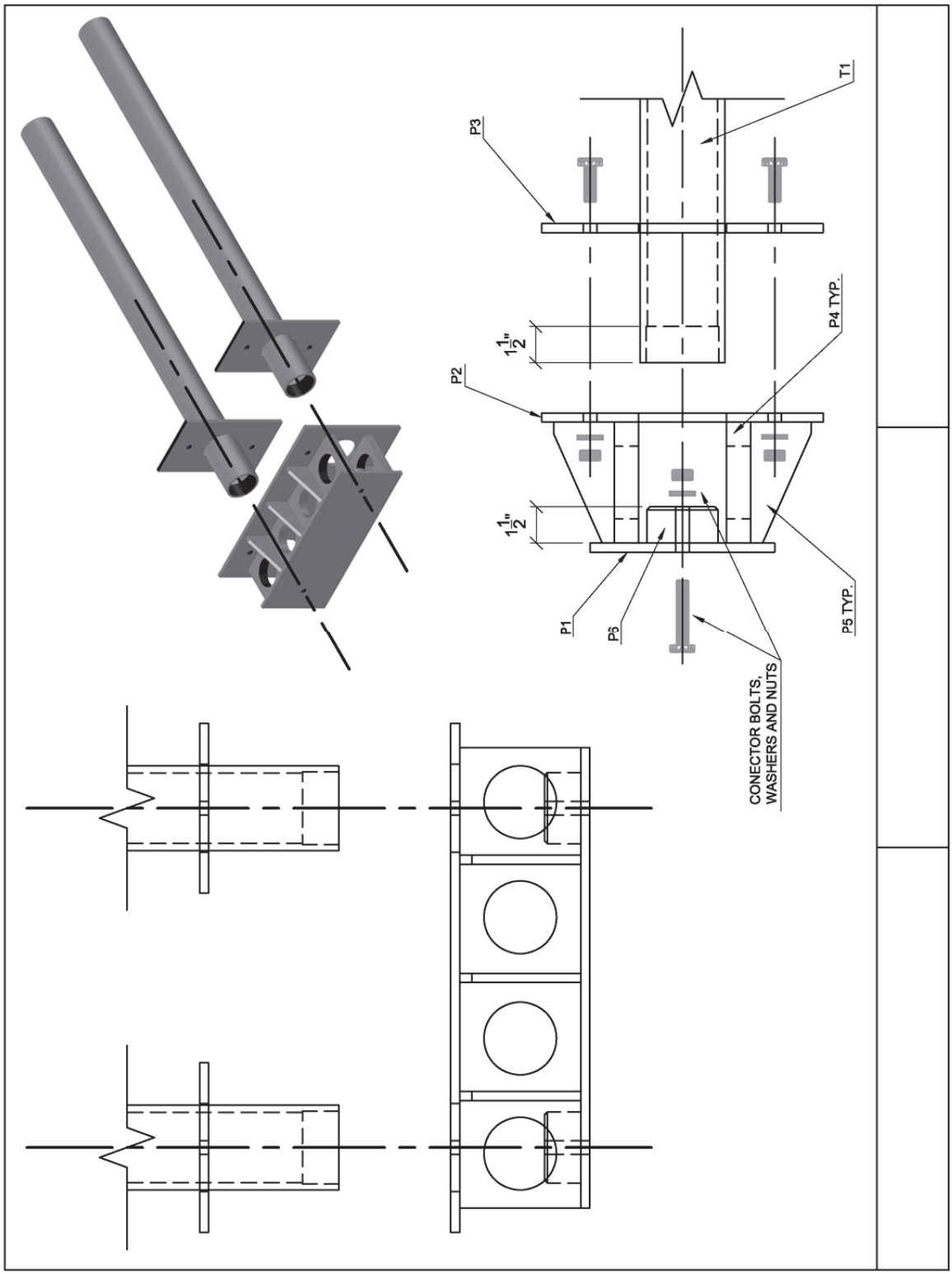
T1
P3
P4 TYP.
P2
1 1/2"
1 1/2"
P1
P3
P5 TYP.
CONECTOR BOLTS,
WASHERS AND NUTS

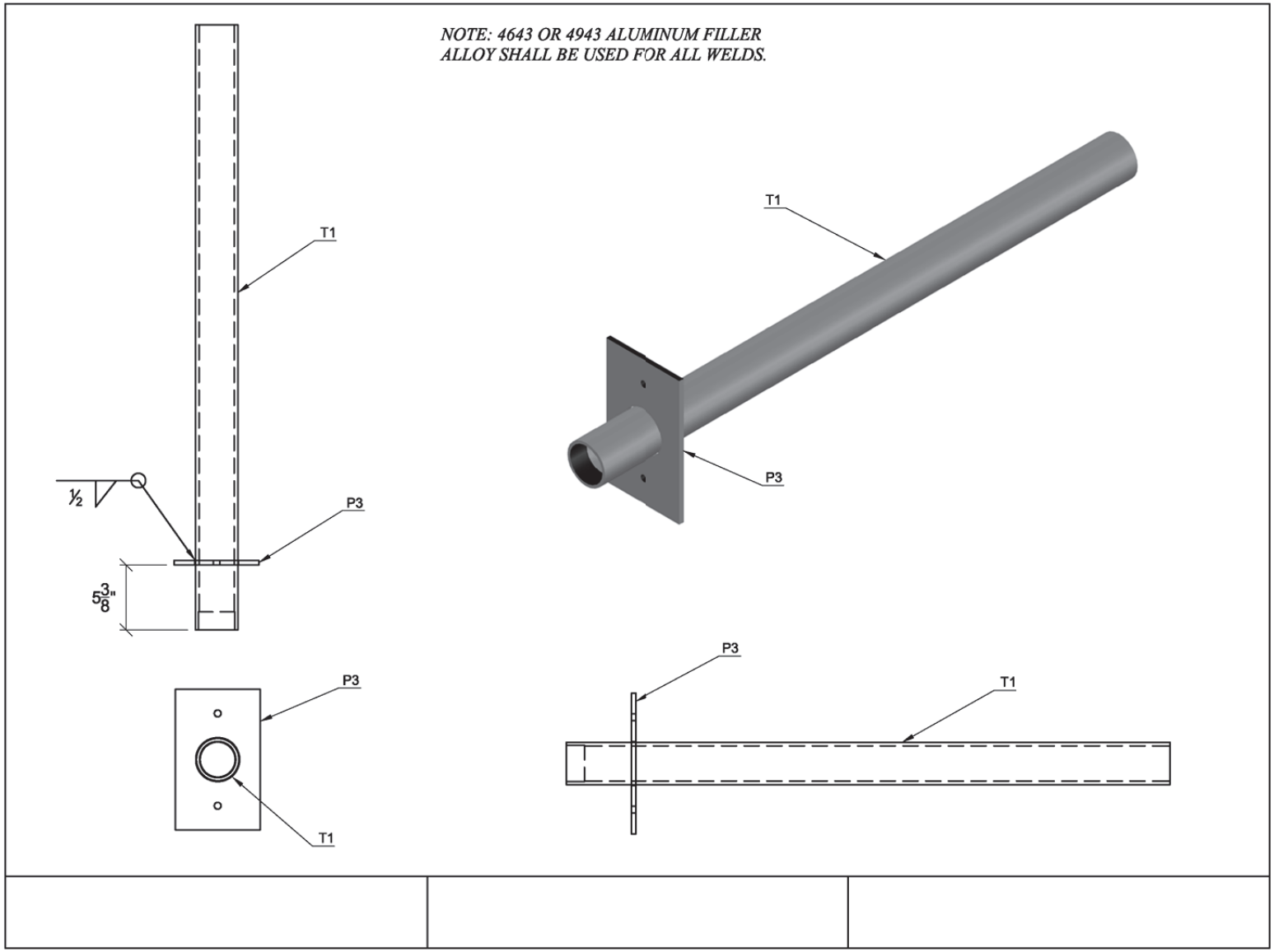
NOTE: 4643 OR 4943 ALUMINUM FILLER
ALLOY SHALL BE USED FOR ALL WELDS.
T1
½
P3
5 3/8"
P3
T1
T1
P3
P3
T1

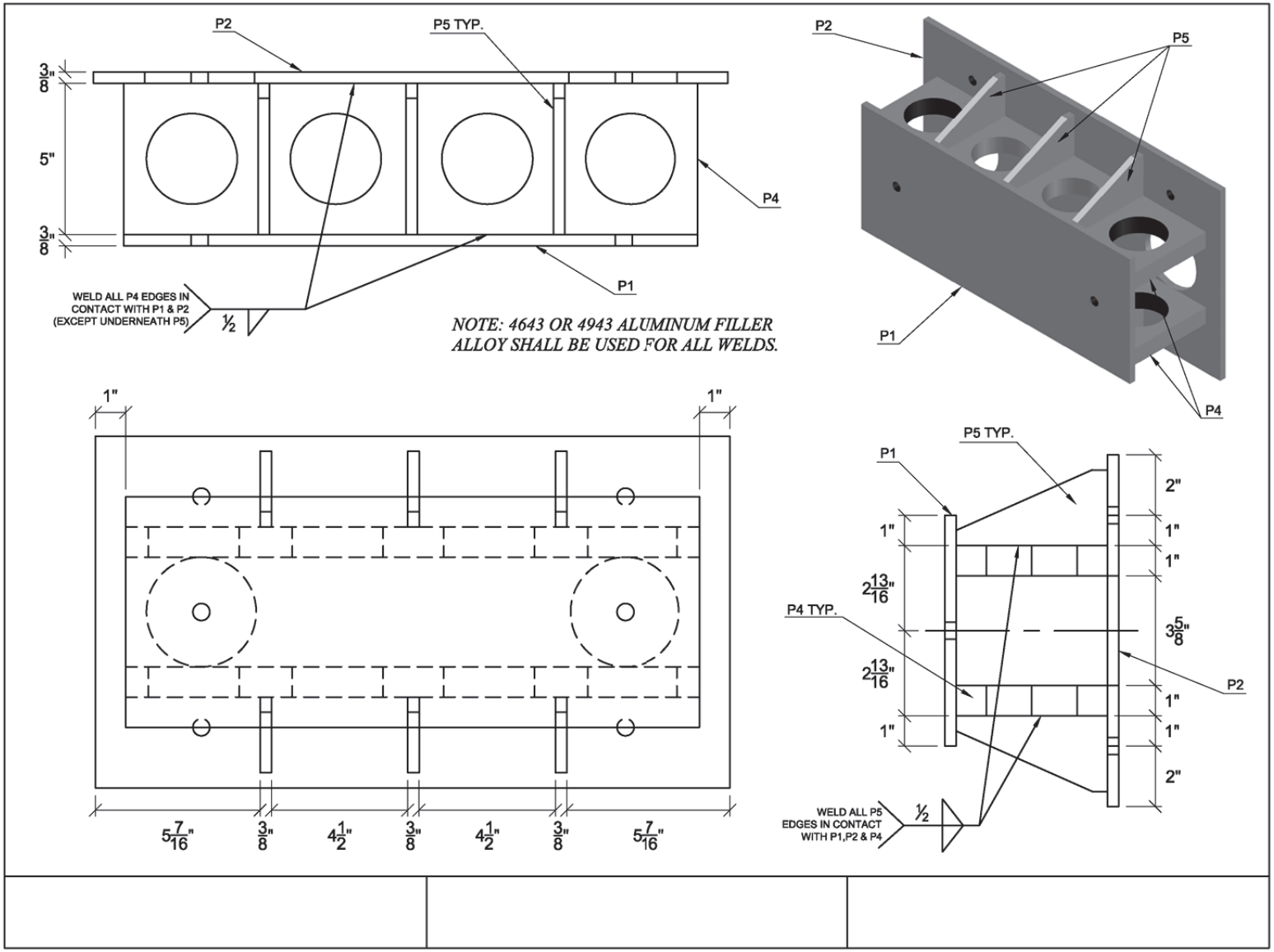
P2
P5 TYP.
3/8"
5"
3/8"
P4
P1
WELD ALL P4 EDGES IN CONTACT WITH P1 & P2 (EXCEPT UNDERNEATH P5)
1/2
NOTE: 4643 OR 4943 ALUMINUM FILLER ALLOY SHALL BE USED FOR ALL WELDS.
P2
P5
P1
P4
1"
1"
5 7/16"
3/8"
4 1/2"
3/8"
4 1/2"
3/8"
5 7/16"
P1
P5 TYP.
2"
1"
1"
1"
2 13/16"
P4 TYP.
3 5/8"
2 13/16"
P2
1"
1"
1"
2"
WELD ALL P5 EDGES IN CONTACT WITH P1,P2 & P4
1/2

MARK	QTY.	DRAWING	NOTES
P1	1	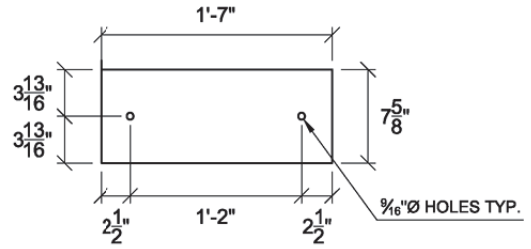	Aluminum 6061 T6 t = 3/8"
P2	1	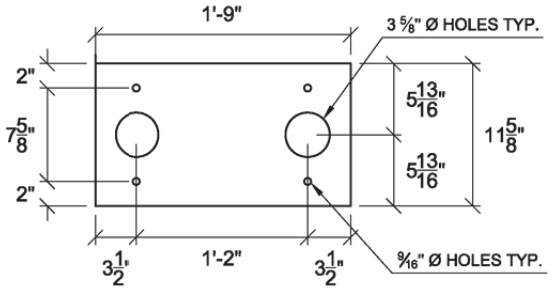	Aluminum 6061 T6 t = 3/8"
P3	2	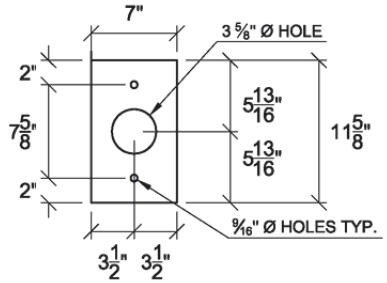	Aluminum 6061 T6 t = 3/8"

MARK	QTY.	DRAWING	NOTES
P4	2	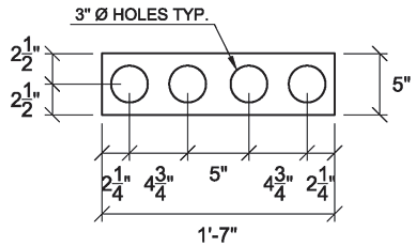	Aluminum 6061 T6 t = 1"
P5	6	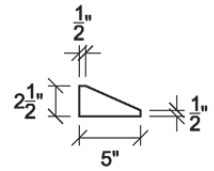	Aluminum 6061 T6 t = 3/8"
P6	2	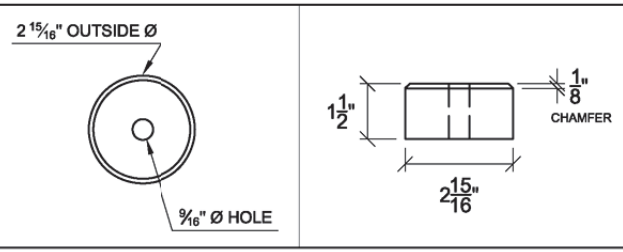	Aluminum 6061 T6 t = 1.5"
T1	4 *NOTE: DO NOT INCLUDE THE TUBE COST IN QUOTE, THIS WILL BE PROVIDED. ONLY INCLUDE MACHINING*	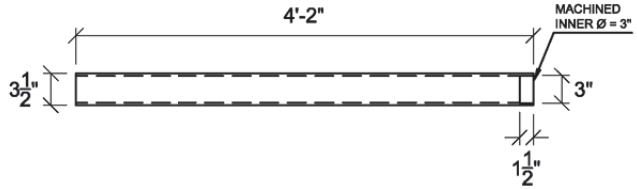	Aluminum 6061 T6 NPS = 3" Sch = 80

APPENDIX C
FRP COMPOSITE POST: MANUFACTURER DATA

Presented in this appendix are sectional and mechanical properties of the CP076 FRP composite post as specified by the product manufacturer (Creative Pultrusions, Inc.).

cp076.part	REV. NO. 2

DATE	SYM	REVISION RECORD	AUTH.	DR.	CK.
10-1 98	①	Was .180"			
10-1 98	②	Added flats			

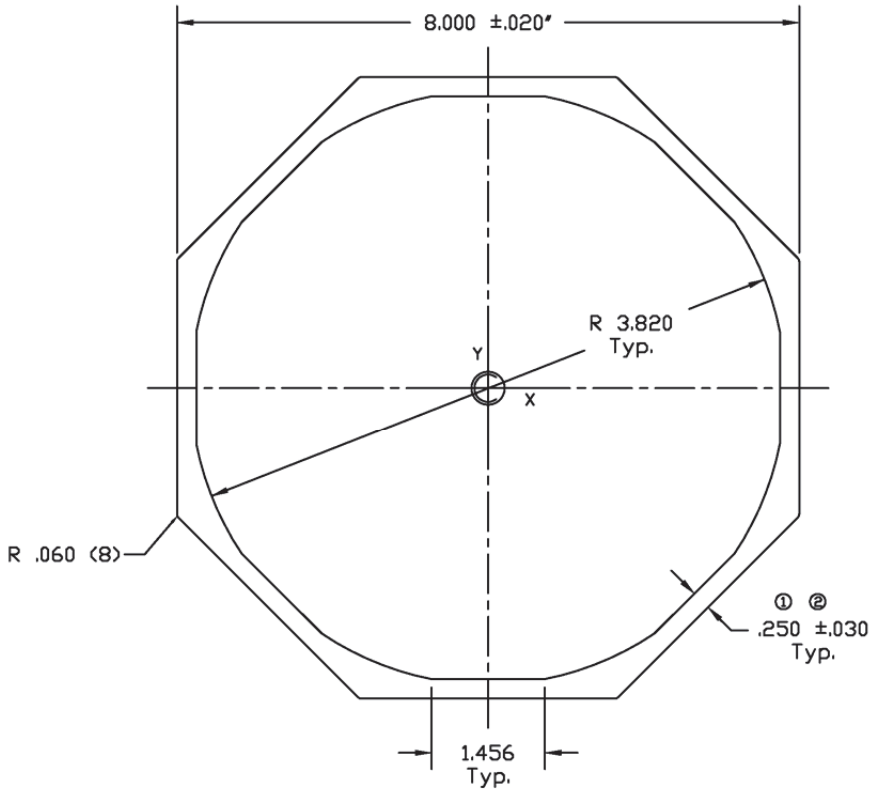

CROSS SECTION PROPERTIES		
Area	7.720	in^2
Ix	60.874	in^4
Iy	60.874	in^4
Ixy	0	in^4
Sx	15.219	in^3
Sy	15.219	in^3
rx	2.808	in
ry	2.808	in

214 Industrial Lane, P.O. Box 6
Alum Bank, Pennsylvania 15521-0006
www.creativepultrusions.com

DRAWN BY	RVH	5-21-98
CHECKED		
APPROVED		
UNITS:	Imperial	
SCALE:	1/2"	
FRACTIONS	±	as noted
DECIMAL	±	N/A
ANGLES	±	N/A

PART NAME:
8.00" x .250" Octagon

cp076.part	REV. NO. 2

POWERTRUSION
PRODUCTS

"GREEN TECHNOLOGY
FOR TODAY AND TOMORROW"

Engineering Specifications

The Powertrusion product line of poles have been specifically engineered to withstand the environmental forces of mother nature and to withstand the test of time. The three profiles are pultruded with a hybridized high performance matrix with an E-glass reinforcement package. The resin contains superior UV inhibitors, in addition, the pole is shrouded with a polyester surfacing veil that provides 10 mils of superior UV protection against the sun's harmful rays. The extremely durable, light weight, high strength POWERTRUSION poles are the strongest, most cost effective pultuded poles in the marketplace. In addition, the poles are pultruded by Creative Pultrusions, Inc., the world's foremost pultruder. Creative has been in the pultrusion business for over 38 years and is world renowned as the pultruder of choice for high strength pultrusions.

CP076
8" x .25" wall
(203mm x 6.3mm)

CP074
10.2" x .25" wall
(259mm x 6.3mm)

CP210
10.2" x .275" wall
(259mm x 7mm)

Mechanical and Physical Properties

	8" (203mm) Light Duty CP076	10.2" (259mm) Med. Duty CP074	10.2" (259mm) Heavy Duty CP210
Mechanical Properties			
Flexural strength (full section) psi (Mpa)	40,000 (275.8)	42,000 (289.6)	43,893 (302)
Ultimate Torque Strength (ft-lbs/N·m)	17,680 (23,971)	29,143 (39,512)	31,865 (43,203)
Axial Compression Strength psi (Mpa)	40,000 (275.8)	42,000 (289.6)	43,893 (302)
Modulus of Elasticity psi (Gpa)	3.8E6 (26.2)	4.0E6 (27.5)	3.7E6 (25.5)
Allowable Moment Kip-ft (kN·m)	30 (40.67)	50 (67.79)	61.5 (83.38)
Ultimate Hole Bearing Strength Lengthwise psi (Mpa)			
5/8" dia. Bolt	25,000 (172)	25,000 (172)	25,000 (172)
3/4" dia. Bolt	23,000 (159)	23,000 (159)	23,000 (159)
Note: Allowable Bending Moment FS=2			
Physical Properties			
Moment of Inertia in^4 (mm^4)	60.87 (2.53E7)	139.69 (5.81E7)	171.57 (7.14E7)
Section Modulus in^3 (mm^3)	15.22 (2.49E5)	27.39 (4.49E5)	33.64 (5.51E5)
Radius of Gyration in (mm)	2.81 (71.4)	3.60 (91.4)	3.57 (90.7)
Weight lbs/ft (N/m)	6.33 (92.4)	8.82 (128.7)	11.05 (161.3)
Area in^2 (mm^2)	7.72 (4980)	10.76 (6942)	13.47 (8690)
Coefficient of Thermal Expansion Lengthwise	5.0^{-6} in/in/°F	5.0^{-6} in/in/°F	5.0^{-6} in/in/°F
Water Absorption	<.60%	<.60%	<.60%
Fiber Volume Fraction	≥ 50%	≥ 50%	≥ 50%
Cross Sectional Area in^2 (mm^2)	7.72 (4980)	10.76 (6942)	13.47 (8690)
Surface Area ft^2 (m^2/m)	2.2 (.67)	2.8 (.85)	2.8 (.85)

Creative Pultrusions, Inc.
214 Industrial Lane
Alum Bank, PA 15521

Powertrusion Products
www.powertrusion.com

Voice: 888-274-7855
Fax: 814-839-4276
www.creativepultrusions.com

PTES-0509.1C

DLR: 09.23.11

APPENDIX D
FRP COMPOSITE POST: STATIC SHEAR TESTING

Presented in this appendix are test procedures and results from static shear testing of the CP076 FRP composite post section. A static test was conducted at the University of Florida Structures Laboratory on August 13, 2013 to assess FRP post strength and deformation behavior under direct shear load. An FRP post 3 ft long was tested using a Tinius Olsen testing machine with integrated data collection. A vertical displacement rate of 0.5 in/sec was used, and data were collected at a frequency of 2.7 Hz.

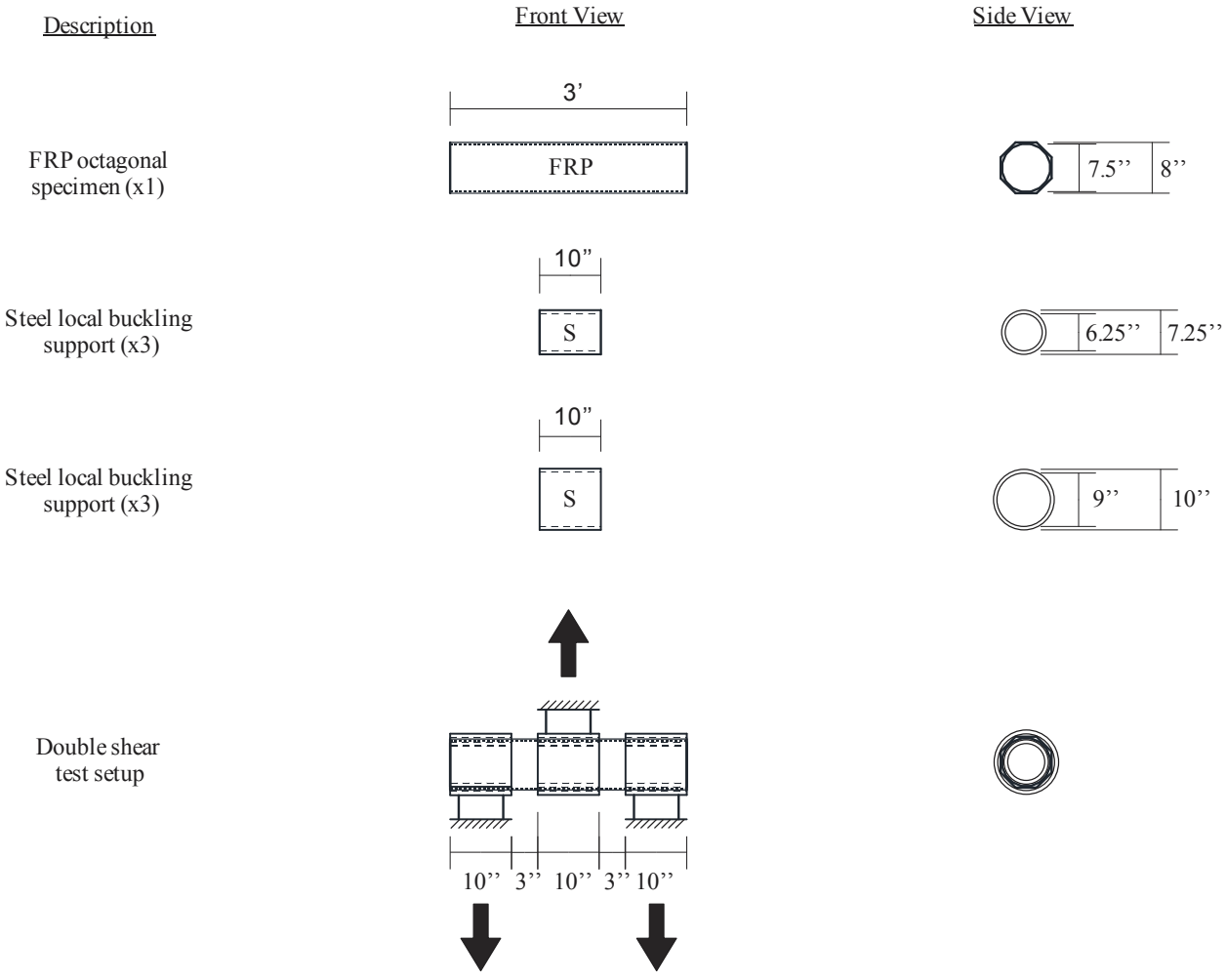

Figure D.1. Schematic diagraph of static double-shear test setup

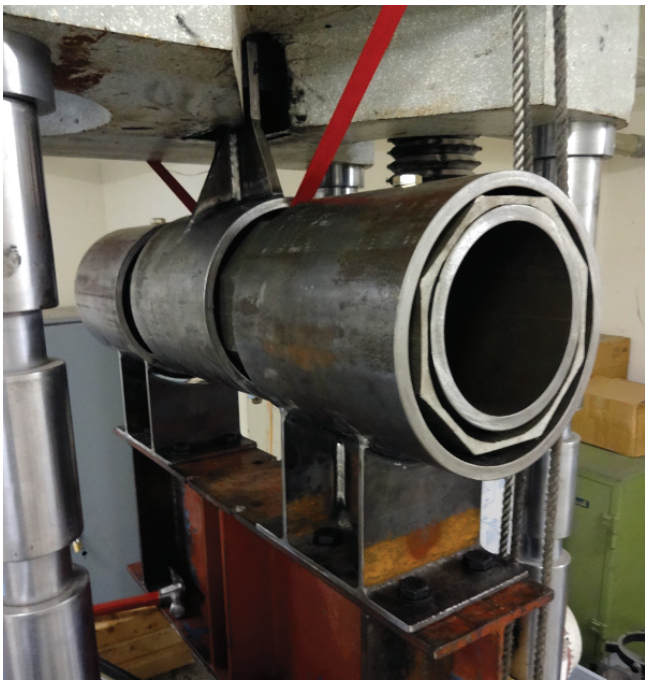

Figure D.2. Static double-shear test setup

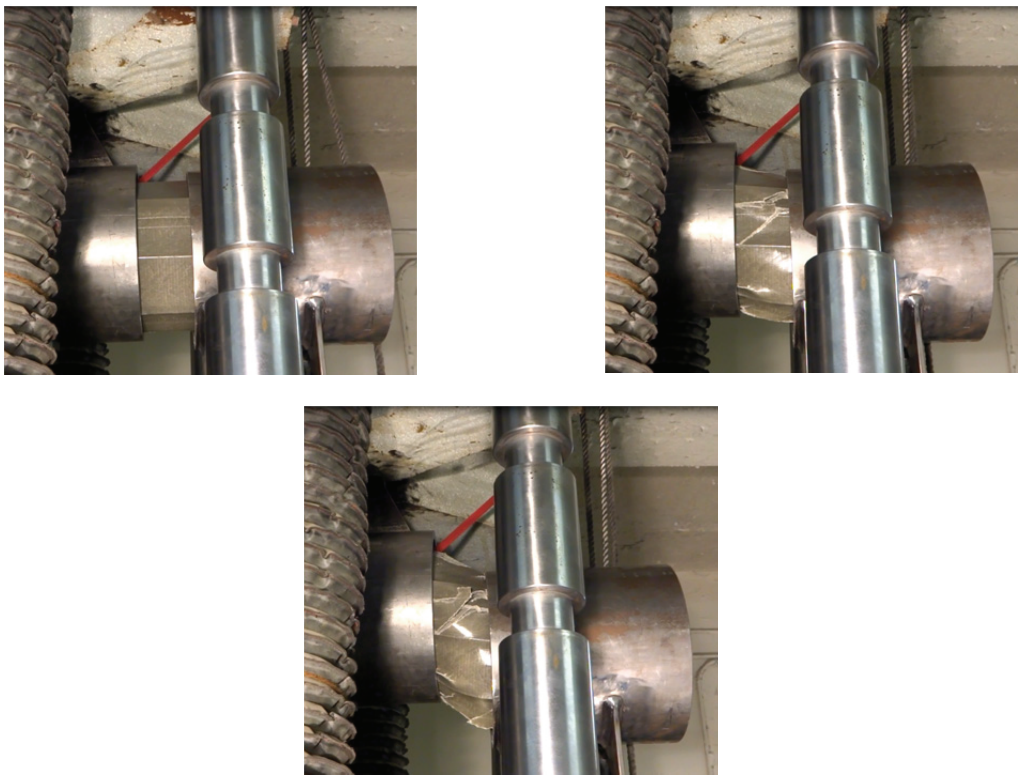

Figure D.3. Section deformation during static double-shear test

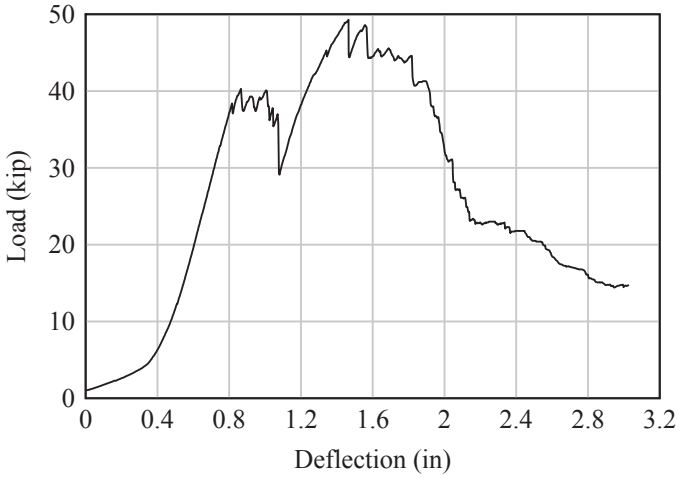

Figure D.4. Static double-shear test results

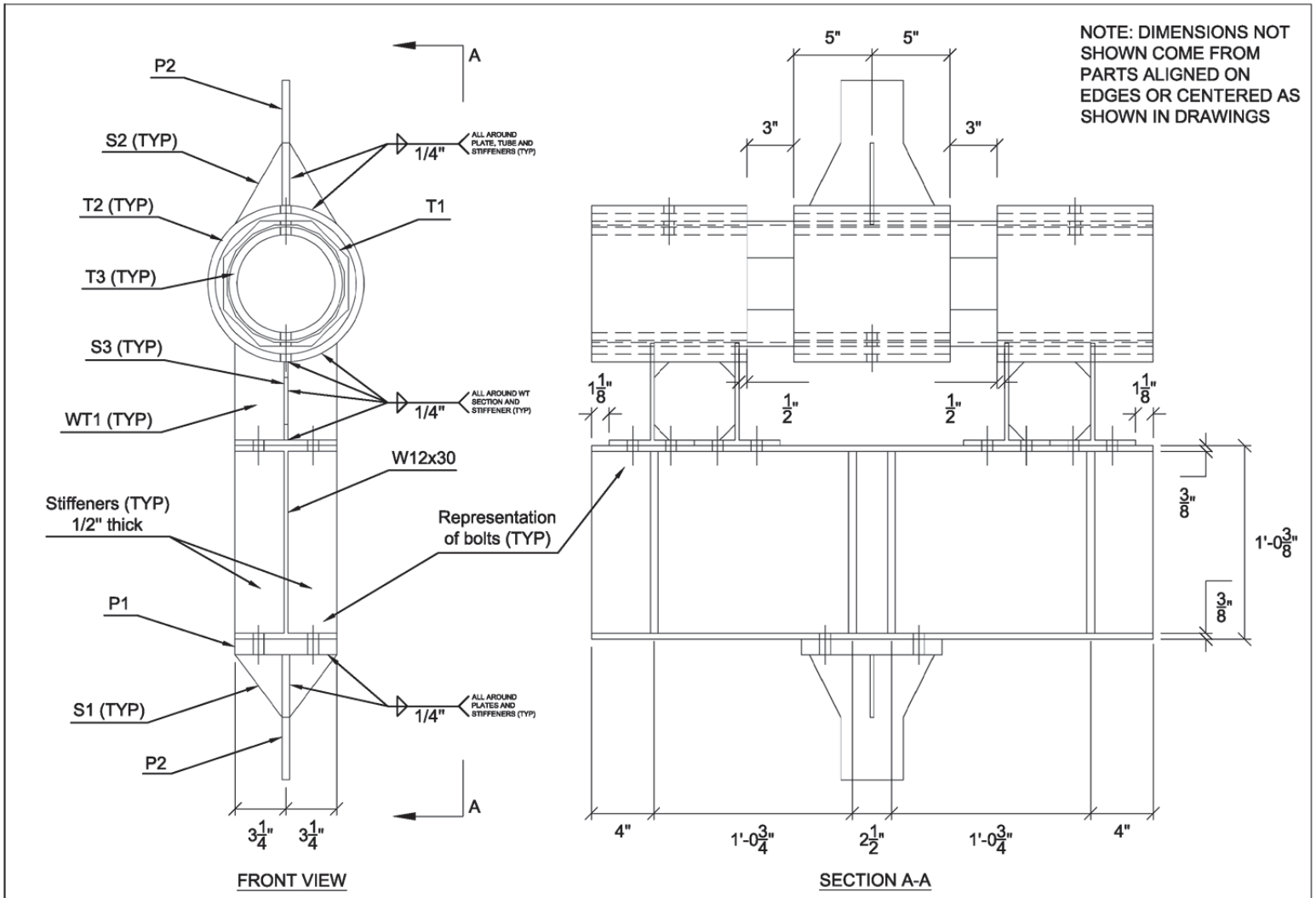

Pendulum Impact Testing of Metallic, Non-metalic, and Hybrid Sign Posts				*Revisions:*	

MARK	QTY.	DRAWING	NOTES
T1	1	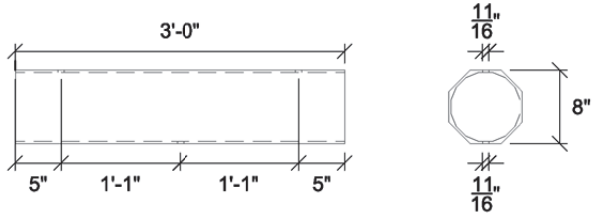	8" Diameter Octagonal FRP Specimen t = 1/4"
T2	3	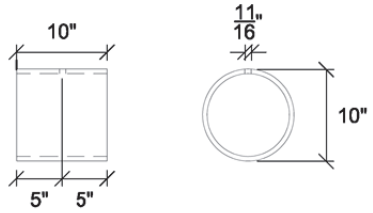	10" Diameter Steel Tube t = 1/2"
T3	3	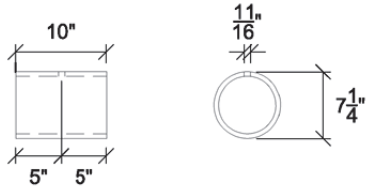	7.25" Diameter Steel Tube t = 1/2"
P1	1	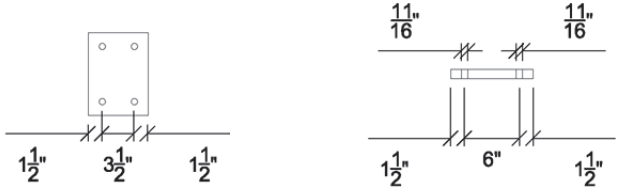	Steel Plate t = 1/2" *From Thick Plate #1 Provided

Pendulum Impact Testing of Metallic, Non-metalic, and Hybrid Sign Posts				Revisions:		

P2	*2*	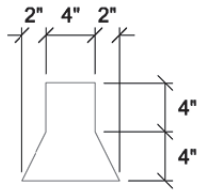	*Steel Plate* *t = 1/2"* **From Thick Plate #2 Provided*
WT1	*4*	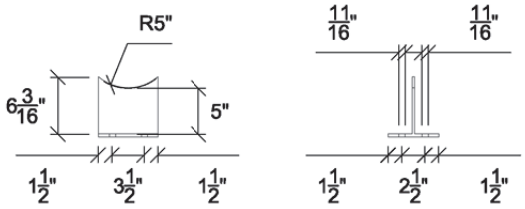	*WT8x13* *6.5" long*
S1	*2*	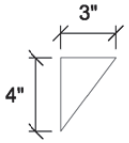	*Steel Plate* *t = 1/4"* **From Thin Plate Provided*
S2	*2*	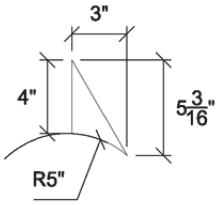	*Steel Plate* *t = 1/4'* **From Thin Plate Provided*

Pendulum Impact Testing of Metallic, Non-metalic, and Hybrid Sign Posts				*Revisions:*	

MARK	QTY.	DRAWING	NOTES
S3	2	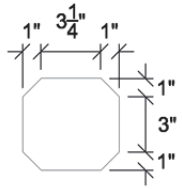	Steel Plate t = 1/4" *From Thin Plate Provided
B1	20	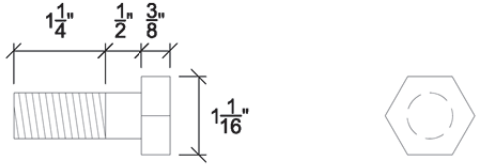	5/8" - 11 1 3/4" Long A325 Bolt
W1	40		Plain Steel Bolt Washer For 5/8" Bolt
N1	20	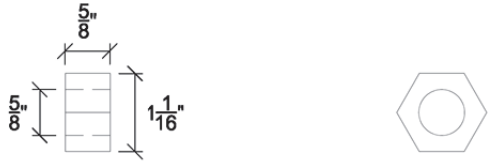	5/8" - 11 Hex Nut Grade C

Pendulum Impact Testing of Metallic, Non-metalic, and Hybrid Sign Posts				Revisions:		

APPENDIX E
STRUCTURAL DRAWINGS: HYBRID SHEAR COLLAR

Presented in this appendix are fabrication drawings for the ‘shear collar’ hybrid breakaway connection system developed and tested in this study.

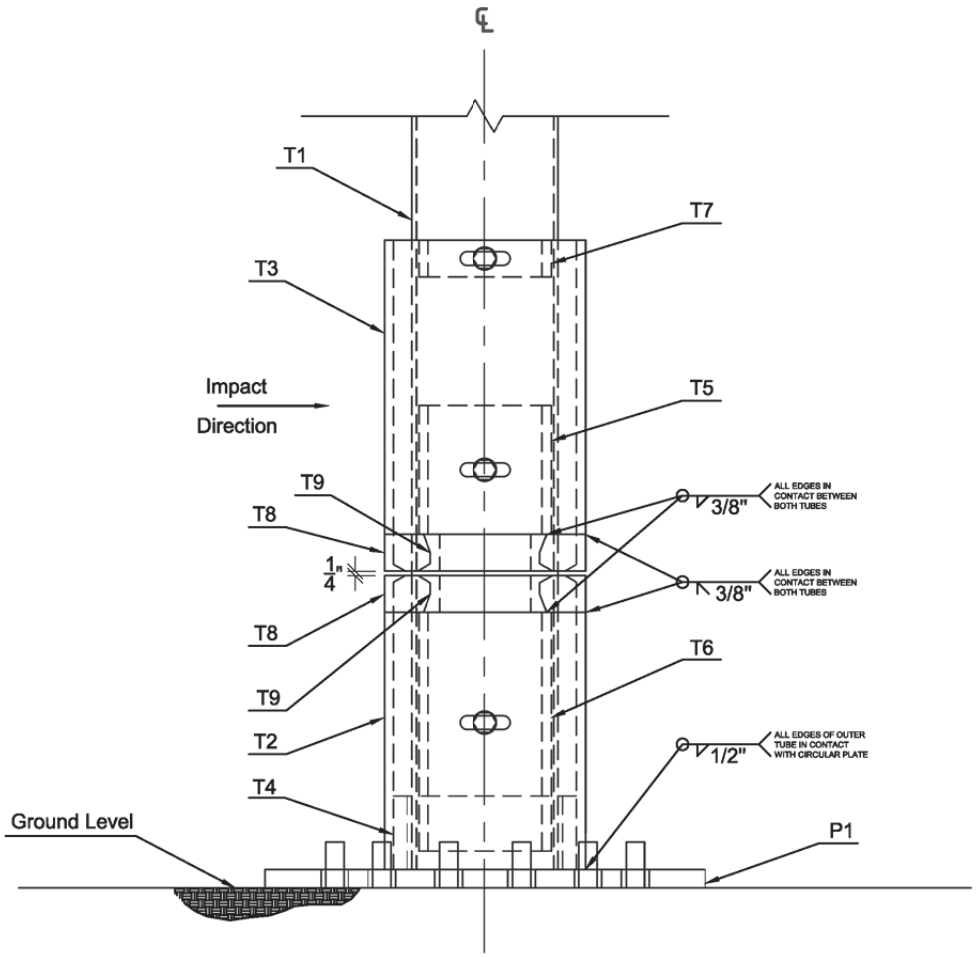

SIDE VIEW

Pendulum Impact Testing of Metallic, Non-metalic, and Hybrid Sign Posts				*Revisions:*		

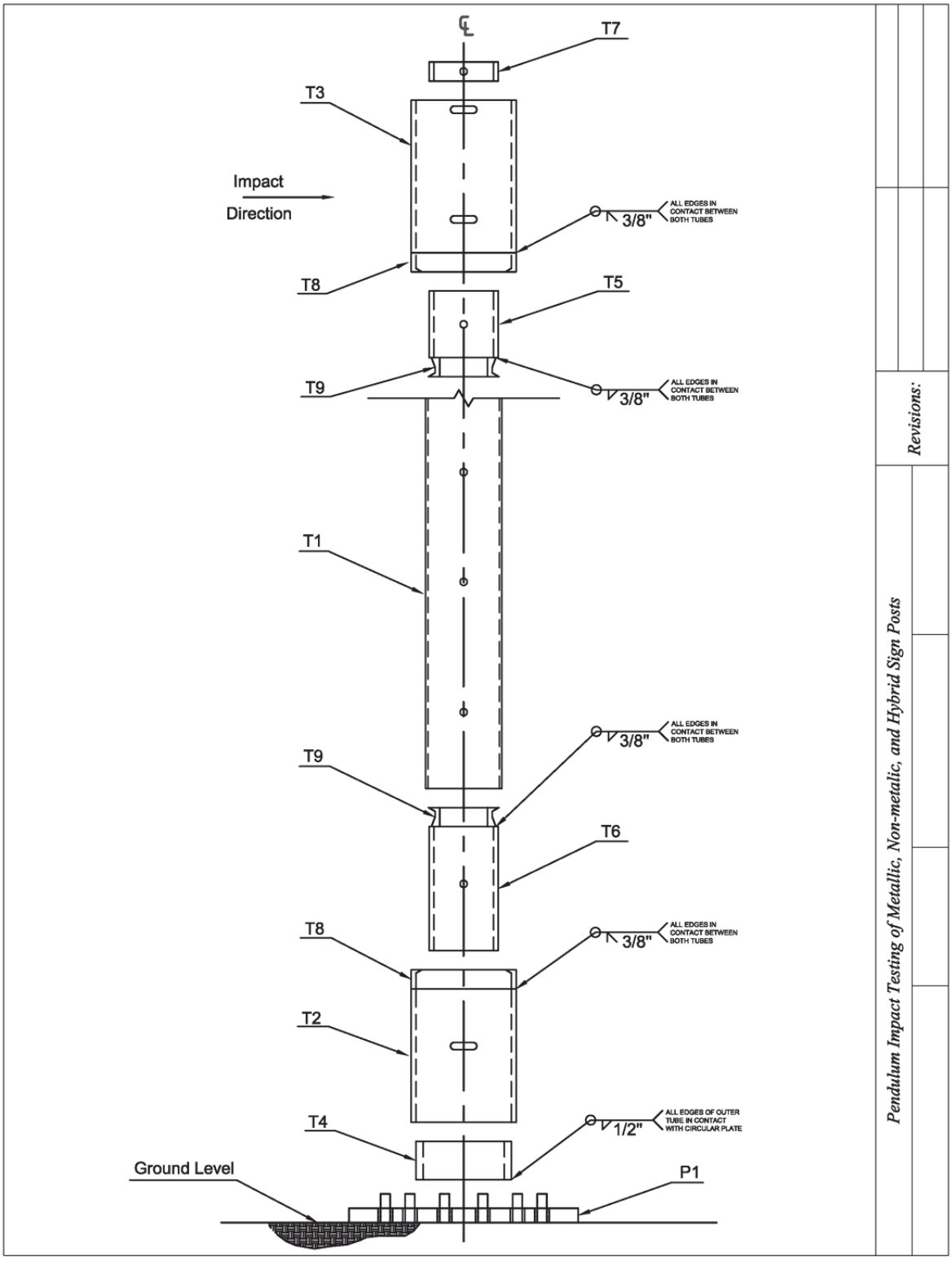
T7
T3
Impact
Direction
3/8"
ALL EDGES IN CONTACT BETWEEN BOTH TUBES
T8
T5
T9
3/8"
ALL EDGES IN CONTACT BETWEEN BOTH TUBES
T1
T9
3/8"
ALL EDGES IN CONTACT BETWEEN BOTH TUBES
T6
T8
3/8"
ALL EDGES IN CONTACT BETWEEN BOTH TUBES
T2
T4
1/2"
ALL EDGES OF OUTER TUBE IN CONTACT WITH CIRCULAR PLATE
Ground Level
P1
Revisions:
Pendulum Impact Testing of Metallic, Non-metalic, and Hybrid Sign Posts

MARK	QTY.	DRAWING	NOTES
T1	1	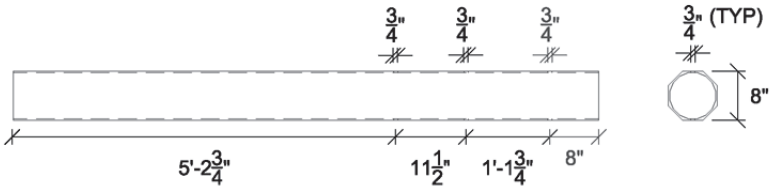	Octagonal FRP Specimen
T2	1	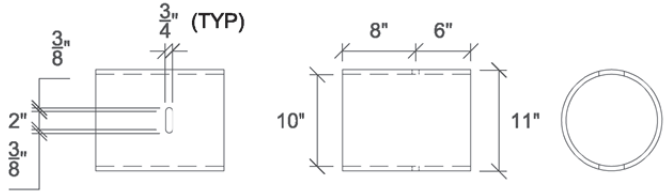	11" Diameter Steel Tube t = 1/2" l = 14"
T3	1	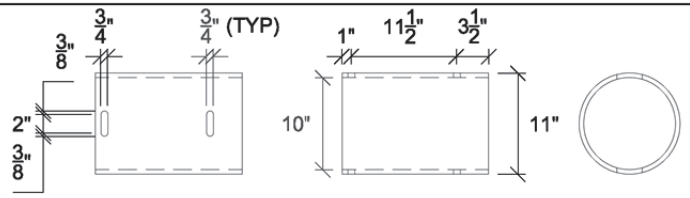	11" Diameter Steel Tube t = 1/2" l = 16"
T4	1	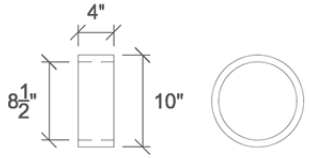	10" Diameter Steel Tube t = 3/4" l = 4"
T5	1	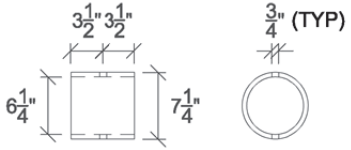	7.25" Diameter Steel Tube t = 1/2" l = 7"

Pendulum Impact Testing of Metallic, Non-metalic, and Hybrid Sign Posts				Revisions:		

MARK	QTY.	DRAWING	NOTES
T6	1	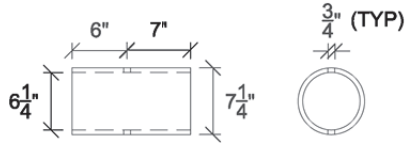	7.25" Diameter Steel Tube t = 1/2" l = 13"
T7	1	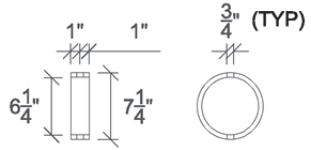	7.25" Diameter Steel Tube t = 1/2" l = 2"
P1	1	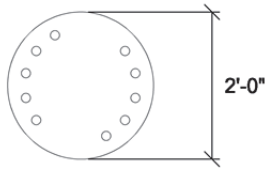	Circular Steel Plate t = 1"
W1	6		Aluminum Washer For 5/8" Bolt
N1	6	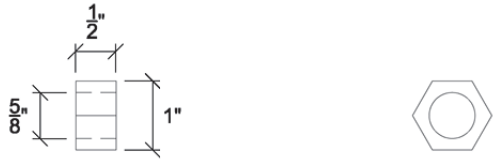	5/8" - 11 Threaded Nut Grade 2 Steel

Pendulum Impact Testing of Metallic, Non-metalic, and Hybrid Sign Posts				Revisions:		

MARK	QTY.	DRAWING	NOTES
B1	3	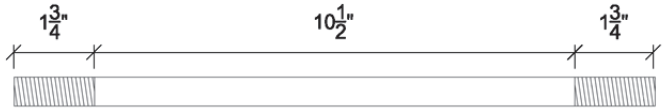	5/8" - 11 14" long Spacing Stud
T8	2	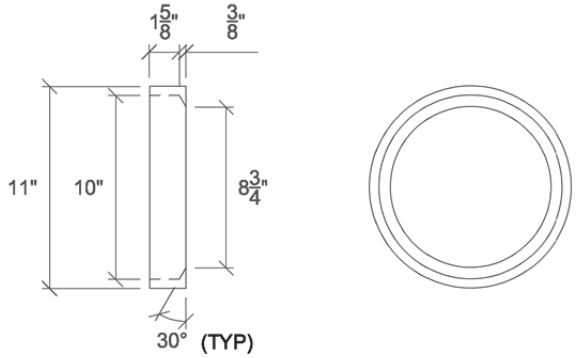	11" Diameter Steel Tube t = 1.5" (lathe) l = 2"
T9	2	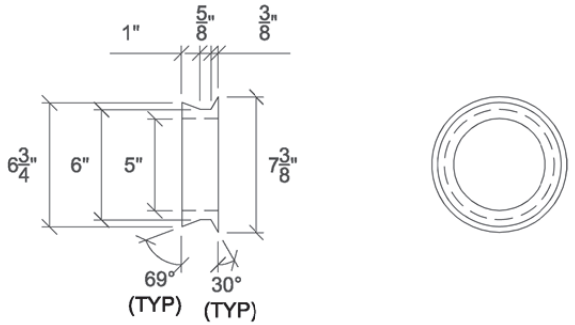	7.5" Diameter Steel Tube t = 1.25" (lathe) l = 2"

Pendulum Impact Testing of Metallic, Non-metalic, and Hybrid Sign Posts				Revisions:		

APPENDIX F
STRUCTURAL DRAWINGS: HYBRID MOMENT COLLAR

Presented in this appendix are fabrication drawings for the ‘moment collar’ hybrid breakaway connection system developed and tested in this study.

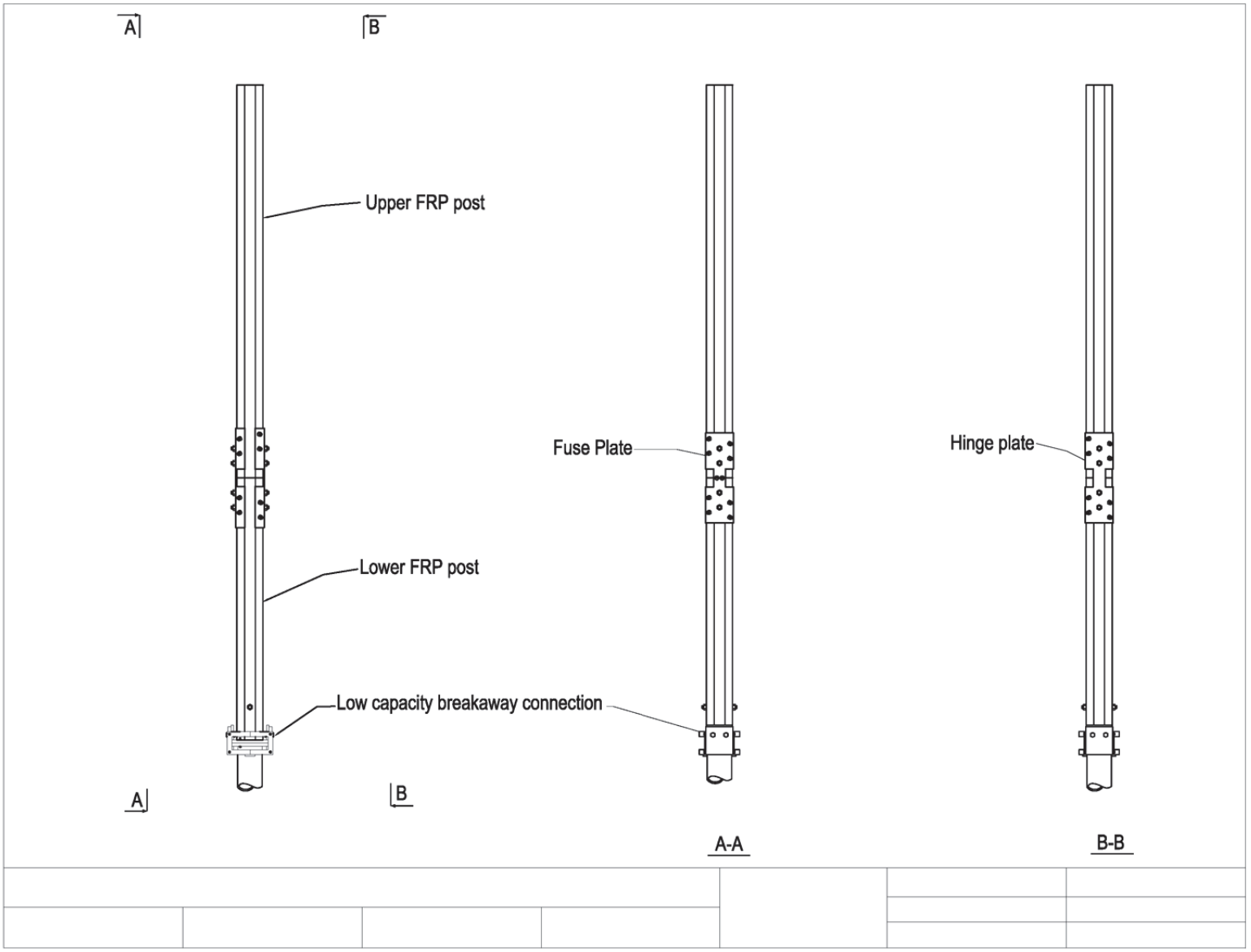
A
B
Upper FRP post
Lower FRP post
Low capacity breakaway connection
Fuse Plate
Hinge plate
A
B
A-A
B-B

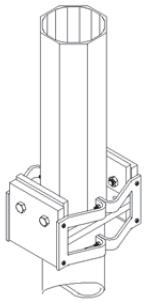

Assembled system

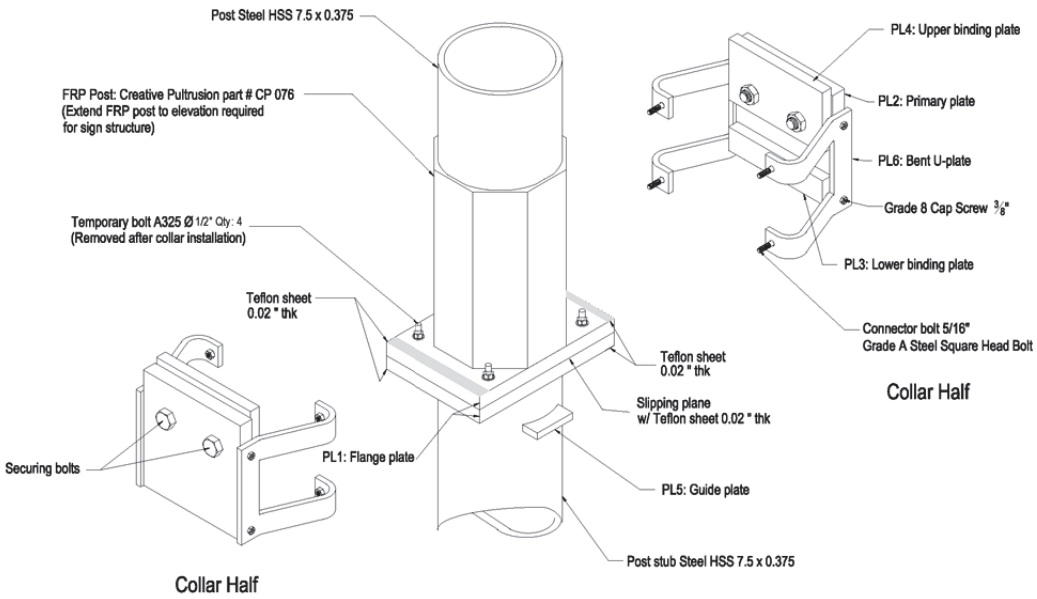

Collar Half

Collar Half

Note: HSS is 42 ksi, all other steel is A572 Gr. 50 unless otherwise noted.

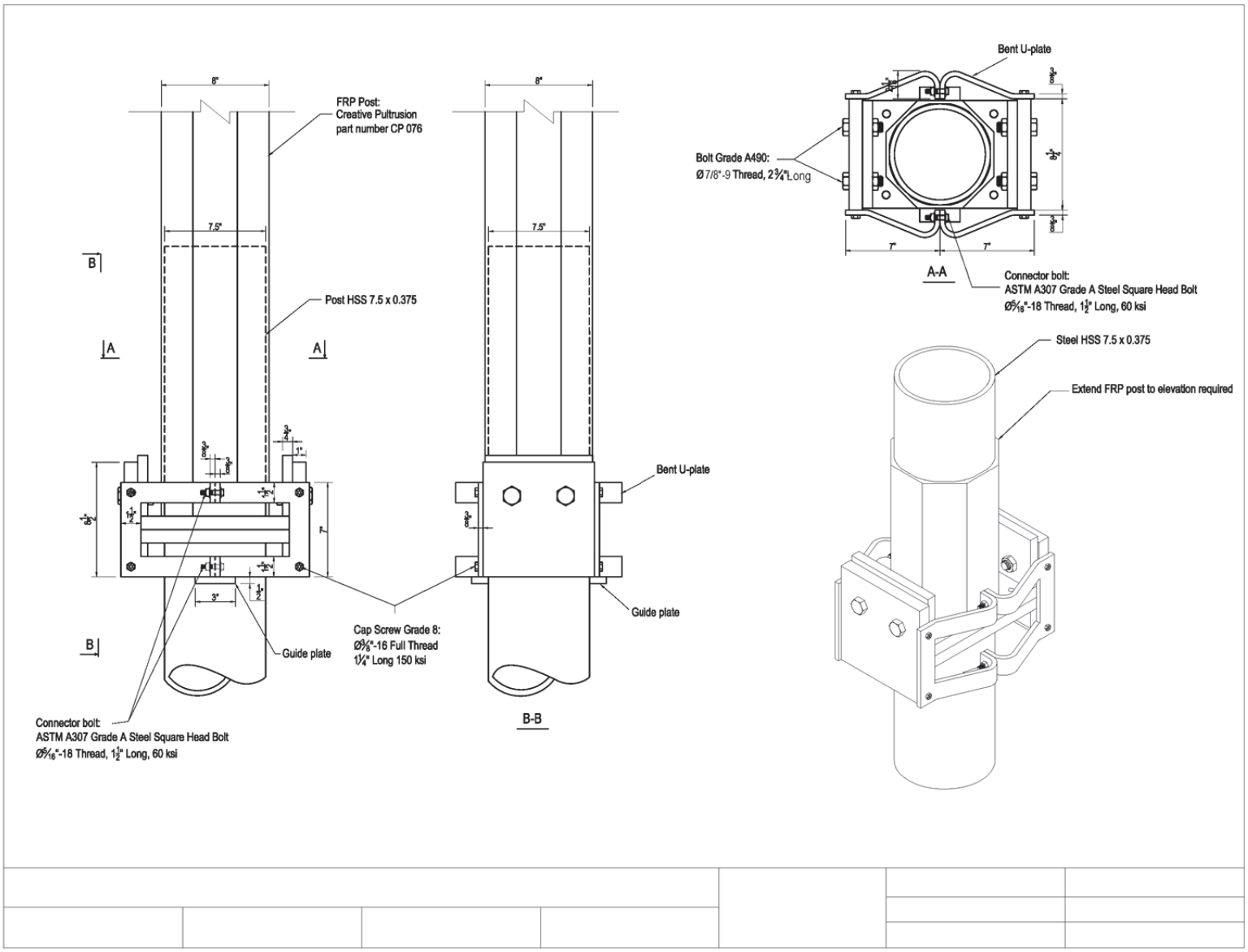
8"
FRP Post:
Creative Pultrusion
part number CP 076
7.5"
B
Post HSS 7.5 x 0.375
A
A
B
Guide plate
Connector bolt:
ASTM A307 Grade A Steel Square Head Bolt
Ø5/16"-18 Thread, 1½" Long, 60 ksi
Cap Screw Grade 8:
Ø3/8"-16 Full Thread
1¼" Long 150 ksi
Bent U-plate
Guide plate
B-B
Bent U-plate
Bolt Grade A490:
Ø7/8"-9 Thread, 2¾"Long
7"
A-A
Connector bolt:
ASTM A307 Grade A Steel Square Head Bolt
Ø5/16"-18 Thread, 1½" Long, 60 ksi
Steel HSS 7.5 x 0.375
Extend FRP post to elevation required

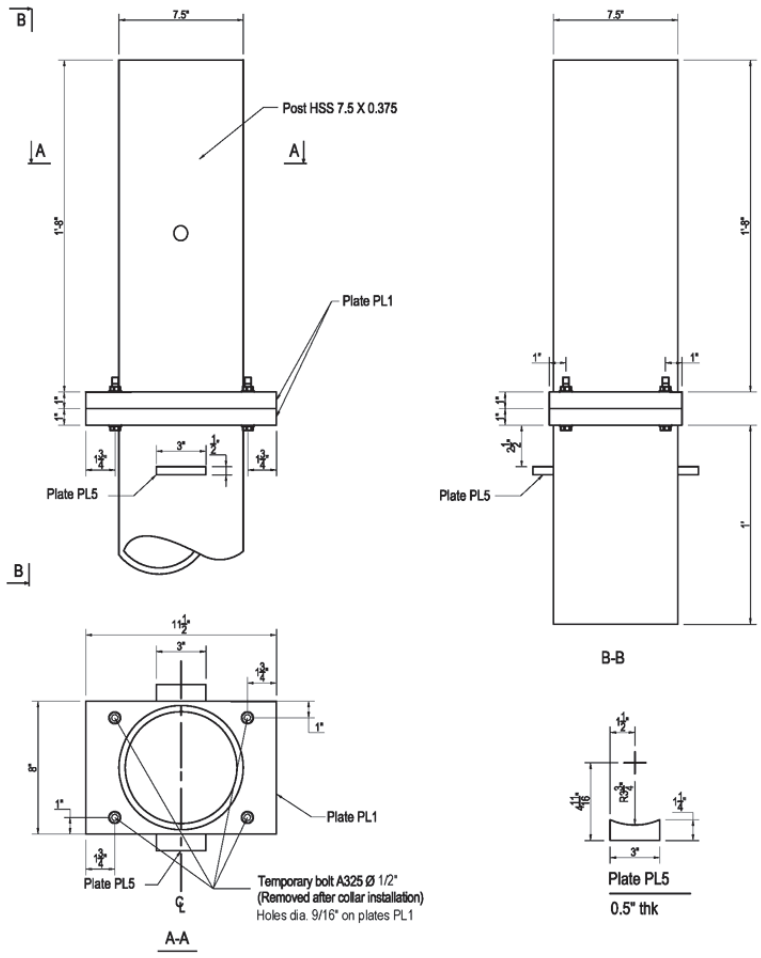
B
A
A
B
7.5"
Post HSS 7.5 X 0.375
Plate PL1
Plate PL5
1'-8"
3"
A-A
Plate PL1
Plate PL5
Temporary bolt A325 Ø 1/2"
(Removed after collar installation)
Holes dia. 9/16" on plates PL1
B-B
Plate PL5
0.5" thk

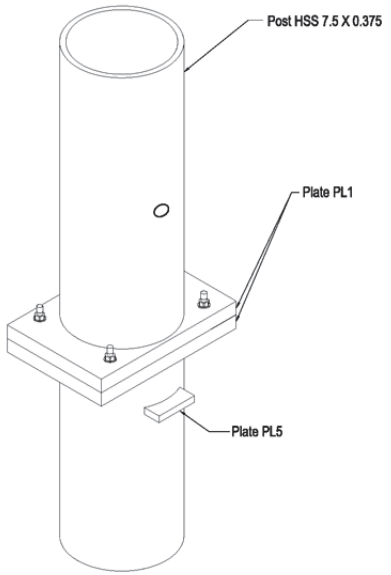
Post HSS 7.5 X 0.375
Plate PL1
Plate PL5

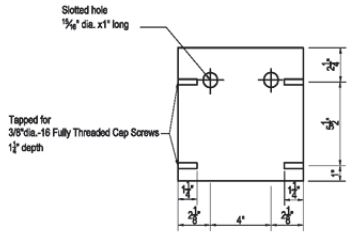

PRIMARY PLATE: PL2
Plate thickness= 1"

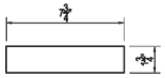

LOWER BINDING PLATE: PL3
Plate thickness= 1"

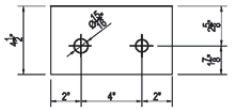

UPPER BINDING PLATE: PL4
Plate thickness= 1"

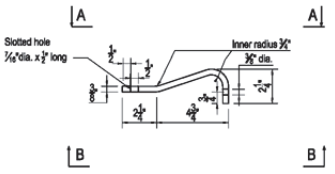

PLAN VIEW OF BENT U-PLATE: PL6
Plate thickness= ⅜"

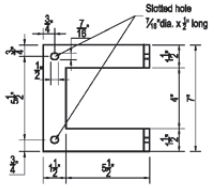

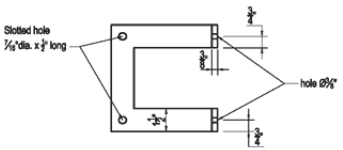

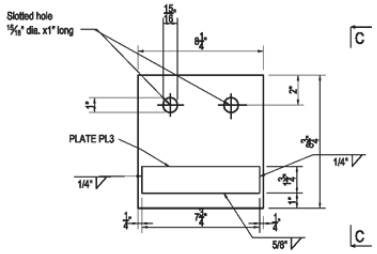

LOWER BINDING PLATE
WELDED TO PRIMARY PLATE

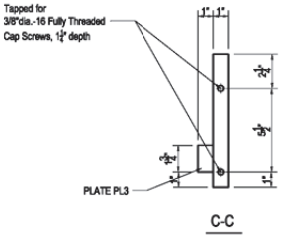

C-C

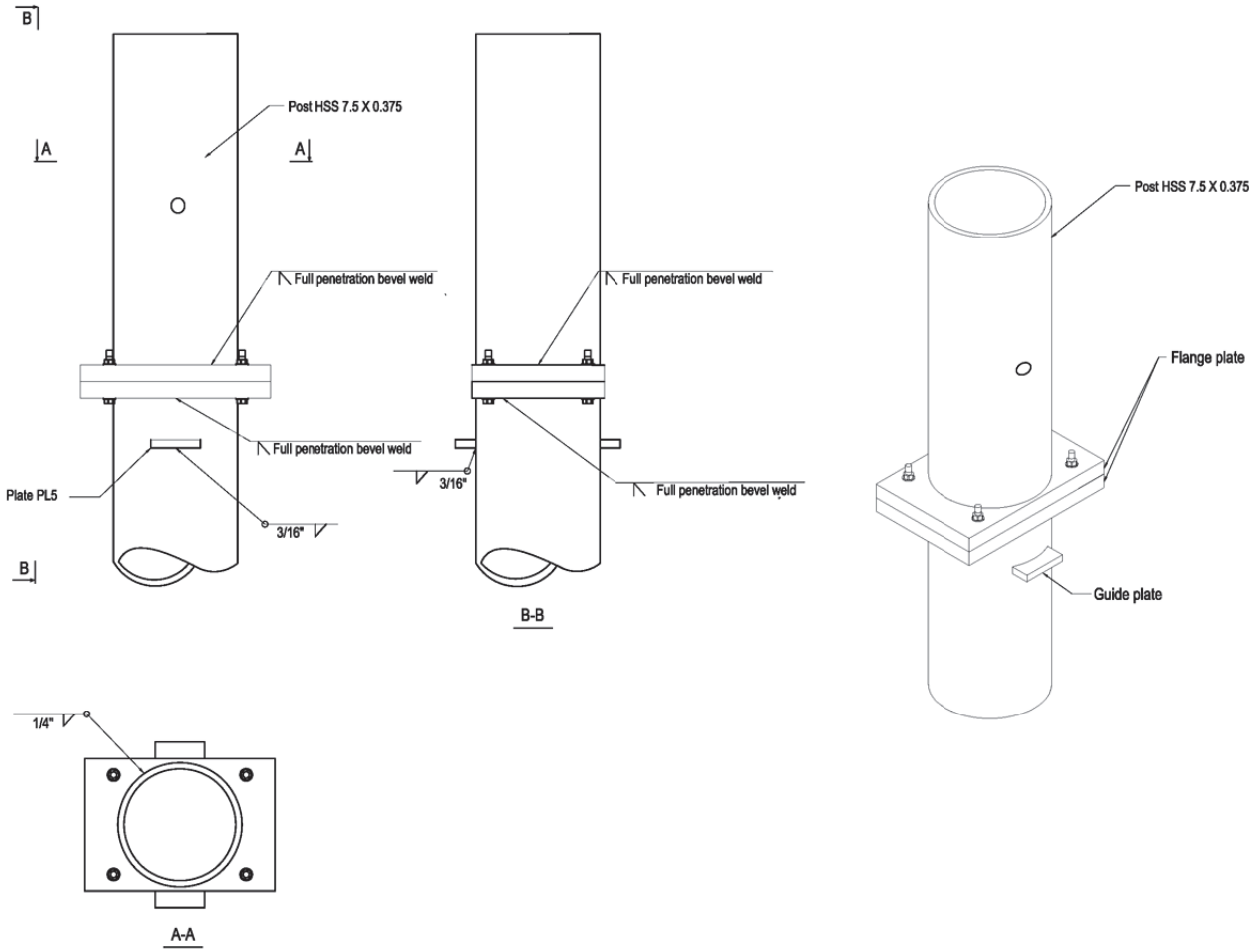
B
A
A
Post HSS 7.5 X 0.375
Full penetration bevel weld
Full penetration bevel weld
Full penetration bevel weld
Plate PL5
3/16"
B
3/16"
Full penetration bevel weld
B-B
Post HSS 7.5 X 0.375
Flange plate
Guide plate
1/4"
A-A

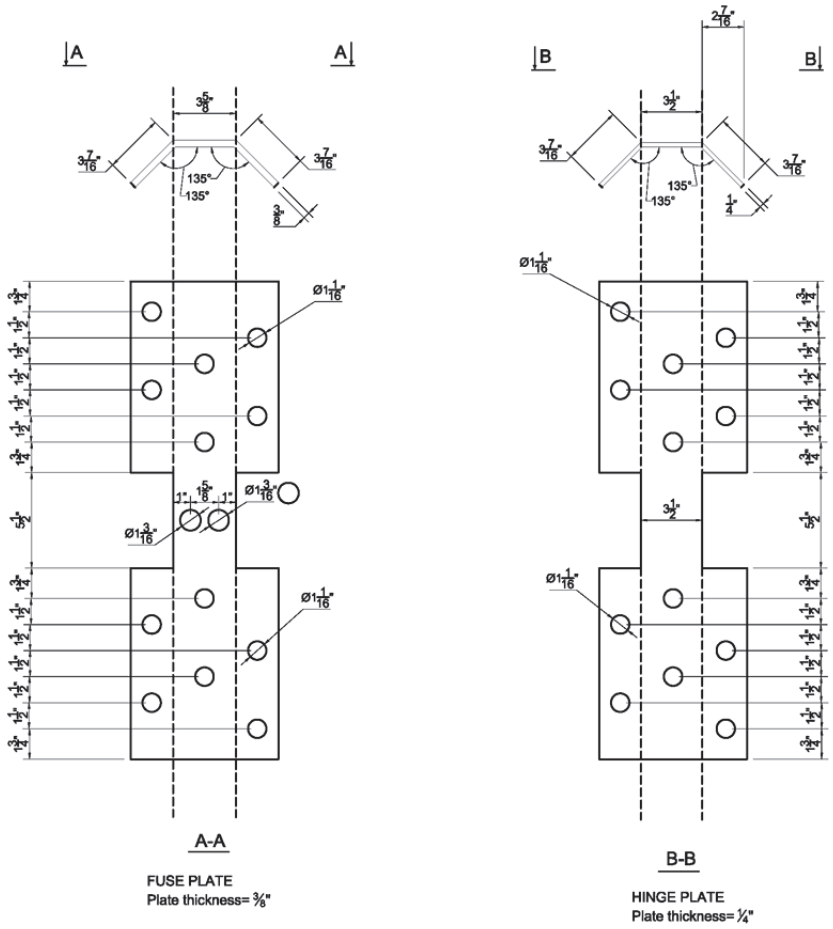
A
A
B
B
135°
135°
A-A
FUSE PLATE
Plate thickness= ⅜"
B-B
HINGE PLATE
Plate thickness= ¼"